NORTHWESTERN UNIVERSITY

Antenna-Coupled Quantum Well Infrared Photodetectors: Enhancement and Beam-Forming

A DISSERTATION

SUBMITTED TO THE GRADUATE SCHOOL
IN PARTIAL FULFILMENT OF THE REQUIREMENTS

for the degree

DOCTOR OF PHILOSOPHY

Field of Electrical Engineering

By

Robert L. Brown

Evanston, Illinois
March 2018

Abstract

This thesis reports on the use of optical antennas, and more broadly, metal optics for the engineered collection and enhancement of infrared photodetectors. These ideas would be useful in enhancing at other wavelengths and other types of detectors, but this work is specifically focused on the Quantum Well Infrared Photodetector (QWIP) and addressing its shortcomings, while enhancing its advantages. Metallic antennas can be used to collect light, resonate, enhance in a nearfield, change polarization, and re-direct the direction of incident light. These properties can be directly applied to QWIP to enhance absorption, apply electric field across the quantum wells (necessary for absorption), and reduce noise by allowing for a smaller electrical volume, and thus a smaller dark current.

This project was also interested in extending QWIP and infrared detectors beyond their typical direct collection and enhancement; delocalization of a collector and source can open doors for interesting research and applications. Inspired by microstrip antennas and waveguides typically seen in the microwave, and enabled by a metal-to-metal substrate bonding process, micro-scale patch antennas and waveguides are fabricated to support infrared modes and direct collected light to QWIP.

In this work a flexible, modular platform for integration of antennas with QWIP has been developed and demonstrated; a simple metal-to-metal substrate bonding process was integrated with etched QWIP and antennas for a three-dimensional device that is compatible with other semiconductor processes. This process was proven to work with QWIP with the demonstration of an etched Grating Device with a responsivity of 0.12A/V, an improvement over the only other reported small-volume QWIP.

The flexibility of this platform was also demonstrated by the addition of BCB microstrip waveguides and antennas. We showed that with a stationary biased absorber, one can waveguide-couple an antenna allowing for delocalized coupling to QWIP. Due to the modular nature of this design and relative simplicity of fabrication, any of these components can be replaced or expanded on allowing either 1) the introduction of QWIP to applications beyond typical focal plane arrays or 2) the use of an emitter instead of absorber for a controlled, directional radiation of infrared.

Acknowledgements

First of all, I would like to thank my advisor, Professor Hooman Mohseni, who has helped me grow as an engineer, and as a person. His mentoring, guidance, and intense approach to attacking problems will always stick with me.

I also would like to thank all my collaborators, (in no particular order): Alireza Bonakdar, Omer Gokalp Memis, Sung Jun Jang, Min Su Park, Chee Leong Tan, Edward Kinzel, Alan Selewa, Mohsen Rezaei, Skylar Wheaton, Iman Hassani Nia, Travis Hamilton, Simone Bianconi, Cobi Rabinowitz, Vala Fathipour, Ryan Gelfand, and Jack Kohoutek

I would next like to thank my undergraduate advisor Dr. Stefan Preble, for giving me my first opportunity to work in an academic laboratory and opening my eyes to the world of optics.

I wish to thank my family: My parents, my brother, and Sophie, for their continued support and encouragement. Finally, I wish to thank the first electrical engineer I ever met, my late grandfather Clarence O. Brown, who inspired me to follow this path.

Table of Contents

I. Introduction

Quantum Well Infrared Photodetectors (QWIP) were introduced as an alternative to the state-of-the-art Mercury Cadmium Telluride (HgCdTe) detectors used for mid- to long-wave infrared detection [1]. HgCdTe is a direct-band semiconductor and has strong absorption, but is expensive and hard to work with, and has large variation across even one array [2]. There are alternative technologies typically based on the relatively mature and inexpensive III-V semiconductor platform (either GaAs or InP). For this to work, an intersubband process is required using quantum dots [3], quantum wires [4], or quantum wells [5]. Quantum Wells, the most viable of these realized in QWIP, though relatively easy to fabricate, suffer from weak and polarization-dependent absorption, and the material itself in a traditional detecting platform cannot be pushed to compete with HgCdTe.

Optical antennas [6] have been demonstrated extensively to enhance light matter interaction in the visible [7] and the infrared [8]. In this dissertation, we show that these principles can be applied to QWIP to boost performance in three ways: 1) Boost Quantum Efficiency by enhancing the near field and by allowing a strong resonance, 2) Reduce dark current noise by shrinking the device volume while maintaining optical collection area, 3) Reduce background radiation and eliminate the need for a cold shield by making the collection field of view as small as possible. We also demonstrate de-localization of radiation collection and detection that could be useful for applications such as beam-forming/beam-steering.

In this document we design, fabricate, and measure two designs that aim to address those performance goals. Additionally, we show an extension of microwave antenna concepts to III-V semiconductors by using microstrip technology can allow for brand new applications of infrared detection like lens-less imaging and beam-forming.

II. Theory of Quantum Well Infrared Photodetectors

A. Quantum Well Infrared Photodetectors

Though the bulk semiconductors typically used as photodetectors don't have band gaps small enough to absorb mid- to long-wave infrared photons, systems of these materials can be engineered to have discrete energy levels based on confinement of charge carriers (electrons) [9]. Confinement in one, two, or three dimensions can be utilized to absorb infrared radiation; quantum dots confine in three dimensions, quantum wires in two dimensions, and quantum wells in one dimensions. Each of these have interesting properties and applications, but the most practical in the context of infrared detection are quantum wells. This is due to the ease of material growth, stability, and quantum efficiency and as such this document will deal exclusively with Quantum Well absorbers.

A quantum well is a structure with a low electron potential energy surrounded sandwiched by a relatively higher electron potential energy. The solution for Schrodinger's Equation in this potential well allows only discrete energy levels in the well and a continuum of allowed states above the well [10]. Excited electrons can relax to a lower energy and emit a photon with the energy lost from relaxation. Likewise, an electron can be excited thermally or by absorbing a photon and go to a higher state or the continuum [11] (Figure 1)

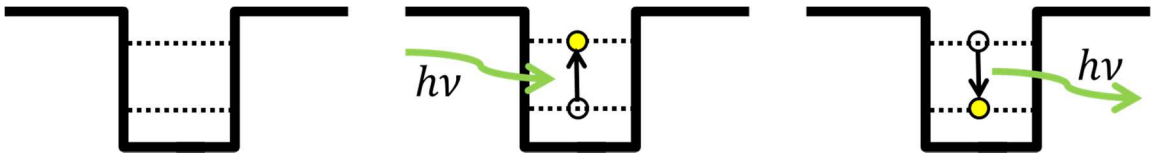

Figure 1a) Quantum Well Energy Levels b) Diagram of Quantum Well Photon Absorption c) diagram of Quantum Well Photon Emission

Quantum wells can be made in semiconductors by sandwiching thin layer of semiconductor between a larger bandgap semiconductor and the potential energy well can be in the conduction band for electrons or less commonly in the valence band for holes. The specific energies in the structure can be engineered by material selection, well thickness, and layer dopant. In III-V semiconductors, these properties can be precisely controlled by the growth process, typically Molecular Beam Epitaxy (MBE) [9] or Metal-Organic Chemical Vapor Deposition (MOCVD) [12]. These structures are used for photon emission devices like Light Emitting Diodes (LEDs) [13], Semiconductor Lasers [14], and Quantum Cascade Lasers (QCL) [15] as well as photon absorption devices.

The subject of this dissertation is the Quantum Well Infrared Photodetector (QWIP), which is a multi-layer stack of quantum wells that is biased [1]. This is an intersubband photodetector and absorbed photons excite electrons and either go directly into the conduction band or tunnel into it, as shown in Figure 2.

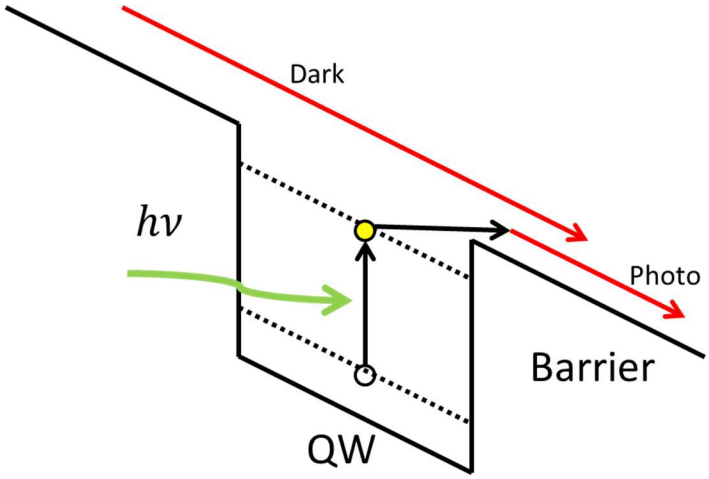

Figure 2 Diagram of Origin of Photocurrent in biased Quantum Well

There are two main types of quantum wells: Bound-to-bound and bound-to-continuum [16]. Bound-to-bound has two bound electron energy levels, the higher of which is close to the conduction band where electrons can easily tunnel when the device is biased. Bound-to-continuum has one bound state and electrons are excited directly into the conduction band as shown in Figure 3.

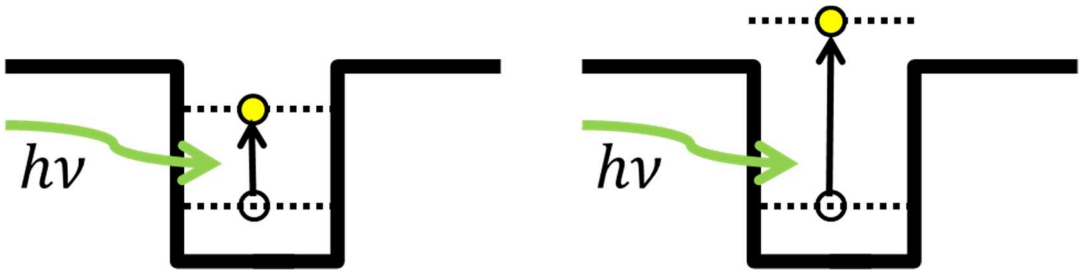

Figure 3 a) Diagram of Bound-to-Bound Quantum Well Absorption b) Diagram of Bound-to-Continuum Quantum Well Absorption

Bound-to-continuum QWIP have the advantage of needing a much lower bias for photocurrent because no tunneling is required for excited electrons. However, for this same reason, there is much larger dark current. Bound-to-bound QWIP has the advantage of having a significantly smaller dark current for the same reasoning. After the increase in bias, the responsivity is not much different and thus has a superior signal-to-noise. Also, bound-to-continuum QWIP is about

three times more broadband than comparable material bound-to-bound QWIP, which can be a disadvantage depending on the application. [16]

Despite its relative ease of fabrication (cheap and common materials), one big disadvantage of QWIP is weak and polarization-dependent absorption. Electron Quantum Wells only absorb electric field perpendicular to the direction of growth. This means that the array of MESAs that compose a typical Focal Plane Array (FPA) won't absorb any incoming radiation. Also, the absorption that is there is very weak; For example, the QWIP system used in the experiments and designs contained in this document has about an order of magnitude smaller absorption coefficient than state-of-the art HgCdTe which absorbs in all directions.

One traditional way to address this is with a 45° surface, as drawn in Figure 4. Polarized radiation is coupled into a waveguide made of the substrate or the QWIP itself and Electric Field with a vector component in the z-direction can now be absorbed by the QWIP. This is an effective way to test a new material, but fabrication is too complicated to be incorporated into an FPA. To practically make a camera, some alternative form of coupling must be implemented. [17]

A much simpler way to couple light into a QWIP FPA is to incorporate some kind of scattering element or array, as drawn in Figure 4. One way to do this is with an optical grating made of metal on top of the pixel [18]. This can result in roughly double the responsivity from the same QWIP stack with 45° edge coupling. However, because the scattering in the case of the coupler is very directional, it only allows for one or two passes of diffracted radiation. This issue can be solved with a random scattering pattern. The optimum way of doing this is with a designed quasi-random mask that allows for the maximum number of passes in incoming radiation and doesn't cluster the scattering elements [19].

Figure 4 a) 45° coupling to QWIP used to test single pixel b) random scattering to QWIP pixel

B. Derivation of Specific Detectivity (D^*)

Quantum Well Infrared Photodetectors have relatively weak absorption compared to other types of photodetectors. In a traditional set-up, like 45° coupled QWIP, we can simply use Beer's law to describe the internal quantum efficiency [20], that is, the number of photons in the system converted to photocurrent:

$$\eta = (1 - e^{-2\alpha t})/2 \qquad (1)$$

This method is a good way to characterize a material, but is not useful for nearfield coupling mechanisms. A more rigorous method for calculating quantum efficiency is required and discussed in Section III.

Semiconductor optical gain (or just gain) is the factor by which current is multiplied in a semiconductor. In QWIP, a small fraction of current (the capture probability, p_c is captured by the individual quantum wells. The gain is based on this and the number of quantum wells, N.

$$g = \left(\frac{1-p_c}{p_c}\right)\frac{1}{N} \qquad (2)$$

The figure of merit that determines the overall signal generated in an infrared detector is Responsivity, which is fundamentally the amount of photocurrent generated for a given incident power [20]. For QWIP, responsivity (in A/W) is defined as [2]:

$$R_i = \frac{\lambda\eta}{hc} qg \qquad (3)$$

Ultimately, we are concerned with the amount of photocurrent we can distinguish from other sources of current (noise current). The RMS-noise current is defined as the combination of all sources of noise current [2]:

$$I_N^2 = 2qg(I_D + I_B)\Delta f \quad (4)$$

I_D is dark current, current due to thermally excited carriers while the device is biased, I_B is background photocurrent, current due to photo-excited current due to background radiation (not signal), and Δf is the measurement bandwidth. There are other sources of current in photodetectors that can contribute to noise, but in QWIP they are small enough to ignore. Of the two mentioned, generally, one source of current is typically large enough to make the other

source negligible. In standard QWIP operation, dark current is typically the limiting factor. This current is due to thermal generation and recombination of carriers across a detector [2]:

$$I_D = (G + R)Vqg \qquad (5)$$

G and *R* are the Generation and Recombination volume rates respectively and can be considered roughly equal ($G \cong R$). *V* is the electrical volume of your detector. Also, to note is the gain. This can't be measured directly, but the dark current and RMS noise current can. The dark current is simply a DC measure when the device isn't illuminated. The RMS Noise current is a can be measured directly as well, however, one must note noise generated from the amplifier and measurement setup to extract the true value. To see how temperature affects carrier generation and dark current, we expand this expression [21]:

$$I_D = q v_{drift} A_e \left(\frac{m_B k_B T_{OP}}{2\pi\hbar^2}\right)^{\frac{3}{2}} e^{-\frac{\Delta E}{k_B T_{OP}}} \qquad (6)$$

Some of these parameters are related to material properties, which is beyond the scope of this document, but the parameter to note for us is the strong dependence on operation temperature, T_{OP}. At typical operation there are excess excited carriers in the QWIP due to thermal excitation that cause an increase in the generation rate and thus dark current. Due to this effect on dark current, QWIPs are typically cooled with liquid nitrogen down to 77K.

A typical goal of a new photodetector is to get the highest amount of signal to noise possible. A standard way to represent signal to noise in IR detection is Specific Detectivity (D^*) which normalizes for measurement bandwidth and device area, which are considered in rms-current noise but not in responsivity.

$$D^* = \frac{R_i}{I_n}\sqrt{A_O \Delta f} \qquad (7)$$

When the dark current is the main source of noise in a detector, the specific detectivity is:

$$D^* = \eta \frac{\lambda}{hc}\sqrt{\frac{1}{2(G+R)t}}\sqrt{\frac{A_O}{A_e}} \qquad (8)$$

which has the unit $\mathrm{cm}\sqrt{\mathrm{Hz}}/\mathrm{W}$. In a traditional QWIP, the optical and electrical areas are equal, removing the last term. Very simply, in traditional QWIP, the balance is between thermal generation in the material (caused by temperature), material thickness, and quantum efficiency (which due to beer's law increases with thickness).

C. Background Limited Infrared Photodetection (BLIP)

Depending on the material properties and the coupling mechanism of the detector, the advantage of cooling has a limit as photocurrent due to background radiation. This condition is called Background Limited Infrared Photodetection (or BLIP) and is the ultimate limit of a cooled detector and is not dependent on the temperature of the detector but rather the surroundings of the detector. This is shown in Figure 5, whereas the detector temperature rises, the dark current noise takes over and degrades performance.

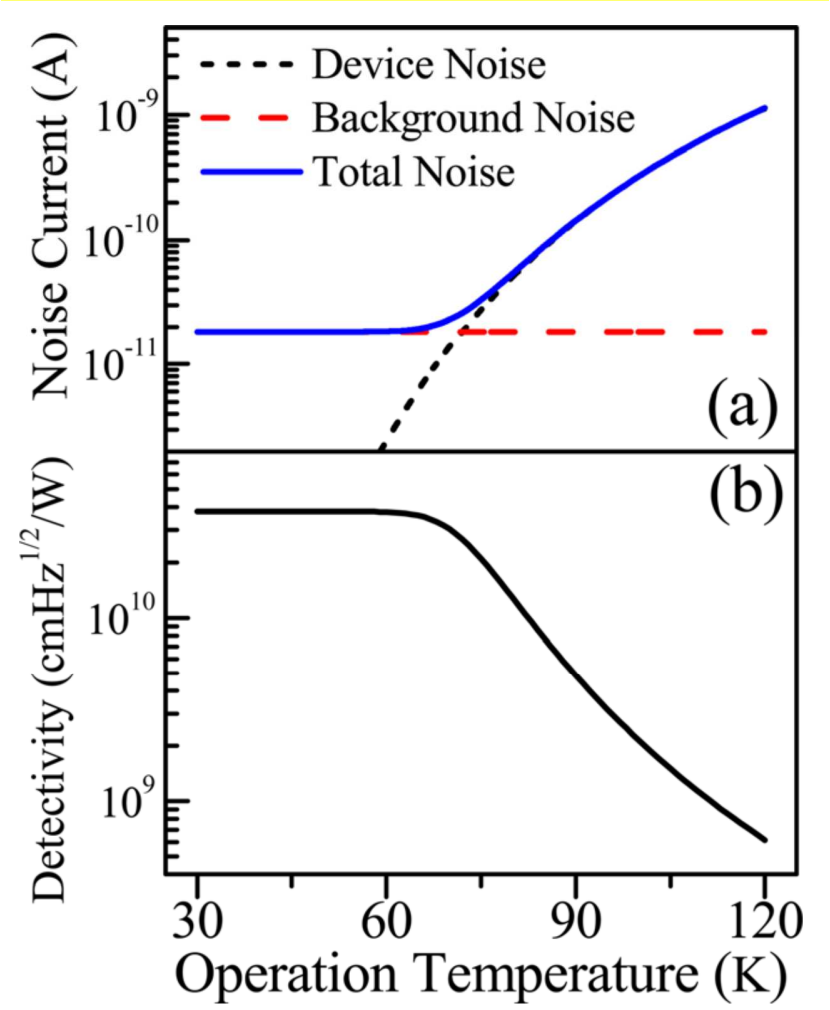

Figure 5 Temperature regimes of both noise current mechanisms

We will discuss background radiation coupling for more advanced structures in section III, but for a more traditional detector we can consider the background radiation photocurrent to be [21]

$$I_B{}^2 = 4\eta\Phi_B A_O g^2 q^2 \Delta f \qquad (9)$$

where Φ_B is the photon flux on the surface of the detector. The internal mechanism of carrier generation is the same for background radiation as it is for signal, however, the source is different. The signal is typically focused from a lens whereas the background radiation is generated from the detector's surroundings, and the radiation of the background is typically around the absorption range of our detectors (mid- to long-Infrared). Detector dimensions do not affect background radiation detectivity directly (but may be relevant to the quantum efficiency) and neither does device temperature, meaning that once a detector is cooled to its BLIP temperature, any subsequent cooling does not have any positive effect:

$$D^* = \frac{1}{2}\frac{\lambda}{hc}\sqrt{\frac{\eta}{\Phi_B}} \qquad (10)$$

For a traditional detector, the photon flux density is the integral of the solid angle that the detector sees. With no cold shield, the detector will have a 90° field of view (FOV), but with a shield it can be less. [2]

$$\Phi_B = \int \frac{I_\nu(\nu,T)}{h\nu}\,d\nu \int d\Omega = 2\pi \int \frac{I_\nu(\nu,T)}{h\nu}\,d\nu \int_0^{FOV} \sin(\theta)\,d\theta \qquad (11)$$

We can see D^* enhancement with a limited cold shield FOV in Figure, where relative D^* is plotted against FOV:

$$\frac{D^*(FOV)}{D^*(90°)} = \sqrt{\frac{1}{1-\cos(FOV)}} \qquad (12)$$

This relationship is shown in Figure 6.

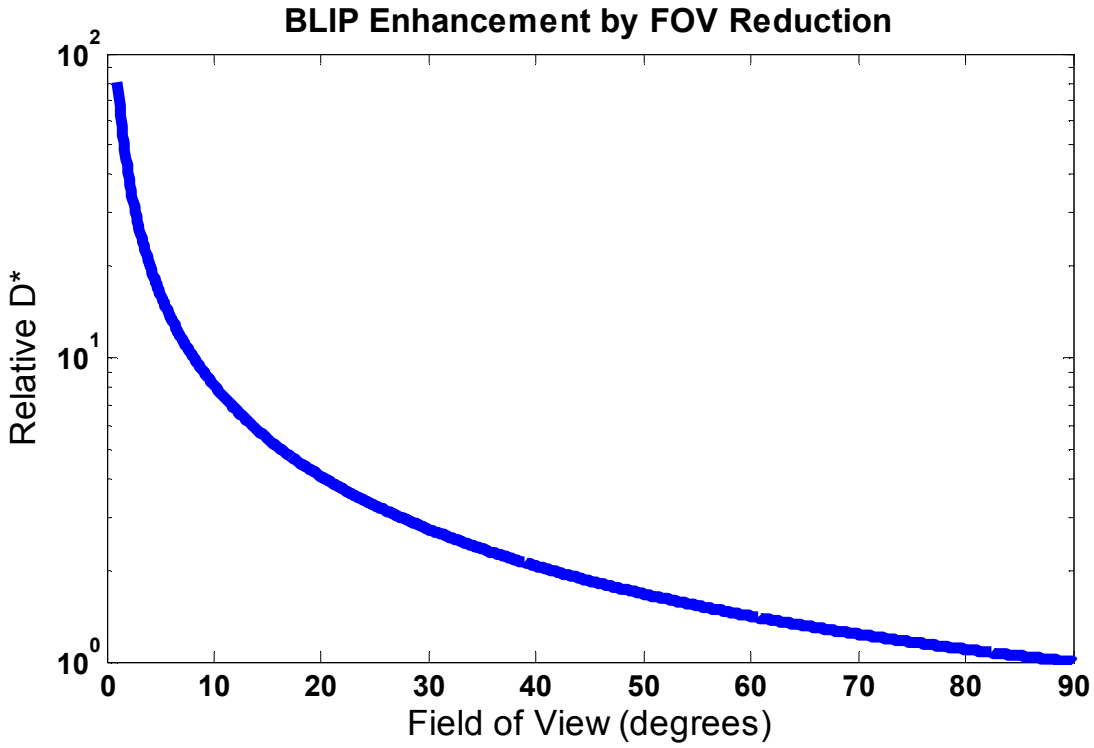

Figure 6 Effect of Field of View on QWIP performance in BLIP regime

III. Advanced Coupling for QWIP

Ultimately, QWIP FPAs made as MESAs are limited by weak signal and are not comparable to state-of-the art HgCdTe bulk detectors [2]. We propose using optical antennas for enhancement of QWIP. Optical antennas and more generally, metal optics, have a plethora of applications that can directly benefit QWIP. They can be used to re-direct light to have the proper polarization [22], they can locally enhance [23], they can resonate to form a cavity [24], and they can be used to extend concepts from microwave electronics into the infrared domain [25] [26]. In this section we explain why the use of antennas for enhancement, beam-forming, and shrinking detectors are extremely beneficial to QWIP, both to address typical concerns in infrared detection, and to extend the function of them beyond typical considerations.

A. Infrared Antennas

Antennas are engineered, metal-based structures that can collect or transmit radiation. They can be designed in a variety of shapes and forms for a variety of applications, for specific frequencies of radiation, and for specific angular spectra of reception and emission [27]. Initially, antennas were designed for radio frequencies but have since been extended to higher frequencies into the Microwave and Terahertz thanks in part to the development of microstrip technology [28].

Concepts from microwave circuits have recently been extended to infrared and optical frequencies to enhance traditionally photonic applications. Instead of coupling to and from a circuit operating at the antenna frequencies, these antennas enhance local fields or couple to a DC load like a thermal detector [29].

Great strides have been made in demonstrating infrared antennas for active photonic applications like beam-forming [26] and detection and passive infrared antennas and frequency selective surfaces for reflective and transmission frequency [30] and polarization control [22], demonstrating the extension of microwave concepts to photonic applications.

We are interested in taking this a step farther and extending these ideas to III-V QWIP used to make cameras. These antennas and systems can not only address common problems and enhance properties of infrared detectors but also can enable some interesting applications not previously thought of.

B. Small Volume Infrared Detectors Enabled by Antennas

One of the limiting factors in QWIP is high dark current. Above the BLIP temperature, this is the dominant source of noise. This is especially a problem in the case of bulk QWIP, as there is a lot of material generating noise, sometimes tens of microns thick. The square of RMS noise current for thermally generated current is directly proportional to electrical volume:

$$I_D{}^2 \propto A_e t \qquad (13)$$

This is one of motivations of antenna-enhanced QWIP. The easiest way to address this would be to just worry about thickness. One could make one or two orders of magnitude thinner QWIP in a traditional MESA structure and implement a coupling mechanism on top that enhances directly at the surface, such as a resonant plasmonic mode. Such a plasmonic mode would rapidly decay from the surface, so not only is there a reduction in dark current noise, but there is no benefit to having more absorbing thickness.

An improvement to take this idea one step further would be to reduce the electrical area without reducing the optical area.

$$D^* \propto \sqrt{\frac{A_O}{A_E}} \qquad (14)$$

This means that the optical collection area should be relatively bigger than the electrical area, either separate or within. Holes, pillars, or other arbitrary patterns within a periodic or single element would demonstrate this benefit. Also, a delocalized large collection area directed towards a small absorber could benefit from this principle.

With these antenna-coupled and waveguide coupled systems, the standard beer's law formulation for quantum efficiency is insufficient. A more rigorous analytical formulation is required to determine this in simulation. Quantum Efficiency in terms of a photon absorber, is the percentage of photons converted to excited electrons (or holes in the case of p-type absorber) which directly comes from the power absorbed by light in the volume.

$$P_{abs} = \int \alpha I(\vec{r}) d^3 r \qquad (15)$$

The quantum efficiency would just be this power normalized to the input power:

$$\eta = \frac{P_{abs}}{P_0} \qquad (16)$$

In QWIP, the absorption of light only occurs in the z-direction, so it is necessary to consider the intensity in terms of this component of the electric field. [31]

$$\eta = \frac{\alpha}{P_0} \int \frac{nc\varepsilon_0}{2} |E_z(\vec{r})|^2 d^3r \qquad (17)$$

Depending on the specific design, such as a periodic array for example, it may be more convenient to put this formulation in terms of incident electric field.

$$\eta = \frac{n\alpha}{AE_0} \int |E_z(\vec{r})|^2 d^3r \qquad (18)$$

A is the optical area that the incident field, E_0 is projected onto.

C. BLIP Performance Improvement

The Power of blackbody radiation emitted from a surface is:

$$P = \iiint \frac{\varepsilon 2h\nu^3}{c^2\left(e^{h\nu/kT}-1\right)} d\nu d\Omega dA \qquad (19)$$

This is the power emitted from a surface with an emissivity, ε, to a solid angle of Ω. Emissivity is often simplified to a constant between zero and one, but in our case, we're considering a frequency dependence.

At thermal equilibrium between this surface and its surroundings, the amount of thermal radiation emitted by a surface is equivalent to the amount it receives from a hemisphere of background. If this same surface is cooled to 0K, but the surroundings remain the same, it still receives this same radiation.

The mechanism of interest in evaluating the different noise sources is carrier generation which in the case of background radiation is optical instead of thermal, unlike the case for dark current noise. For a detector receiving blackbody radiation, the carrier generation rate per volume is:

$$G_{back} = \iiint \frac{2\nu^2 \alpha(\nu)}{nc^2\left(e^{h\nu/kT}-1\right)} d\nu d\Omega dA \qquad (20)$$

This is for a bulk material, considering the absorption spectrum $\alpha(\nu)$ in cm^{-1}. A more general expression which is required for a structure with an alternative coupling structure, such as an antenna would account for dimensionality and quantum efficiency. Even more generally, when dealing with antennas, we consider the antenna efficiency, η_a, which defines the amount of power collected by the antenna and converted to photocurrent:

$$\eta_a = \frac{P_{Abs}}{P_0} \qquad (21)$$

$$\mathrm{G_{back}} = \frac{1}{\mathrm{V}} \iiint \frac{\nu^2 \eta_a(\nu,\theta)}{\mathrm{c}^2\left(\mathrm{e}^{\mathrm{h}\nu/\mathrm{kT}}-1\right)} \mathrm{d}\nu \mathrm{d}\Omega \mathrm{dA} \qquad (22)$$

The area integral can be separated from the total integral, as any variation would be considered in the function for quantum efficiency. In terms of rate of total photons absorbed:

$$\mathrm{N_{back}} = A_o \iint \frac{2\nu^2 \eta(\nu,\theta)}{\mathrm{c}^2\left(\mathrm{e}^{\mathrm{h}\nu/\mathrm{kT}}-1\right)} \mathrm{d}\nu \mathrm{d}\Omega \qquad (23)$$

Finally, we have a general expression for BLIP detectivity in terms of photons generated due to background radiation that can be applied to antenna-coupled QWIP.

$$D^*_{BLIP} = \frac{\eta(\nu_0,\theta_0)}{h\nu_0} \sqrt{\frac{{A_O}^2}{A_E N_{back}}} \qquad (24)$$

Keeping in mind that in an antenna-coupled system, the quantum efficiency is simply the antenna efficiency in delivering energy to the detection medium, we can immediately see the advantage in having a narrowband, directional antenna. High directionality eliminates the amount of background radiation accepted by the detector, and a sharper resonance limits the spectrum of photons that can be converted to noise current.

Sometimes, the quantum efficiency frequency and angular spectrum are so discrete that they can be separated into the frequency spectrum and the normalized directive gain of the antenna system at the desired frequency. Directive gain, $D(\theta)$, represents the power density over a given solid angle in the far field. This can be used to represent the angular response of quantum efficiency

$$\eta(\nu,\theta) \cong \eta(\nu) \frac{D(\theta)}{D(0)} \qquad (25)$$

$$\mathrm{N_{back}} = A_o \int \frac{2\nu^2 \eta(\nu)}{\mathrm{c}^2\left(\mathrm{e}^{\mathrm{h}\nu/\mathrm{kT}}-1\right)} \mathrm{d}\nu \int_0^{2\pi} \int_0^{\pi/2} \frac{D(\theta)}{D(0)} d\theta \, d\varphi \qquad (26)$$

This approximation should be first verified before making this calculation.

A cold shield is a metal box cooled down, typically by liquid nitrogen, with an aperture opening towards a lens. In a non-antenna coupled setup, a cold shield is used to eliminate background radiation off-angle. Cold shields, however have three problems: 1) they add another element and associated size constraints to the optical system, 2) for practical reasons, the cold shield can't be brought very close to the lens due to size constraints and the IR-transparent window separating the cooled system from the optics, and 3) even if the cold shield could be brought directly to the lens, due to the nature of a large 2-dimensional array of detectors, they cannot fully limit the FOV of the detectors to the limit of the optical system and there will be variation in the noise across the array (Figure 7).

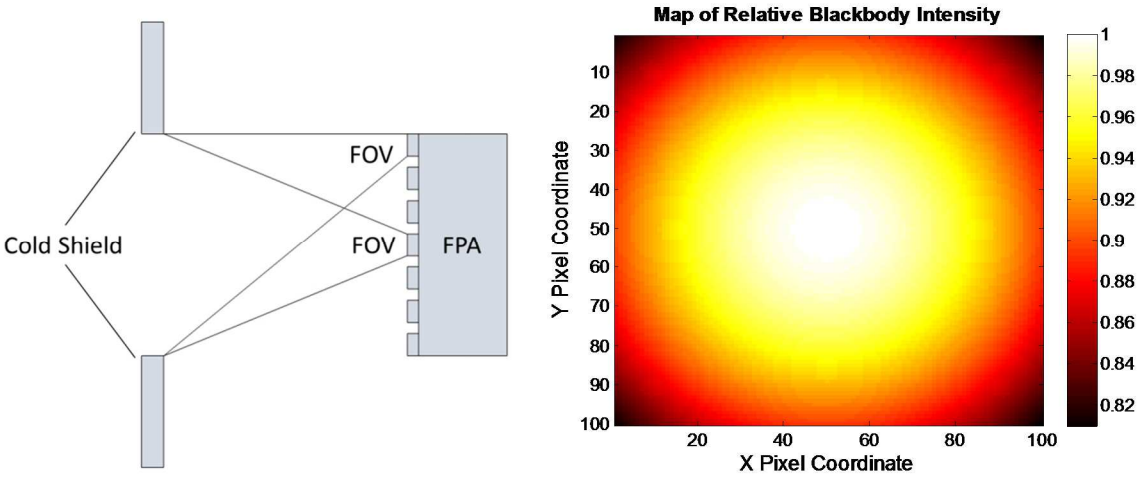

Figure 7 Effect of pixel position on background flux

In contrast, an integrated antenna can eliminate background radiation equally at the pixel level. As with the cold shield it will not contribute to background radiation as it is cooled at the chip level, but it is advantageous because it is integrated directly with the detector and doesn't require another bulky, system-level component.

We would also like to point out that theoretically, for a material with a very high thermal carrier lifetime, background radiation can be the dominant source of noise even at higher device temperatures. In fact, if we go as far as to say that if the device is at room temperature, the background radiation will still be the dominant source of noise. At thermal equilibrium, the amount of thermal radiation received by the detector is equal to the amount emitted. This means that the background generation rate is doubled from the case of the cooled detector and that the D^*_{BLIP} will only increase by a factor of $\sqrt{2}$.

D. Beam Forming, Synthetic Aperture, and Far Field Imaging

In the context of BLIP noise reduction, the goal is to shape a beam to be narrow, but still be centered at 0°, meaning the use of a symmetric structure. However, in using asymmetric or multi-input/output systems, beam forming is possible, and coupled with III-V photon detectors, specifically QWIP, can be used to really broaden the capabilities of infrared detection.

Beam Forming has previously been demonstrated at infrared frequencies in surfaces, and as discrete devices. The detecting devices however, have been thermal loads (microbolometers) [25] and rectifying loads (Metal-oxide-metal diodes) [32]. These devices are very interesting for very specific application, and have the advantage of being operated at room temperature. However, these detectors only have a Specific Detectivity of $D^* = 9.65 \times 10^6 \mathrm{cm}\sqrt{\mathrm{Hz}}/\mathrm{W}$ [33], not sufficient for image formation. The next step is to further extend these concepts to photon detectors and specifically use microstrip antenna-coupled QWIP as the enabling technology.

One technology this could be used for is synthetic aperture. In synthetic aperture, an array of angular sensitive arrays is swept or rastered, and given the known angular response, an image can be formed [34]. This concept has yet to be demonstrated in the infrared. A second technology is angular-sensitive cameras where each pixel has a unique and designed angular sensitivity. This concept has been demonstrated in the visible regime with complex gratings [35], but could also be used in the infrared using antennas.

These angular-sensitive patterns utilize two gratings to give each individual pixel a unique angular response, with multiple peaks, utilizing what's known as the Talbot Effect. [36] In the infrared, such gratings would take up ~20× more space and not be feasible for infrared imaging. However, with infrared antennas, individual pixels can have a tailored angular response without making one grating that effects the entire array. Figure 8 shows a concept for an antenna that will be expanded on in Chapter VII, but the motivation for such an antenna is clear here.

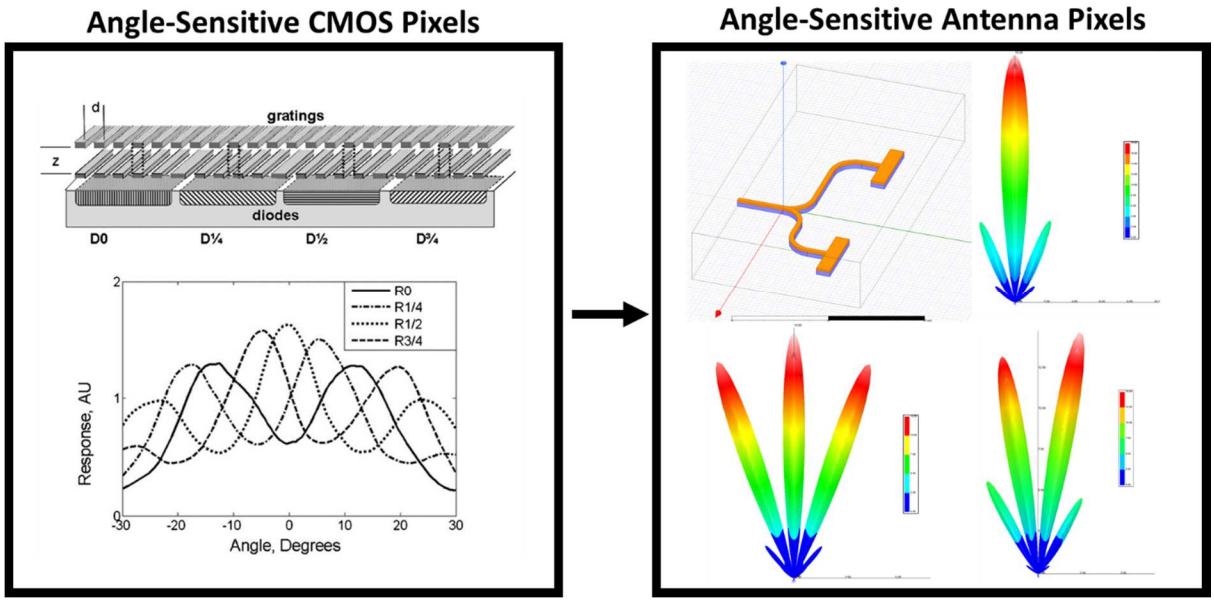

Figure 8 Extending Lensless Imaging to the Infrared with Antennas

In addition to these static-off angle concepts, we can consider active designs that can be tuned. Vanadium Dioxide (VO_2) has been shown to significantly change index and conductivity in the infrared. [37] [38] Adding this capability with these asymmetric off-angle devices could lead to a powerful imager that could look in multiple directions depending on how exactly this is applied as illustrated in Figure 9.

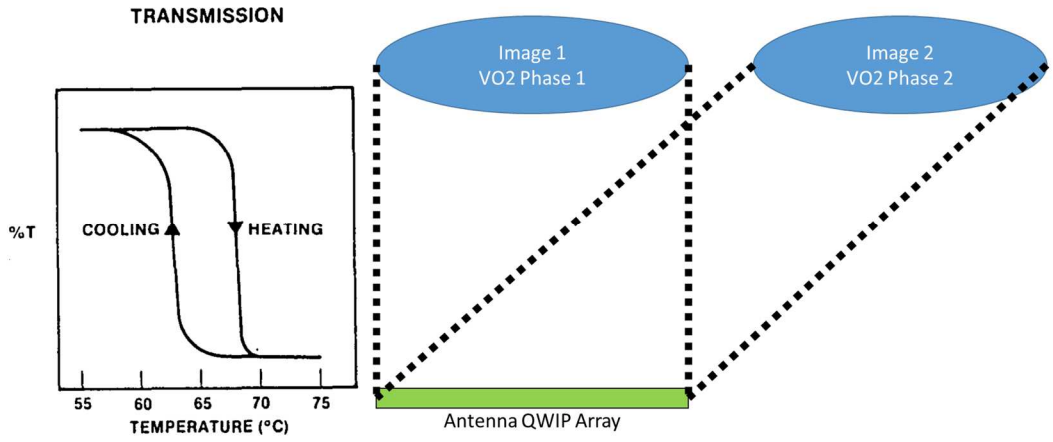

Figure 9 Extending Lensless Imaging to the Infrared with Antennas

In the infrared, a polarized heat signal has already been demonstrated that can be viewed/decoded from a heated surface. [39] If we take these asymmetric antenna-coupled QWIP but replace the QWIP with an emitter in similar wavelengths like a quantum cascade laser [40] , we can send the beam instead of detecting and image. Using just static antennas, without a

heated surface you could construct a similar image in the far field. Using the phase-changing properties of VO_2, multiple images could be projected onto the far field using similar math and algorithms used to construct images with lensless CMOS cameras.

IV. Fabrication of Embedded Antenna Quantum Well Infrared Photodetectors

A. Top-Side Antenna-Coupled QWIP

In 2010 a device was presented by our group at Northwestern that used a Plasmonic structure to enhance QWIP for the first time [41]. The structure was made on top of 500nm of InGaAs Quantum wells with InP barriers tuned to 8μm radiation. This acted both as an antenna and a top contact. The structure was made from an array of holes in a 100nm sheet of gold and was based on the concept of extraordinary optical transmission where a hole array in gold supports a surface plasmon resonance on coupled to both sides of the film. This structure is advantageous for QWIP due both to the localization of radiation and the redirection of k such that the electric field of incoming radiation is parallel to the direction of growth (necessary for absorption). This design is shown in Figure 10.

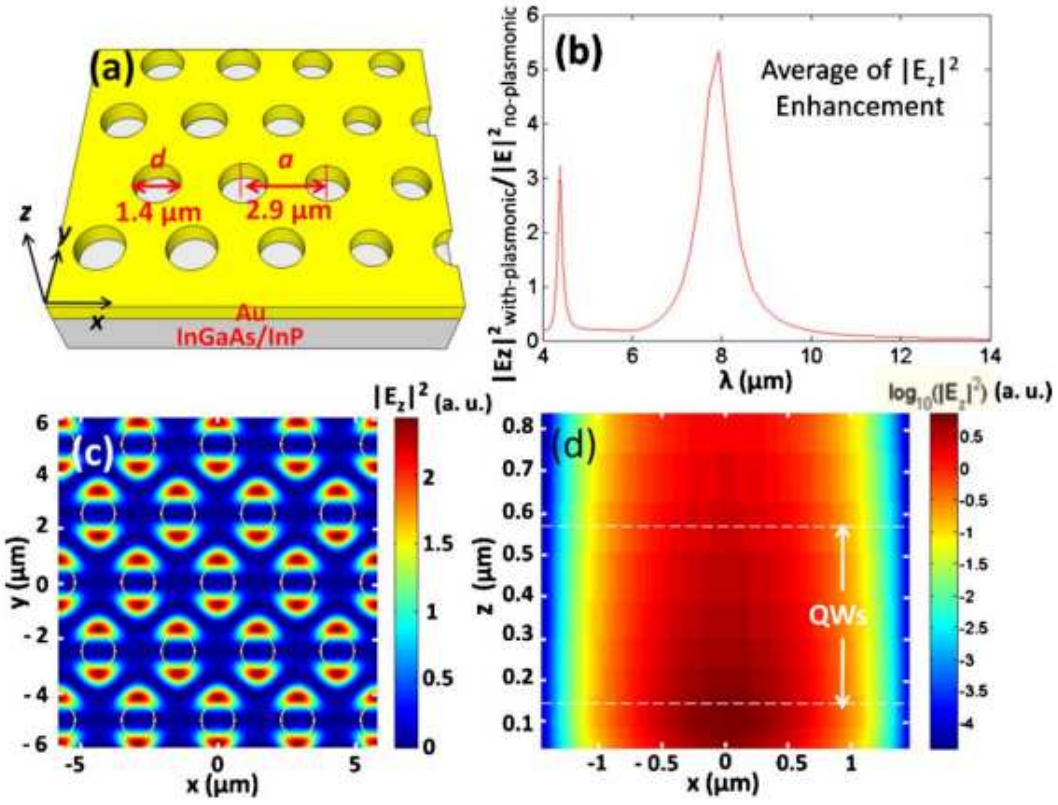

Figure 10 a) Design and Structure of Plasmonic-Enhanced QWIP b) Electric Field Enhancement c) z-polarized intensity map d) lateral intensity over hot spot

A well-known InP/InGaAs QWIP system designed for 8μm radiation was used in this project [42]. As discussed previously, thin QWIP can lead to lower dark current. In this case, instead of 50 or 100 layers of quantum wells, 8 were used. Figure shows a cross-sectional SEM of the layers. The bright regions are InGaAs and the darker regions are InP. All-in-all there's 444.8nm of QWIP absorber that contributes to dark current between the InGaAs contact layers (Figure 11).

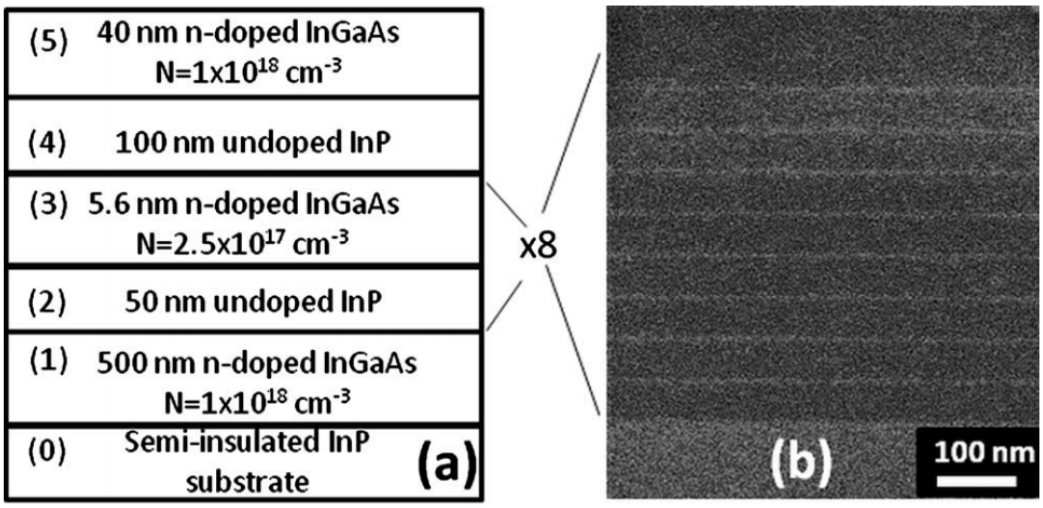

Figure 11 QWIP Layers

This structure was made into MESAs ranging from 250μm x 250μm to 25μm x 25μm. The top contact of the MESA was made of 100nm gold and milled with FIB to make the hole-array antenna (Figure 12). This was designed to resonate at with 8μm radiation.

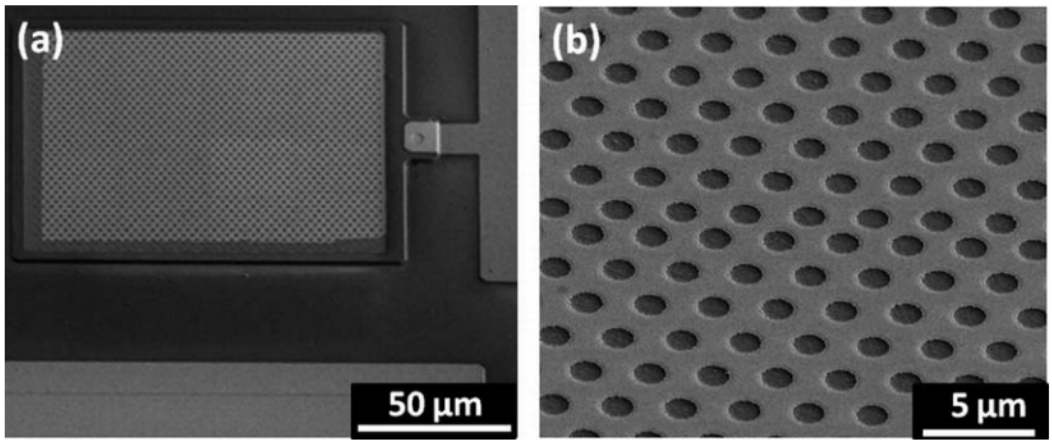

Figure 12 a) SEM image of plasmonic-enhanced QWIP MESA b) close-up SEM of plasmonic structure on QWIP

At 78K (liquid nitrogen), the peak responsivity was reported to be 7A/W at 8μm and a Specific Detectivity of $7.5 \times 10^{10} cm\sqrt{Hz}/W$.

B. Embedded Antenna-Coupled QWIP Design

This device was a great step forward in enhanced QWIP, but had its shortcomings: It could not be contacted from the top which is required to make a camera as this would destroy the plasmonic antenna. Side-contacting would greatly reduce the fill factor in an FPA configuration. Also, due to the extreme localization of E_z at the edges of the holes, there is a lot of non-absorbing material that contributes to dark current but not to quantum efficiency. As limited as the dark current is by the thinning of the absorber, removal of "dead" space would have a large impact.

To overcome these issues, we designed a small-volume/limited area QWIP with an embedded antenna (Figure 13). The metal hole array is embedded within the detector such that the absorbers are cylinders within the antenna which doubles as the ground for the device. All the cylinders in the pixels are connected at the top by a layer of gold that doubles as a top contact and as an optical ground plane/mirror to further enhance E_z in the QWIP.

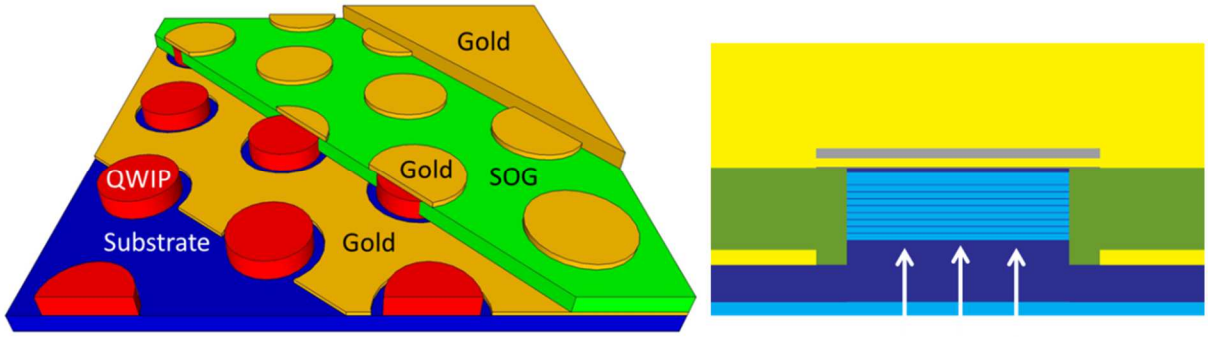

Figure 13 a) Peel-back cross-section of Embedded QWIP structure b) cross-section of single embedded QWIP pillar

Surrounding the pillars, and filling between the antenna and the top contact is a dielectric that's transparent at 8μm. The original plan was to use Spin-on-glass, but we found that there was too much absorption at the wavelengths of interest. However, no matter the material we use, the concept above is valid. This device is to be backside-illuminated.

This structure has a 72% reduction of area (and thus dark current) and a 10x field enhancement at the peaks. This device also uses a self-alignment process to define the antenna, that is, only one submicron lithography step is required. [43]

C. Pillar and Antenna Fabrication

A three-dimensional structure like this requires novel fabrication and many interacting processes. This is not simply a matter of making a MESA or a modified MESA, but requires a coupling structure inside of a "super-pixel" with contacts on two different planes.

The material system we use, InP-based III-V semiconductors, is etched by a plasma of Hydrogen (H_2), Methane (CH_4), and Argon (Ar). This process is very sensitive to organic residue on exposed semiconductor surface, something photolithography and electron beam lithography processes are prone to. A standard resist-lift-off process has three main steps: 1) lithographic definition of the metal regions, opening where metal is desired, 2) Metal evaporation, and 3) solvent lift-off removal of all organics taking waste metal away. Depending on the exposure technique and process parameters used, Step 1 can leave behind residue in the open region, potentially affecting electrical contact, or worse, leaving the sacrificial and contact metals connected. Step 2 can heat up the device "burning" resist onto the sample leaving it remaining for Step 3 and subsequent etches.

To make the device described here, two novel improvements to the lift-off process were implemented. The first is the inclusion of a dielectric bi- or tri-layer buffer between the semiconductor surface and the photoresist layer. This consists of a 250-300nm layer of SiO_2 on the bottom and a 25-30nm layer of Si_3N_4. Before the metal deposition step, the whole system undergoes a combination CH_4 plasma and then HF etch to open the semiconductor structure, and undercut the Si_3N_4 structures respectively, leaving an open contact region completely untouched by organic material. The second improvement made to this process is the application of a thin metal selectively to the very top photoresist surface, to protect underlying photoresist from plasma processes, but will allow for lift-off. This metal is deposited at a very high angle not allowing it to enter the open areas. This process is shown in Figure 14.

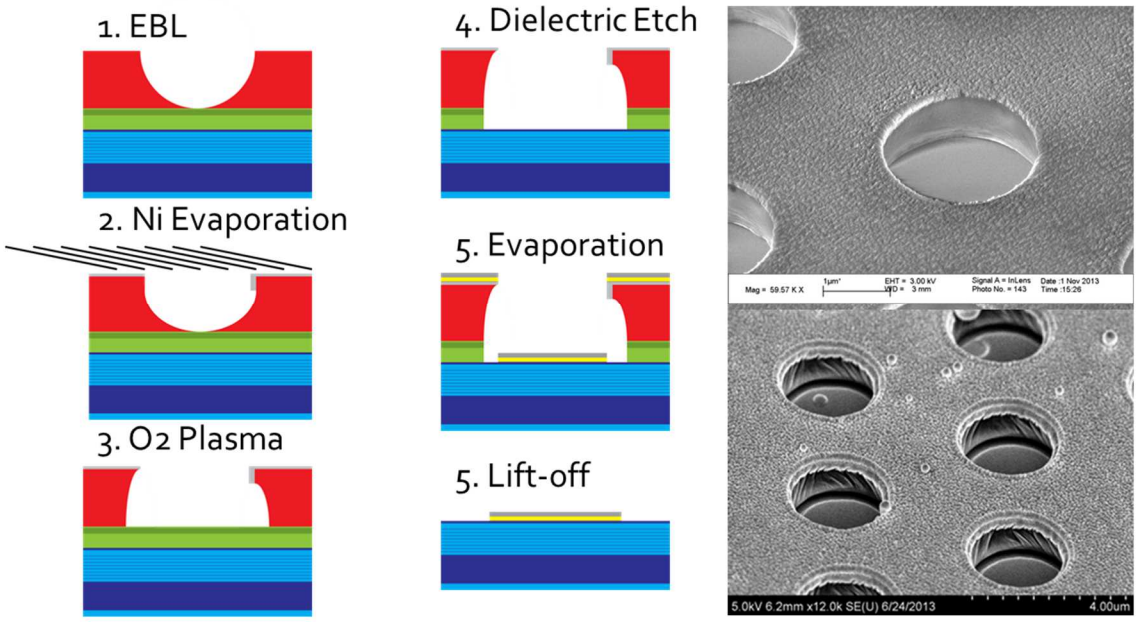

Figure 14 a) Process Flow of metal- and dielectric-assisted metal lift-off b) SEM of angle-evaporated Resist hole (step 3) c) Metal evaporation for QWIPs (step 5)

After lift-off of the top contact layers, the individual pillars are etched to separate all the quantum well absorbers. (Figure 15a) The next step was to make the antenna. This is done by electron beam evaporation which is inherently very directional. Because of this, any slight angle between the deposition source and the sample will lead to deposition on the pillar sidewalls and complete shorting. Due to this, undercut is required.

To completely expose the sidewall semiconductor surface for an undercut etch, metal-organics and semiconductor oxide RIE byproducts from the sidewall surfaces must be rigorously cleaned. To do this, a repeated three step process is applied: 1) Oxygen plasma, 2) Hydrofluoric Acid, and 3) Phosphoric Acid. These three processes are repeated six times and then three more times omitting step two. These steps, in conjunction with each other directly remove etching byproducts, or react with them such that they can be removed by subsequent cycles. The clean sidewalls are shown in Figure 15b.

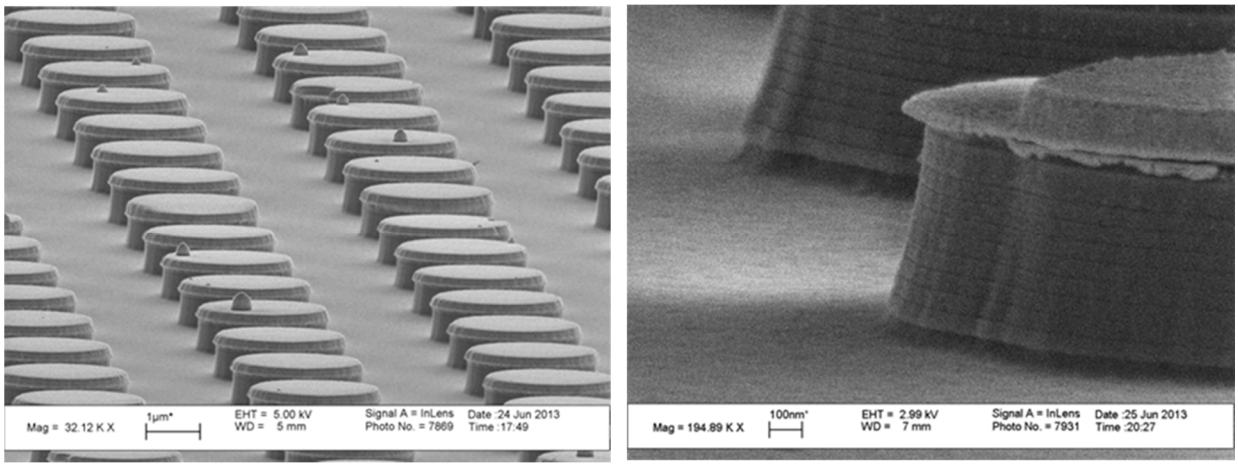

Figure 15 a) Etched QWIP pillar array b) QWIP pillars after side-wall cleaning process. The InGaAs is attacked slightly

Once the surface is clean, the sample is etched with Hydrobromic Acid (HBr) and Hydrogen Peroxide (H_2O_2). This combination non-selectively etches InP and InGaAs and is used to provide ~100nm of undercut for our structures (Figure 16b). With sufficient undercut, this detector has metal evaporated on it. No lithography is required as the top metal provides a "shadow" over the undercut semiconductor (Figure 16c).

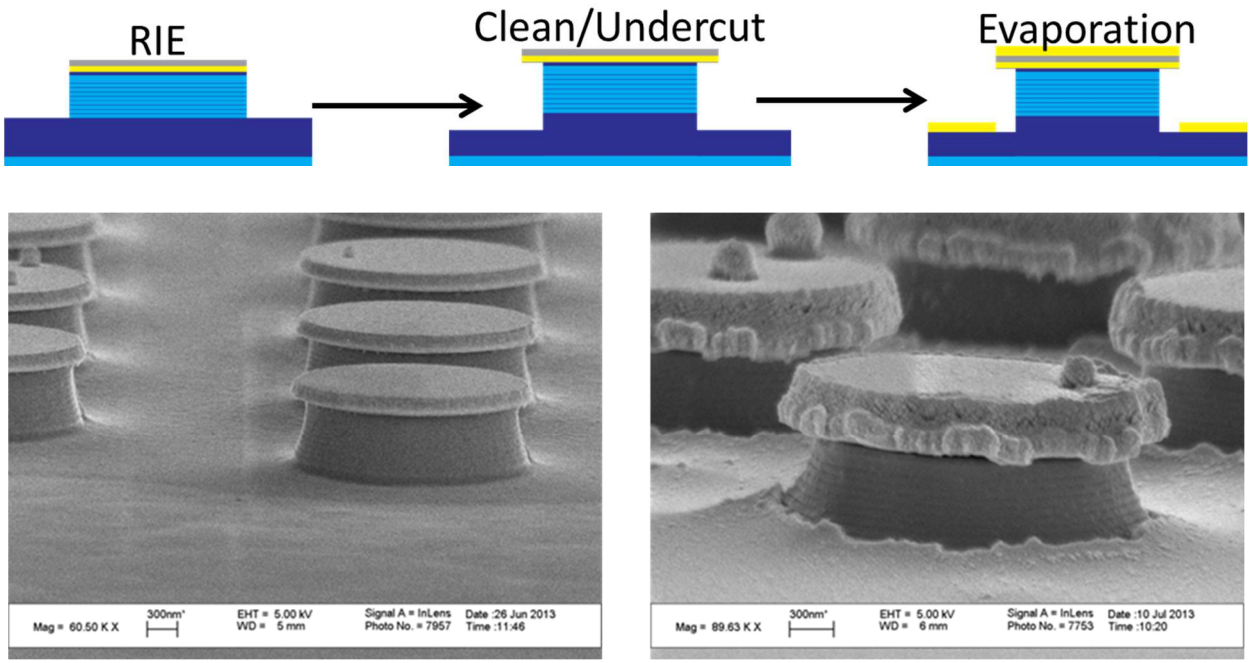

Figure 16) Undercut and self-aligned evaporation process b) QWIP pillars after HBr undercut etch c) self-aligned, or "shadow" evaporation

One other important consideration in making three-dimensional structures like this, especially when there's a lot of surface area connected in parallel, is metal evaporation quality. Any metal particles that can bridge between ground and contact will short the device, no matter how the device is planarized.

One issue that had to be overcome in the fabrication of these detectors was gold "spitting". The source in gold deposition will release clusters of gold that leave spheres on the surface being deposited on (Figure 17). This spitting is caused mainly by carbon contamination and can be reduced by cleaning the metal and avoiding carbon crucibles or just using a much bigger crucible that the beam can't contact.

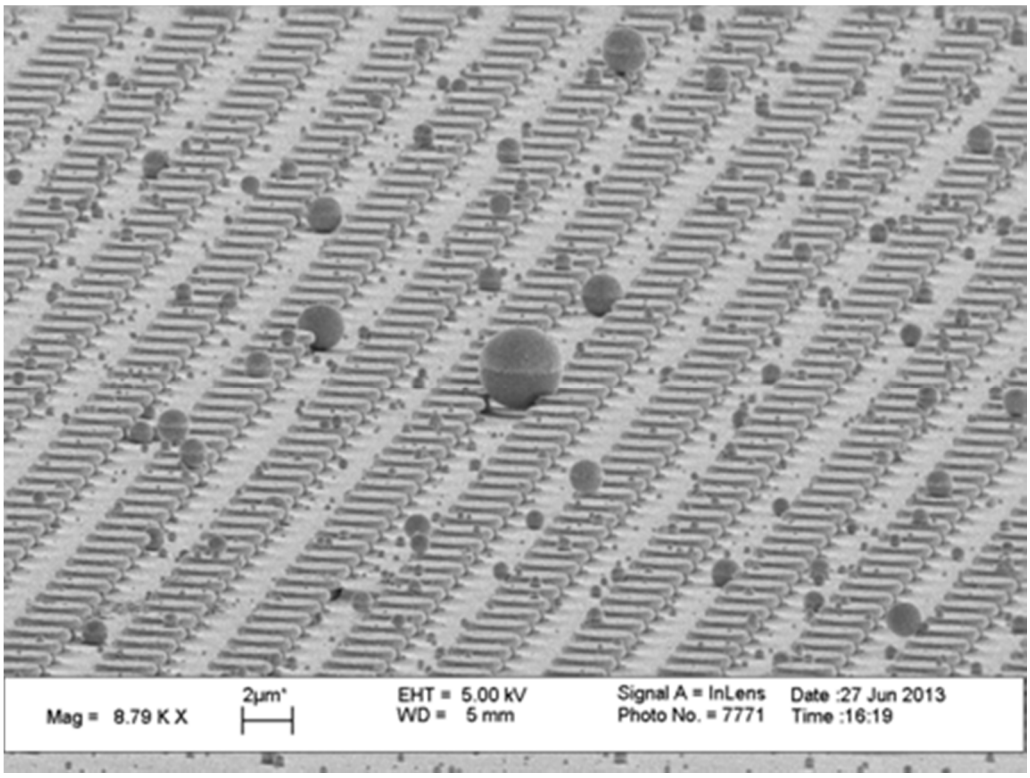

Figure 17 Gold spitting and its effect on QWIP pillars or 3D structures in general

D. Planarization and Top Contact Formation

One of the biggest difficulties in this process has been making top contact to the device and choosing an appropriate dielectric to surround the pillars. Initially, Hydrogen Silsesuioxane (HSQ) based Spin-on-Glass (SOG) was chosen for its mechanical and thermal stability. Un-cured SOG is not viscous and when spun on will planarize a surface very well. Once cured, SOG is mechanically very stable and will not be a major source of stress on the device or separate

from the device sidewalls. SOG also is chemically similar to SiO_2, a common material used in semiconductor processing due to its dielectric, optical, mechanical, and chemical properties.

This process was developed with QWIP in mind as well as another project related to 1550nm single photon detectors. Dissolved HSQ is spun onto the sample worth polarizing. At 3000RPM, the thickness is about 1.5um. This sample is then baked under a nitrogen ambient to avoid reacting with oxygen. The temperature is very slowly increased to prevent cracking and separation, two possible consequences of a sudden change in thermal stress. Figure 18 shows how effective this material is for planarization with two cross sections.

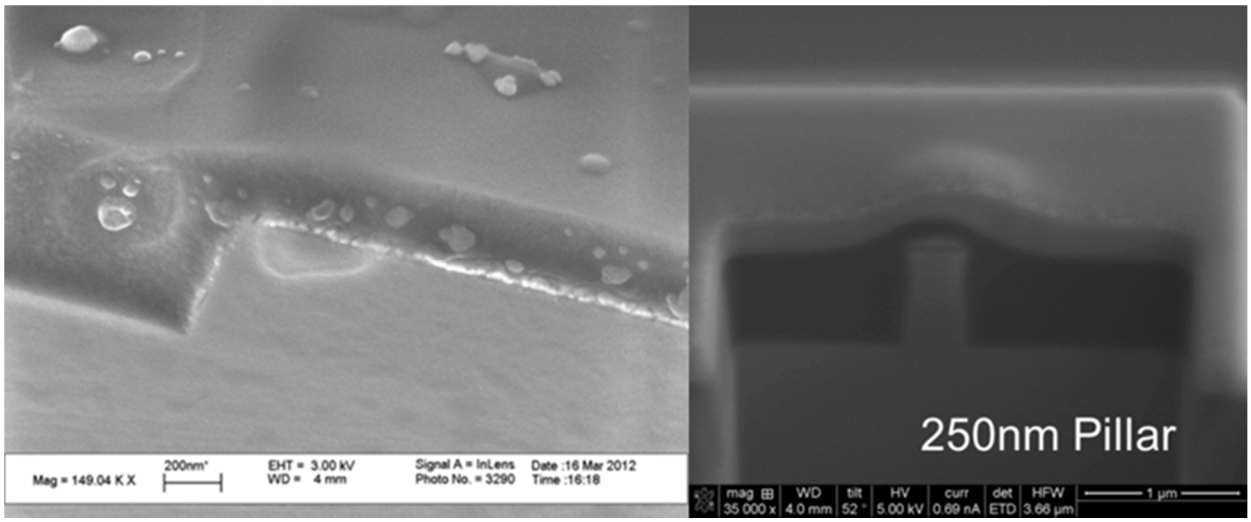

Figure 18 a) SOG planarization on semiconductor MESA b) submicron planarization capability of SOG imaged with a local ion-beam deposited Platinum patch and Focused-Ion Beam milling

After the SOG is cured, it can be etched back to expose the top contact. Because SOG is chemically very similar to SiO_2, the same CF_4-based plasma etch chemistry is used to etch it. The etch rate of this material is well-characterized and once it's close to the surface, the pillars can be checked using various methods, but we chose to use Profilometry. Figure 19 shows two examples of exposed pillars after etch-back, including one cross-section and one top view of an array.

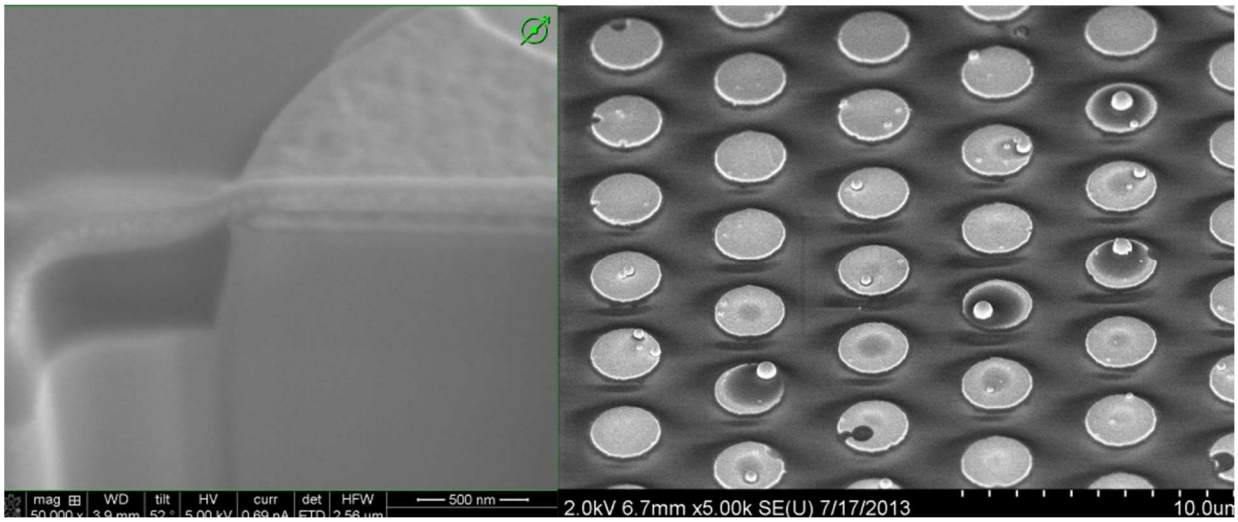

Figure 19 a) SOG etchback, planarizing to semiconductor pillar b) SOG planarization over QWIP pillars

Unfortunately, we found through further investigation that this material is too lossy for use at 8μm. The Si-O bond has a resonance in the mid-infrared and the absorption is too high to support any quality resonance.

As an alternative a sacrificial photoresist process was attempted. This process allows for the same process for pillar and antenna formation and is just an alternative for top contact formation. A thick photoresist is deposited everywhere after the antenna is deposited. Just like the SOG process, this is etched back to expose the top of the pillars. Thin Gold is deposited everywhere, and the device is patterned with thick photoresist and electroplated to form top contact. This resist is removed, the seed layer is removed. Finally, the initial sacrificial photoresist is removed to leave a "floating" top contact over the super pixel. This process is shown in Figure 20. [44]

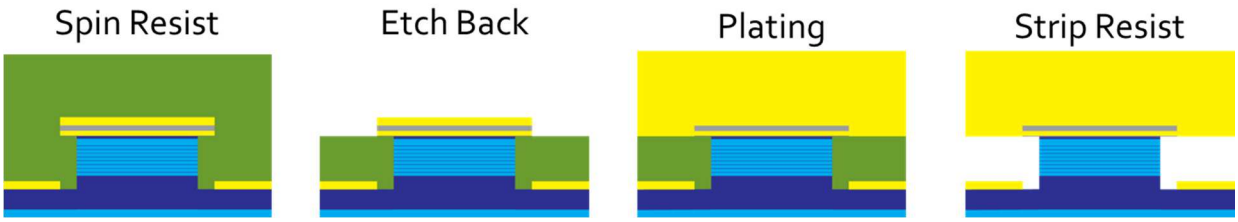

Figure 20 Process flow for sacrificial photoresist floating metal planarization

One major difficulty in this process was the plasma etch back. Oxygen and Argon plasma will etch organics easily; oxygen plasma is commonly used for photoresist removal in plasma ashers. However, the goal here wasn't complete removal, but partial, planar removal. This proved

difficult with the typical chemistry and left behind what looked like a shag carpet. This was fixed by including freon (CF_4) and a nice, smooth, planar etch-back was achieved (Figure 21).

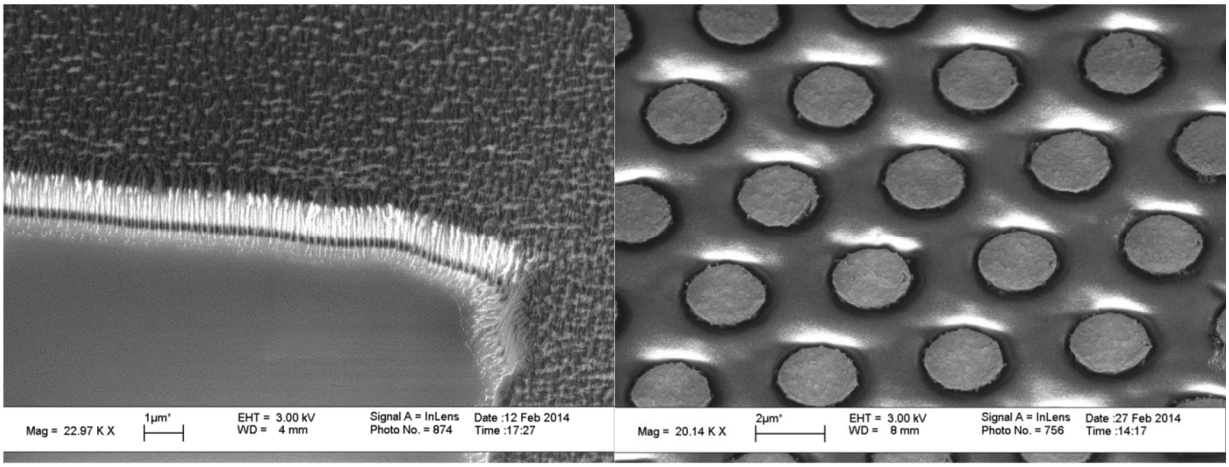

Figure 21 a) Photoresist Planarization Etched Back Photoresist after standard oxygen plasma. This recipe leaves a film resembling a "nano shag carpet" b) Smooth, successful photoresist planarization

This process had two major issues in the end. First of all, the electroplating process was undergoing development and the contact ended up being a very porous, particulate film which led to poor contact and shorting across the entire sample. The other major issue was with backside polishing. The Aluminum Oxide slurry left begind a film of particles everywhere that couldn't be reomved (Figure 22).

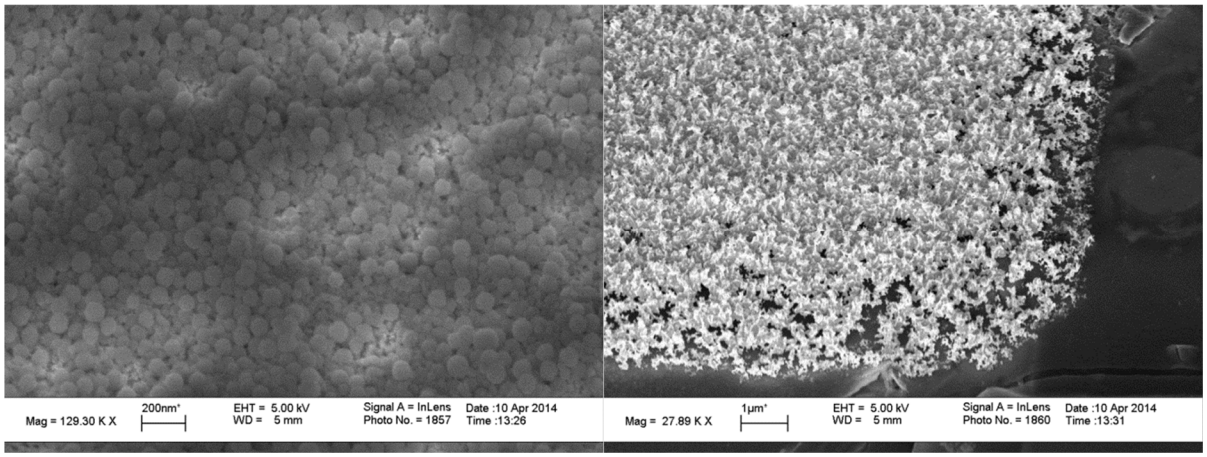

Figure 22 a) Layer of Aluminum Oxide particles on surface. b) Non-optimized electroplating process

E. Cold Welding for Top Contact Formation

In general it is difficult to precisely control processes involving double layers of photoresist seperated by thin gold and make a floating contact, so something more simple is desired. More recently we have attempted to fuse gold paterns with gold films, the idea being to use gold-to-gold cold welding to make a top contact supported by a second mechanical substrate. The other methods require for the top contact to be made monolithically, but this takes this step away and involoves a simple metal pattern definition on a separate substrate. These two sides are then welded together, as illustrated in Figure 23.

This process to pillar formation is fundamentally the same as the previous processes. However, there are extra steps that allow for contact to the ground layer. Due to the nature of the contact method, the ground contact on the device chip needs to be on the same plane as the top contact despite this being a vertical device.

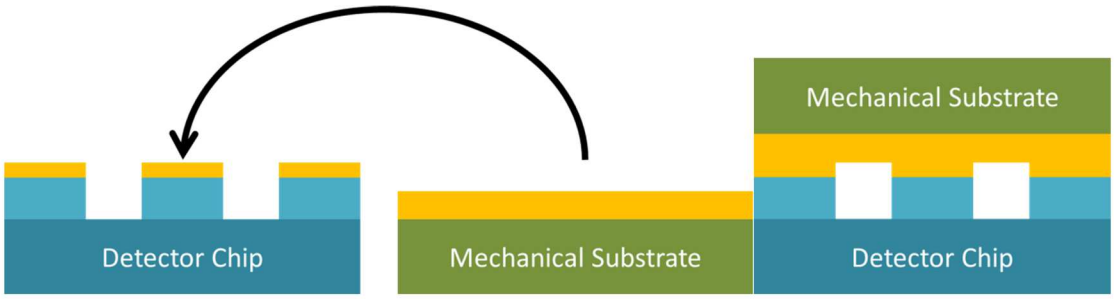

Figure 23 Concept of Bonding. Instead of making top contact monolithically, it's made on a separate chip and connected at the end

After the patterning and lift-off for the pillars, a dielectric the same thickness as this metal is deposited everywhere. This dielectric is patterned and etched, and there will be dielectric everywhere that will contact to ground as illustrated in Figure 24. This pattern also doubles as an RIE mask and will leave untouched QWIP wherever there will be ground.

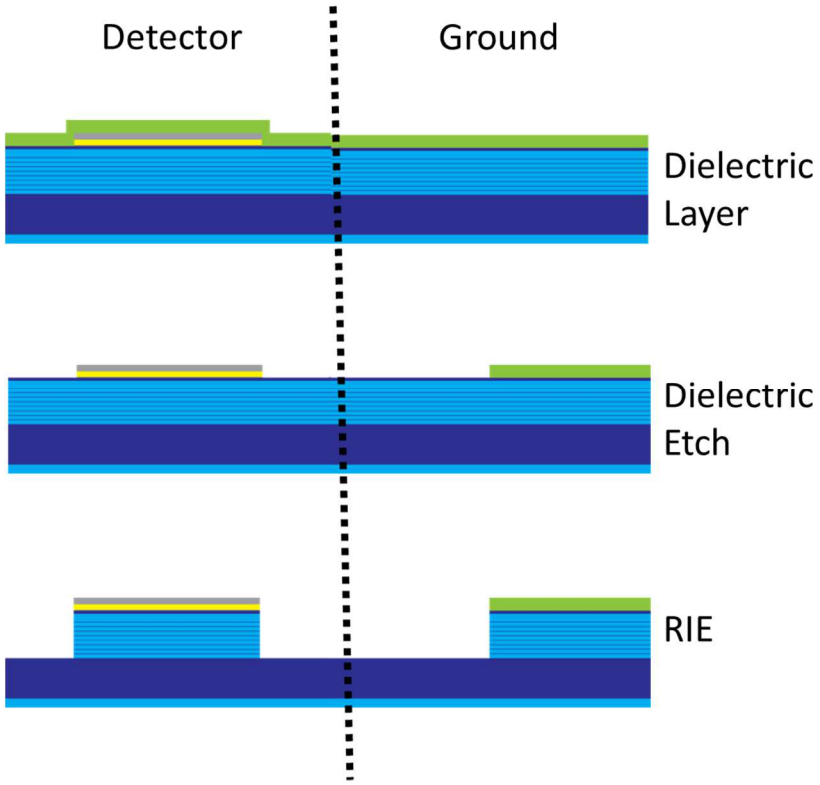

Figure 24 Initial Steps of Metal-Metal Bonding Process: Detector pillar and ground pillar formation. The ground side is in a way, sacrificial because the QWIP will be shorted

After the RIE, the ground MESA is patterned to leave exposed semiconducter for a few microns around the edge. The whole sample undergoes the HBr undercut etch described previously. The pillar should be exactly the same as before allowing for the self-aligned evaporation, but the ground MESA should have a gradual slope caused by the isotropic nature of the HBr etch as illustrated in Figure 25.

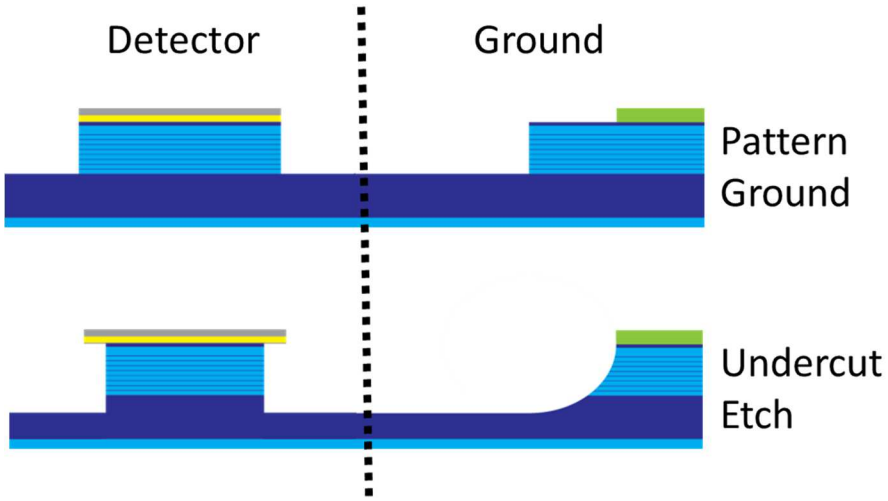

Figure 25 Undercut etch doubles to prepare for self-aligned evaporation and to create an incline for ground contact

The entire sample has gold evaporated on it. This, as before is self-aligned around the pillars defining the antenna and contacting ground. This ground-contacting metal will go over the slope of the ground MESA, shorting the QWIP that is there and providing metal on the same plane as it is for the top contact. This can now be bonded to a substrate with a fanout metal pattern as illustrated in Figure 26.

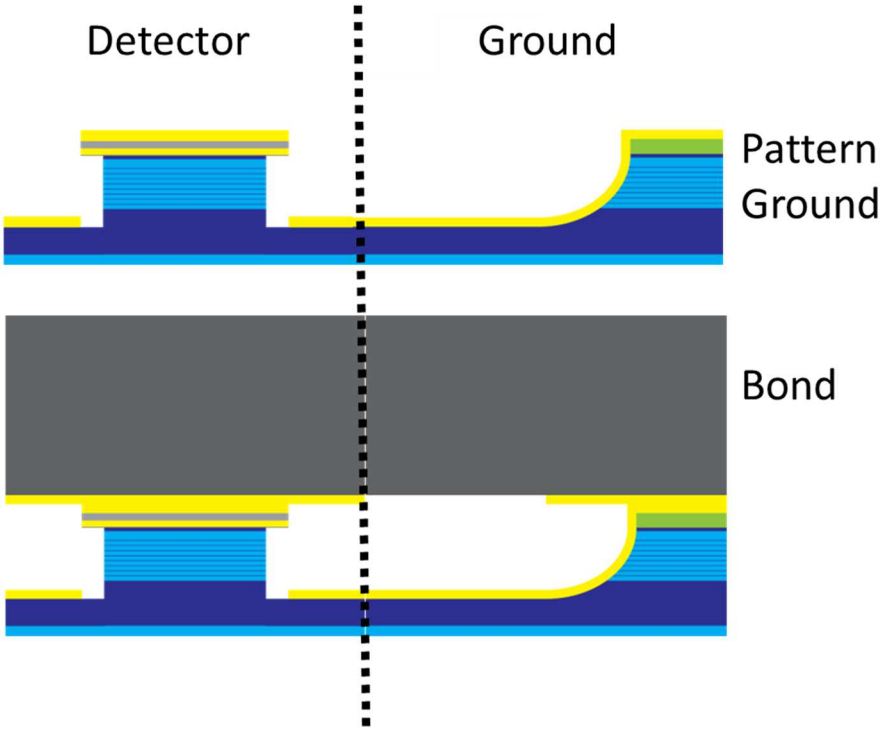

Figure 26 Metal deposition and bonding process

It's impossible to contact every device by a fanout circuit, so the design in Figure 27 is for 36 devices and 4 ground MESAs (40 total pins). The device chip should be 1cmx1cm and the fanout chip will be 2.5x2.5cm and sample devices varrying and size and distance to center.

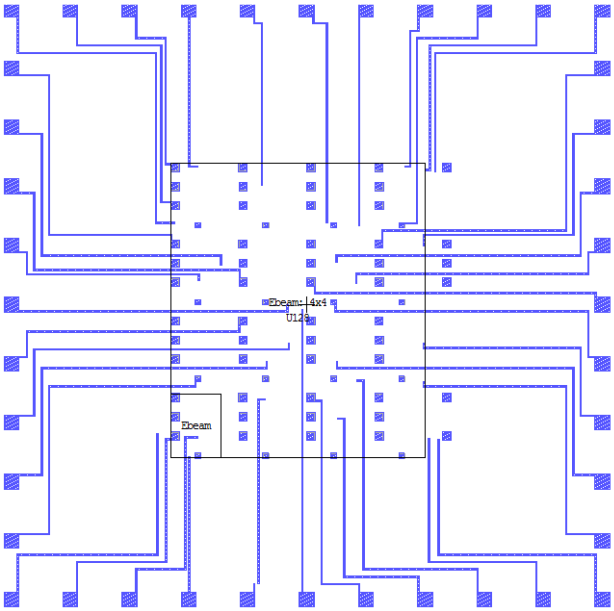

Figure 27 Fanout Mask Compatible with previous MESA Mask. The rectangle in the center is the expected area of the QWIP chip

The biggest unknown in this process for this group was the actual bonding process. Initially, these experiments just started with a square-array of 10μm gold circles on a silicon substrate. This gold was used as an etch mask and ~1μm pillars of silicon were made. This was to be bonded to just a solid sheet of gold on either silicon or a gold slide. This way, the bonding process itself could be completed without worrying about complicated processing or alignment. Initial tests focused on just cold stamping with 50kg of force. However, it was found that for this to work the surface must be activated to remove natural organics and moisture that are deposited in a natural room ambient. This can be taken care of with either a plasma clean or an elevated temperature. The process was now 1) RCA clean on pillar sample and Pirrahna Clean on Gold Sheet/glass, 2) O_2:Ar plasma, 3) Elevated Temperature bonding.

The initial attempts with any actual bonding had mixed results (Figure 28). In the first succesful attempt, there was only partial coverage and bad adhesion. The second succesful attempt, there was more force and complete coverage but poor adhesion as well as deformation due to too much force. The thid attempt had great adhesion as the chips couldn't be seperated, but the chips were uneven and the half of the pillars weren's bonded.

Of course any particulate on the front or back of the sample would ruin this process, but the cleaning steps should mostly take care of this. Instead, we concluded that there was significant deformation of both chips. The sample angle alignment is sometimes unclear and the crosses are "smeared" instead of just a solid clear cross as they are when doing bonder alignment. This is most likely due to chip deformation.

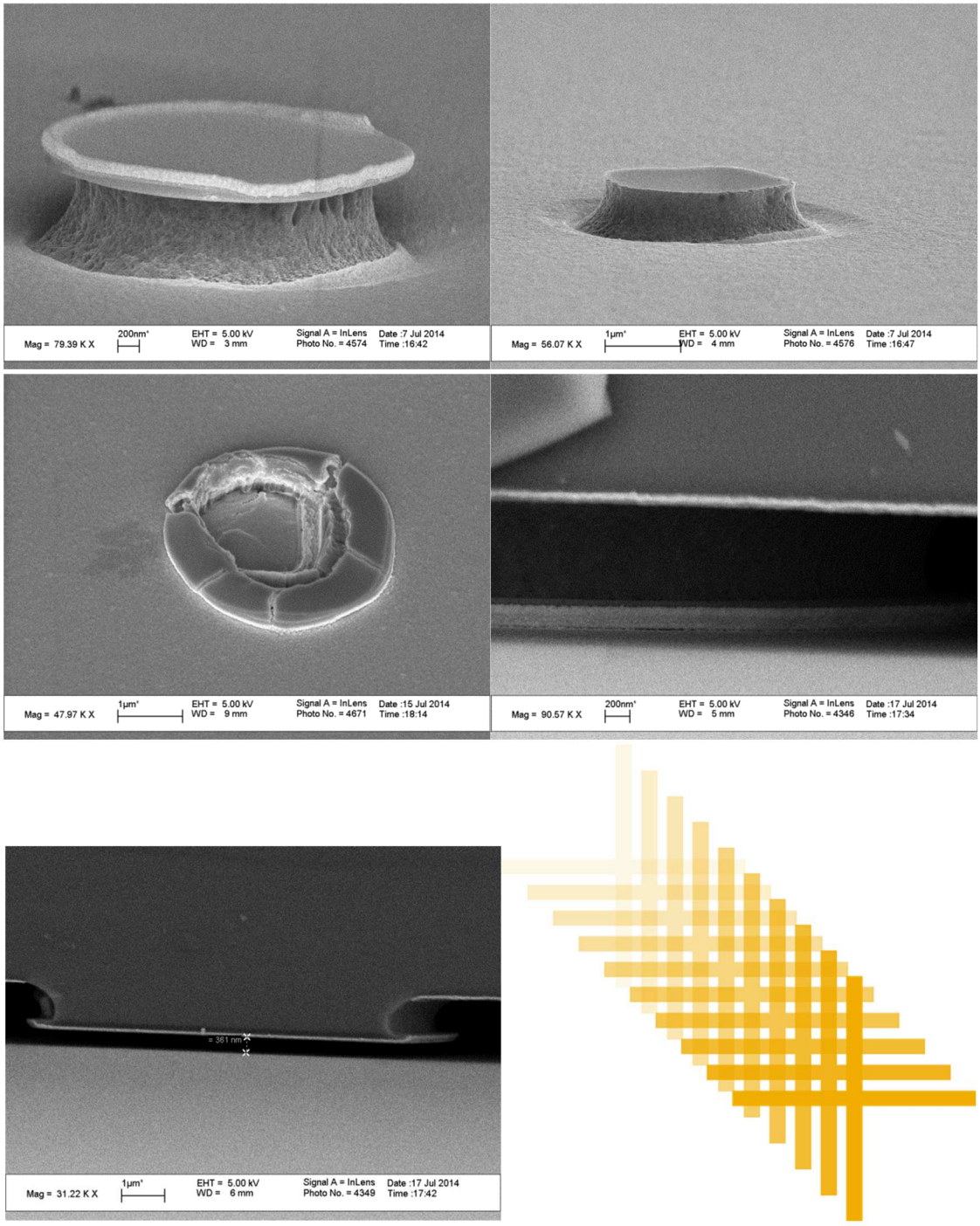

Figure 28a) Silicon Pillar with Metal Top b) Similar Pillar after gold-gold bonding with metal removed. c) Metal transferred to gold sheet with too much pressure applied. d) 10µm circle array completely fused from metal-metal bonding. e) Pillar from same sample as middle right on the other side of the chip showing separation and angular variation. f) Common trend in alignment mark on potentially bent samples

After this we attempted to use Polymethylsiloxane (PDMS) as a stamp. This is used in other cold welding experiments as the PDMS is very flexible and deformable and can absorb deformations, particles, and inconsistensies. Basically, a mold is made out of the QWIP MESA pattern on 10μm-thick SU-8 on silicon. Dissolved, dessicated PDMS is poured into this mold on a hot plate. The holder chip for the PDMS is placed over the mold and placed in a weight configuration that applies equal pressure to the mold (Figure 29). This is then cured on the hot plate at 110°C for 2 hours. This then has gold evaporated on it everywhere.

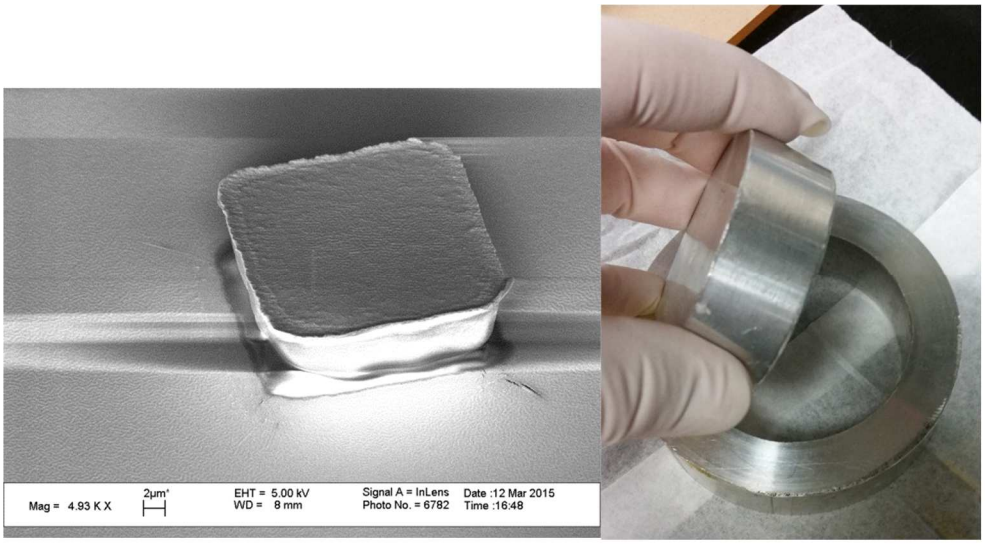

Figure 29a) PDMS Stamp with Metal b) Simple aligned flat weight for PDMS curing

This method had promissing initial results in bonding gold to gold. (Figure 30) There was partial adhesion and transfer. The coverage was only partial again, and the edge adhesion wasn't desireable. Also, due to the the deformation of PDMS, some surrounding gold was able to come in contact in some cases.

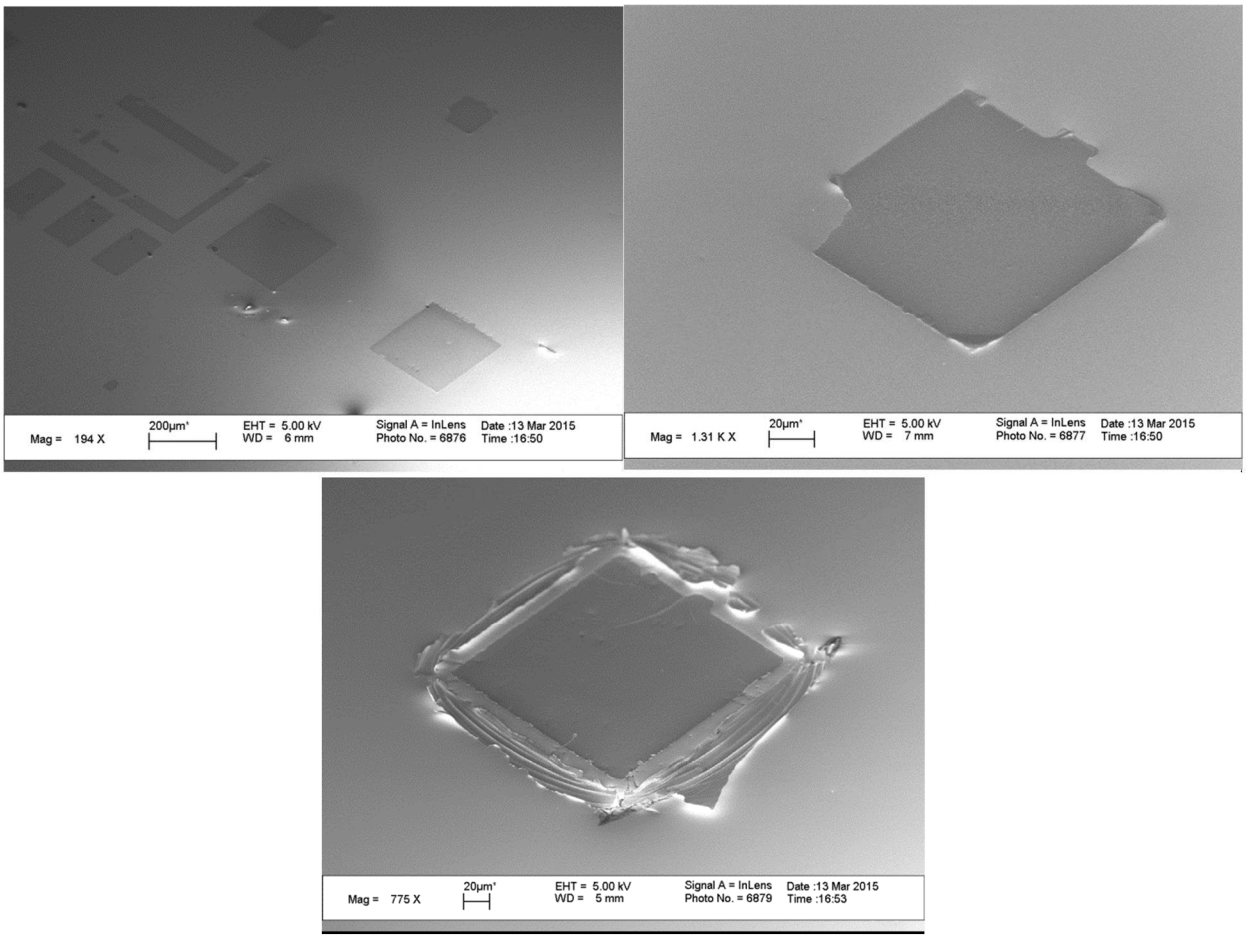

Figure 30 a) Sample Pattern Transferred by PDMS Stamp b) Single Square transferred with PDMS stamp. The transfer is rough around the edges. c) Similar Square on other sample where too much pressure was applied on one side. Due to the flexibility of PDMS the pillar was deformed enough to where the bottom surrounding transferred metal too.

V. Etched Grating QWIP

A. Design of Optical Gratings for Etched QWIP

An optical grating is a series of lines and spaces that can re-direct light to a new direction or multiple new direction. In free space this can be thought of in transmission or reflection, based on the idea that far field diffraction is proportional to the Fourier Transform of an Aperture. [40] Free space diffraction gratings are made up of a 1-dimensional square wave, which when transformed, becomes a series of delta functions, or in this case a series of diffracted orders in angular space. The multiple diffracted orders (m) can be found in terms of incident angle (θ_i), periodicity (d), and wavelength (λ) [41]:

$$\theta_m = \sin^{-1}\left(\frac{m\lambda}{d} - \sin\theta_i\right) \qquad (27)$$

More generally, we can think of this in terms of the wavenumbers of the diffracted orders ($\vec{k}_m$), incident wave ($\vec{k}_i$), and grating ($\vec{K}$):

$$\vec{k}_m = \vec{k}_i - m\vec{K} \qquad (28)$$

This generalization is important, because it extends the grating principle for coupling too/from waveguides and acting as reflectors for semiconductor lasers by altering the period to couple to a wavenumber supported by the waveguide.

Our design uses the similar principal, but instead of coupling to a waveguide, it is designed to couple to a resonant mode in etched QWIP (Figure 31). This uses lines and spaces of Gold over Etched QWIP on top of another layer of gold.

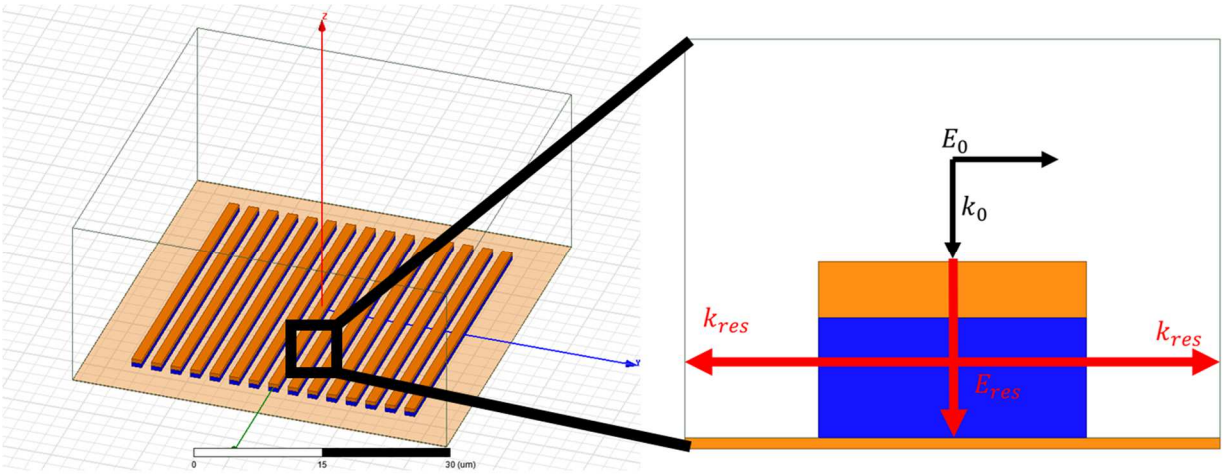

Figure 31 Layout of Etched Grating QWIP and direction/polarization of incident and coupled radiation

Because of the etched QWIP and metal in conjunction, this structure can't be solved analytically with the grating equation. To find resonance for this structure we use ANSYS HFSS. We input our QWIP material [42] and gold [47] relative permittivity and loss tangent/conductivity respectively.

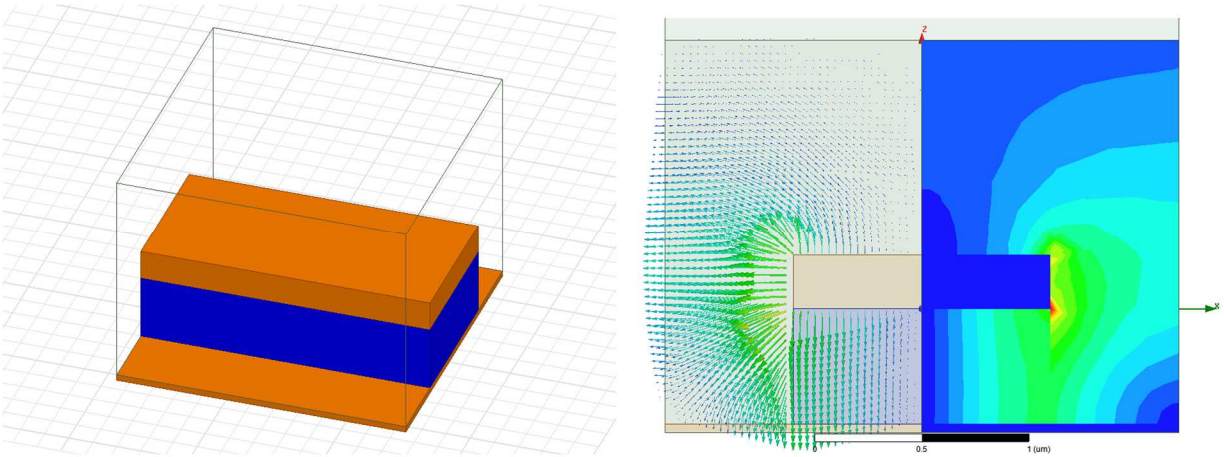

Figure 32 a) Single period of Etched Grating QWIP b) Field cross-section of grating QWIP, with the E-field vectors on the left and the magnitude on the right

The 3D simulation uses a floquet port source and Master/Slave boundary conditions that define a periodic structure like this (Figure 32). The source uses 1W, so the Quantum Efficiency can be calculated in reference to power [31] and is shown as a function of Period in Figure 33:

$$\eta = \frac{1}{P_0}\int \alpha I(\vec{r}) d^3r \qquad (29)$$

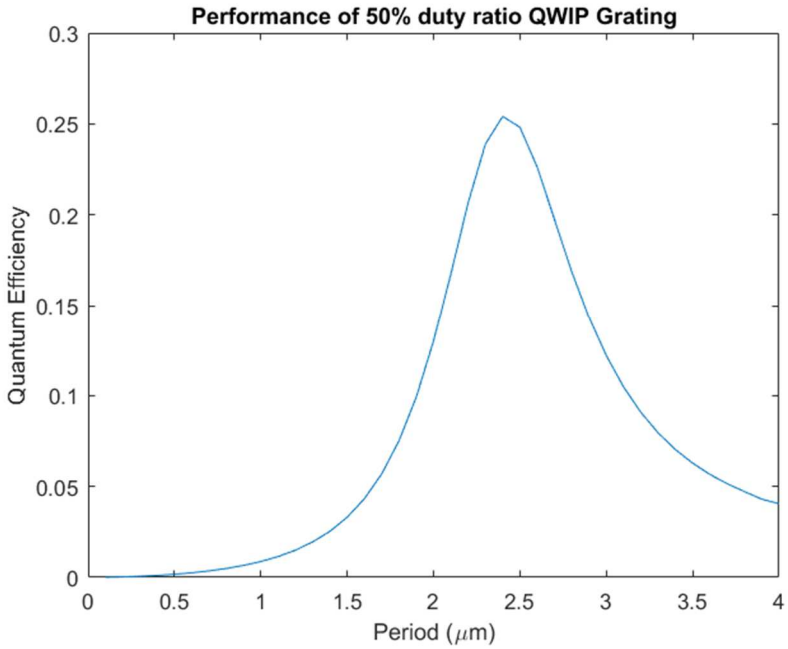

Figure 33 Quantum Efficiency of 50% duty ratio QWIP grating

B. Grating QWIP Fabrication

This process requires thin QWIP on a layer of gold, meaning we require a way to transfer QWIP onto a layer of gold on a mechanical substrate. We start with the exact QWIP structure as previously described.[i] A thin layer of titanium and gold (5nm/20nm) is deposited on both QWIP and a piece of silicon. These metal layers are activated with Argon plasma and immediately pressed together by hand. Finally, pressure and heat are applied in a flip-chip bonder; 35kg (~3.5MPa) at 200°C are applied for 30min. The indium phosphide substrate and 500nm bottom contact InGaAs are chemically removed and we are left with 585nm of QWIP and thin contact.

With the bonded substrate, we then deposit oxide. 250nm of SiO_2 is deposited by PECVD at 200°C. This is patterned with a laser writer and then etched to form a base for a contact pad (Figure 34).

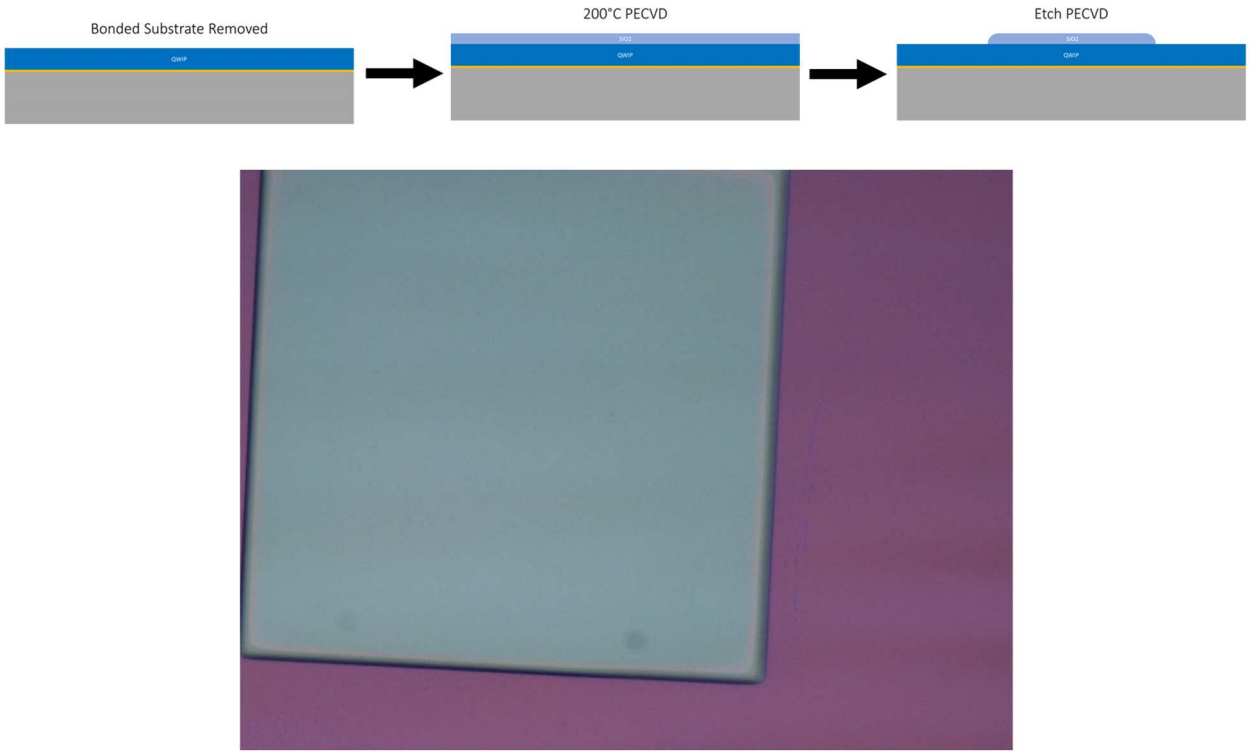

Figure 34 a) Oxide Pad definition process flow b) microscope image of reflowed oxide pad

The metal for the grating is then defined. We use e-beam lithography to define the grating for two reasons: 1) The pattern, 1.2µm lines and spaces, is slightly too small to be defined by our conventional lithography capabilities 2) We are patterning this in parallel with another QWIP design on the same bonded wafer that is outside the scope of this publication. A bi-layer of PMMA/MMA is exposed and developed followed by a brief O_2 plasma clean and a metal deposition of Ti/Au/Cr (5nm/240nm/10nm). The liftoff is shown in Figure 35. The gold provides the correct low-loss optical coupling for this device, and the Chromium acts as an etch mask.

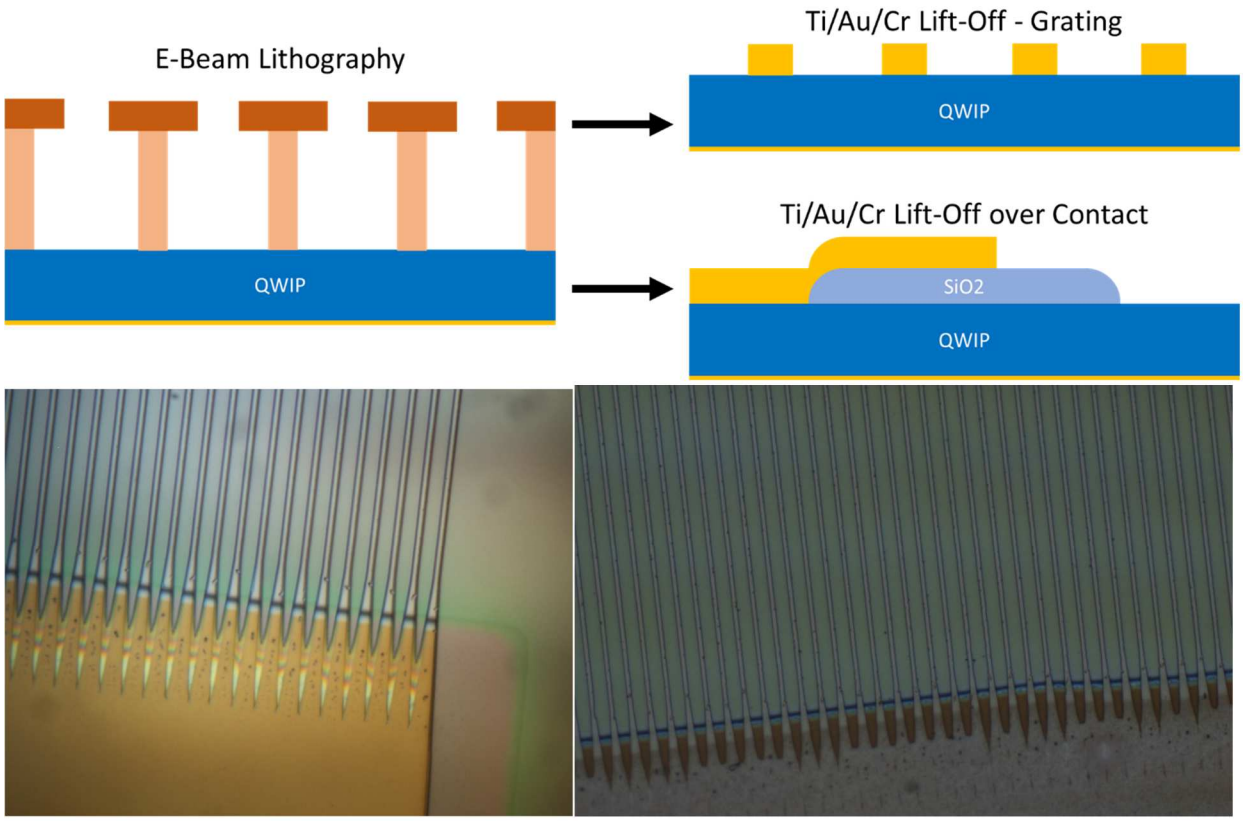

Figure 35 a) EBL to liftoff process b) EBL of pad and grating c) metal lift-off

The III-V is etched then etched using the metal and SiO2 as a mask. This leaves behind active QWIP grating stripes and an insulated platform for making contact. We use H_2:CH_4 etch chemistry which attacks both InP and InGaAs. The grating stripes etched are shown in Figure 36. There were unintended slots and separations at the base of each grating stripe, we think due to some unexposed resist. This shouldn't change the function however if they are electrically connected; the field is coupled perpendicularly to the stripes.

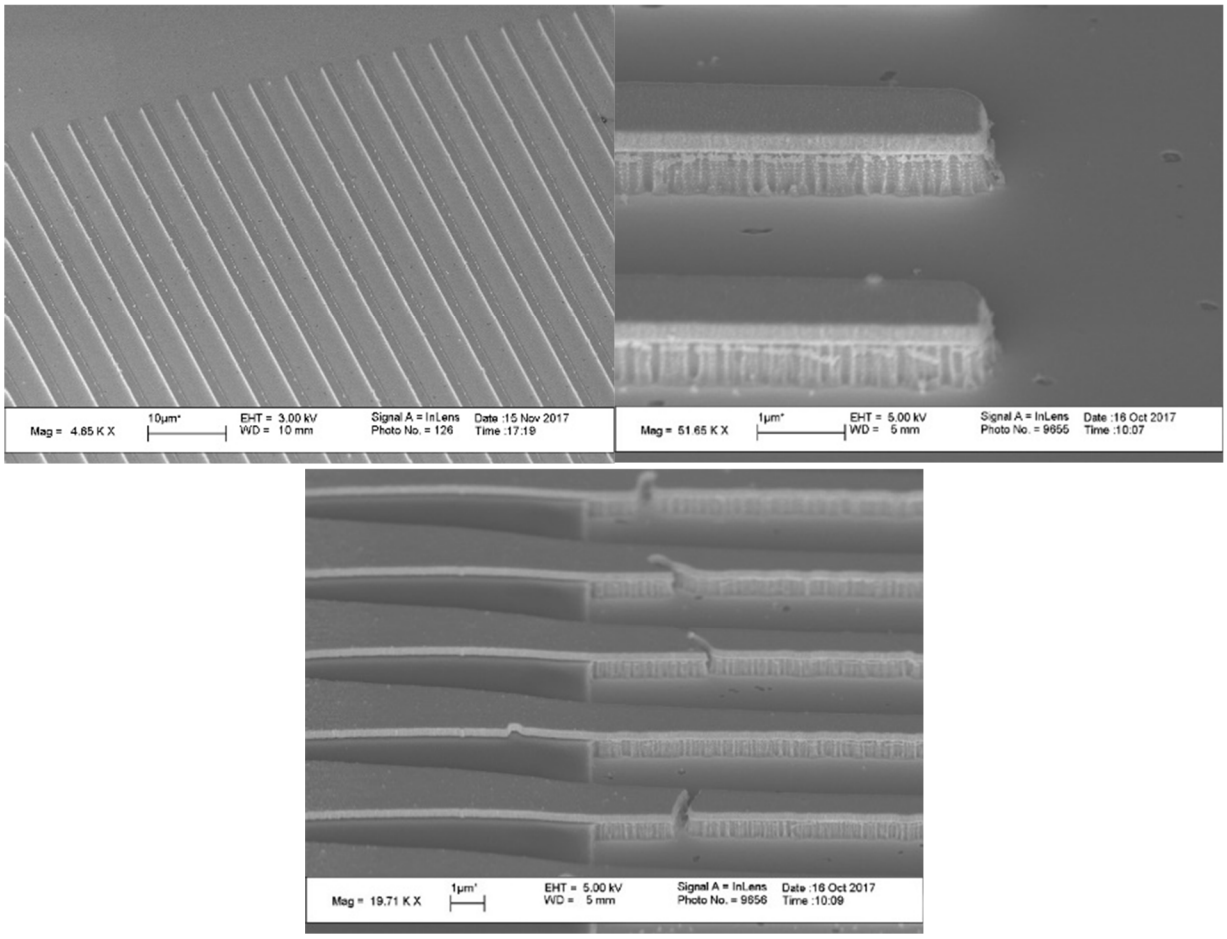

Figure 36 SEM images of QWIP etch gratings

Because the top layer of the metal we used is chromium, a gold ball bond can't be directly connected. Therefore, we must make a second metal pattern optimized for our gold ball bonding process. A 250x250µm square of Ti/Ni/Au is defined by electron beam lithography and lifted off on top of the silicon pedestal, overlapping with the Ti/Au/Cr from the grating (Figure 37). Titanium is used for adhesion, Nickel is used as a solid sturdy base for wirebonding, and gold is to provide a fresh, non-oxidized surface for wirebonding.

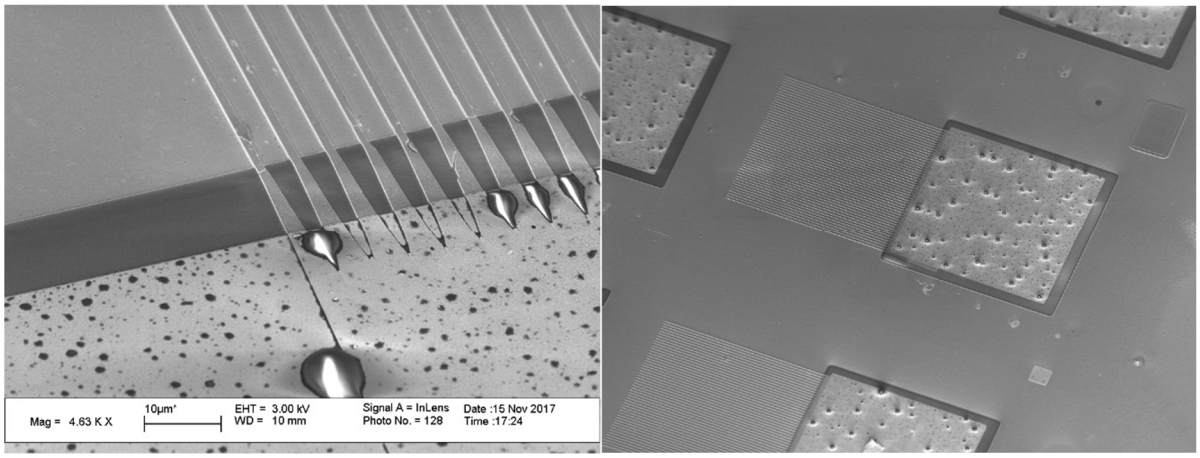

Figure 37 Contact Pad lift-off

There is some unidentified organic contamination on the contact pad, but the wirebonding was successful anyways. This device is completed and ready for measurement at this point. It is wirebonded and soldered to a cryostat that's ready for measurement.

C. Grating QWIP Device Measurement

For this measurement, an FTIR modified to bypass the internal detector, and kick the collimated beam out to our detector. The device is connected to a Low Noise Amplifier that applies a bias and offset current (equal to negative dark current). The signal input is amplified by 20nA/V, which provides significant amplification and bandwidth (2kHz) and this output signal is filtered with a 300Hz bandpass filter. This signal is then sent to an oscilloscope triggered by the mirror motion to retrieve an interferogram.

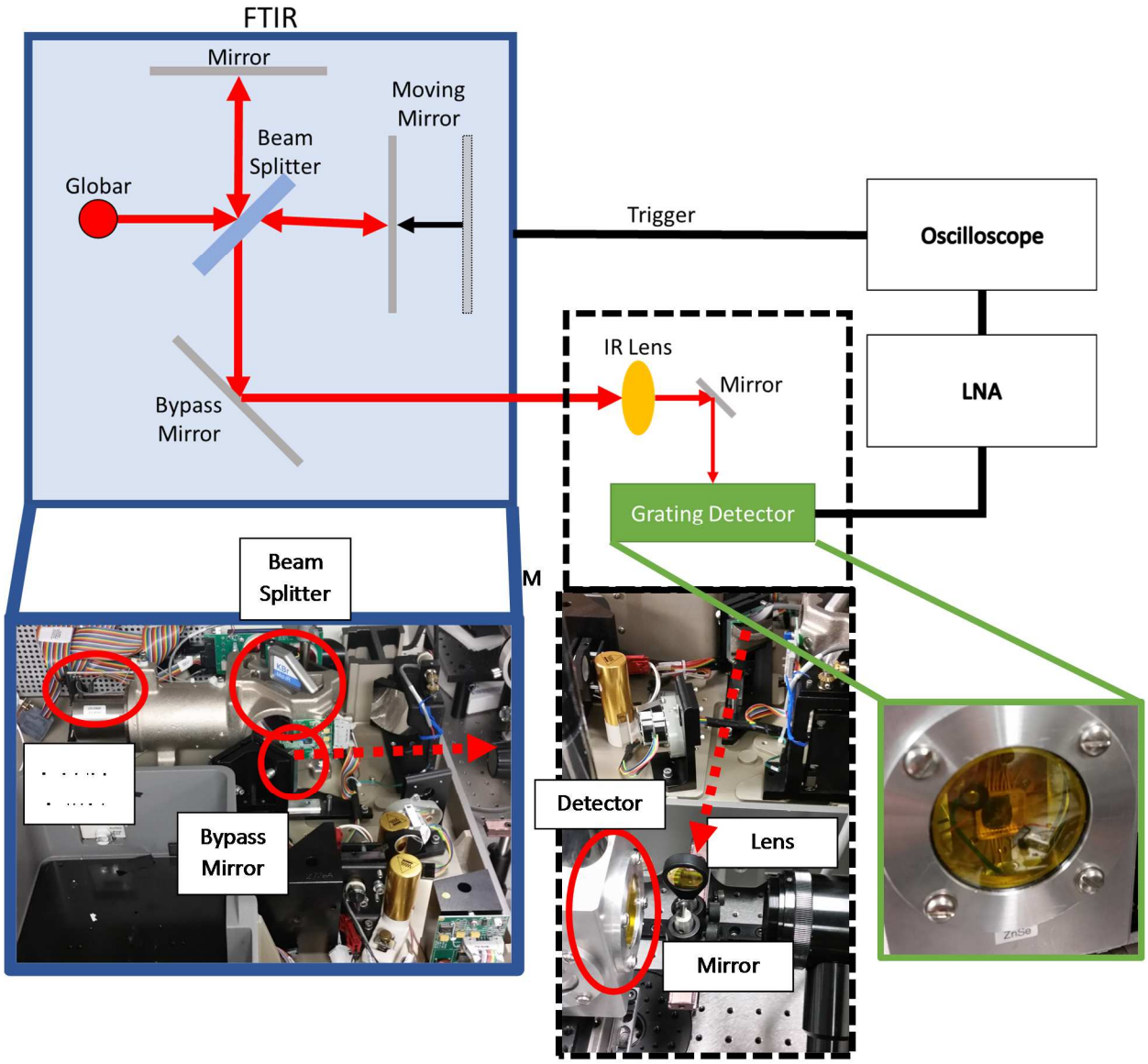

Figure 38 QWIP Grating Measurement Schematic

We obtain an interferogram from the oscilloscope in volts vs time then apodize with half a sinusoidal wave peaked at the center of the interferogram. (Figure 39)

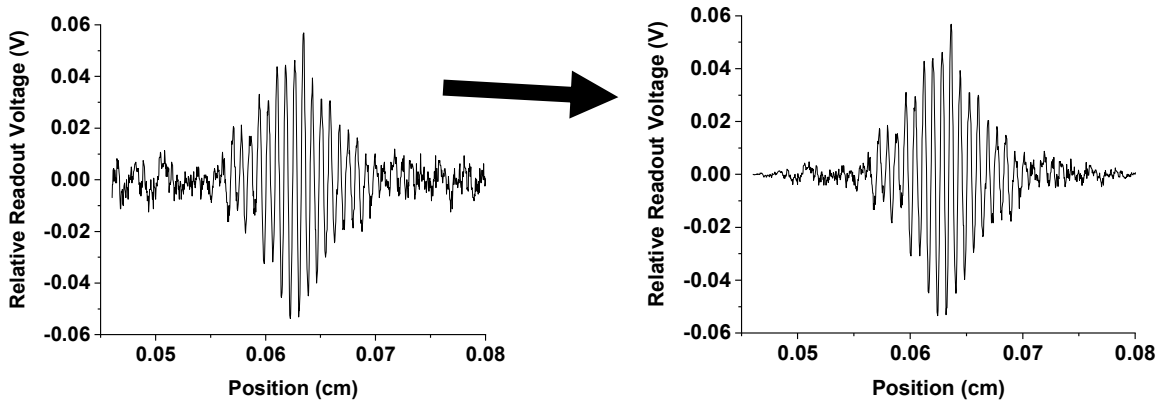

Figure 39 a) Device interferogram b) Apodized interferogram to remove fringe noise

Because we know the mirror velocity, this data can be processed to a plot of photocurrent vs. wavenumber by using a Fast Fourier Transform (Figure 40).

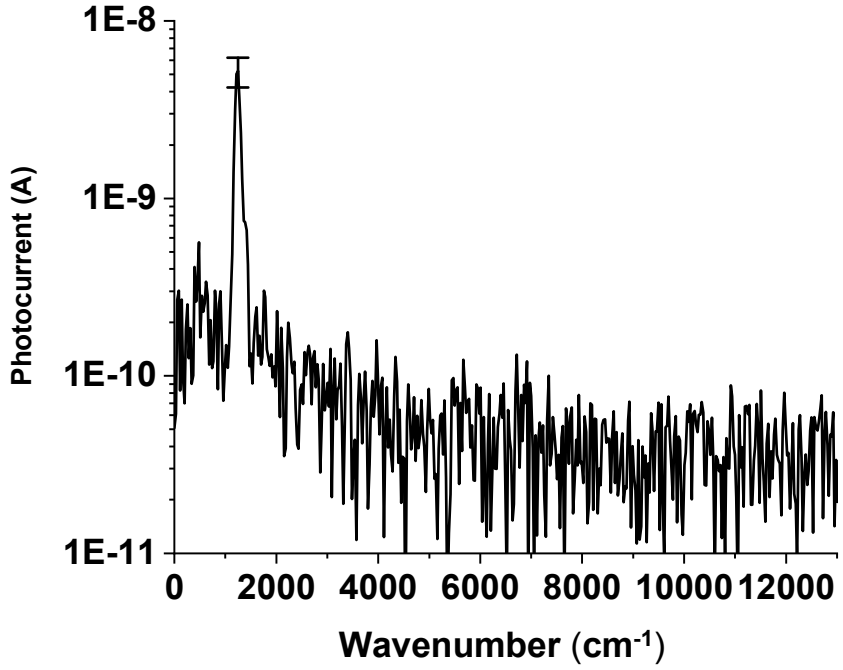

Figure 40 Fourier Transform of Photocurrent for Etched QWIP Grating

We repeat this measurement with a Mercury Cadmium Telluride (MCT) detector of a known responsivity (4A/V) and can determine the responsivity of our devices.

$$\mathcal{R} = \mathcal{R}_{MCT} \frac{A_{MCT}}{A_{Opt}} \frac{I_P}{I_{P\_MCT}} \qquad (30)$$

With a 1V bias, there is a peak responsivity of 0.12 A/V at 8.0μm. We know that with QWIP there is increased gain with increased bias. Up to the bias of 1V that we measured to, we can see increasing Responsivity with bias, we can expect a further increase in responsivity with increased bias. This design is supposed to be completely polarization-dependent; electric field perpendicular to the grating stripes will couple to the QWIP and just like a wire-grid polarizer, electric field in the direction of the wires will cause a current and reflect, causing now QWIP absorption. We also applied a polarizer to our setup at select polarizations from 0° to 180° by every 45°. These results are in Figure 41.

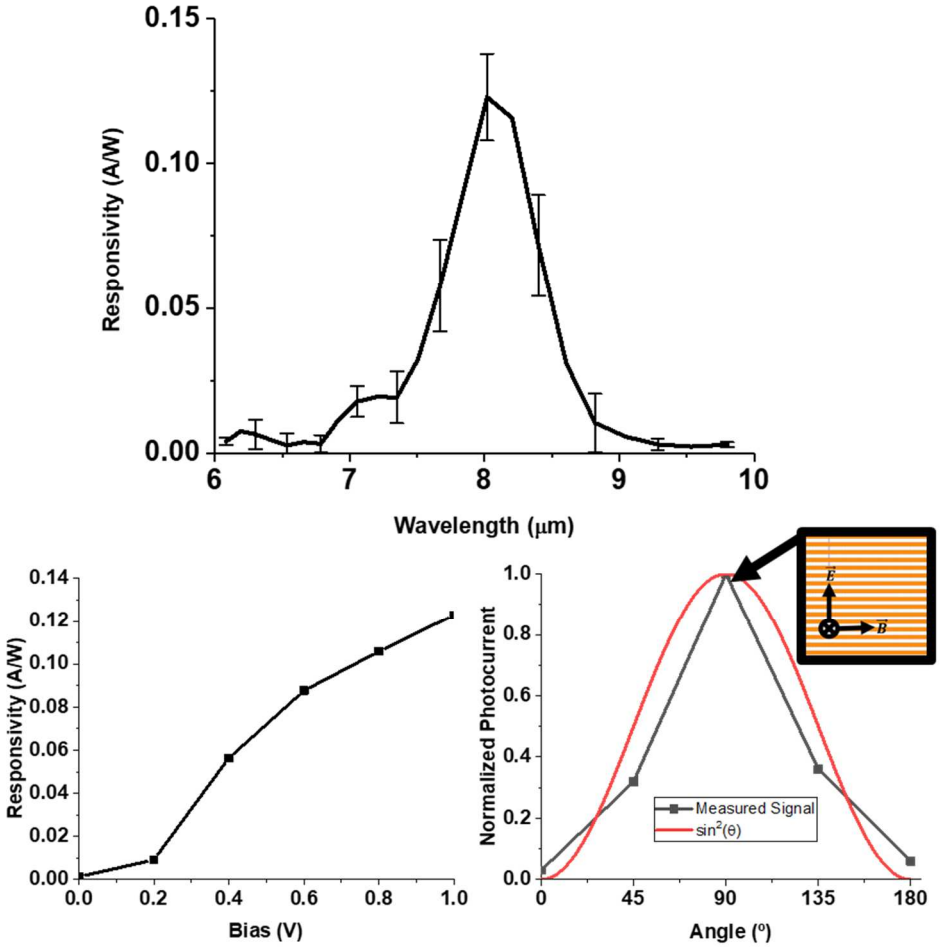

Figure 41 a) Responsivity of Etched QWIP Grating b) Effect of gain on responsivity c) Polarization response of QWIP Grating

VI. Antenna and Star-Coupler QWIP

A. Device Inspiration

There has been much progress in the field outside of this group since the successful plasmonic QWIP paper. A similar plasmonic array to the one described in Section IV was integrated with QDIP, and though this isn't the same absorbing material, the approach is noteworthy [47]. This group was able to successfully make a Focal Plane Array based on this technology, by doing substrate removal and backside bonding. However, the fabrication of this enhancement came at a cost: proximity. The plasmonic mode that this antenna supports had to be too far from the absorbing region to provide any real enhancement. Nonetheless, this detector was the first of its kind and the substrate removal process inspired our new designs.

The group responsible for the Quantum Efficiency formalism described in Section III has made some interesting resonant structures around QWIP [48]. The most recent of these structures was based on "square donuts" of diffractive elements directly on top of QWIP [49]. The size of the pixel and the dimensions of these elements were optimized for each material. This fabrication also featured substrate removal. The highest recorded quantum efficiency for this structure was >70%, a huge improvement. However, the drawback of this is that this structure requires a relatively thick active region, 1.15μm, and no area reduction. Compared to traditional QWIP this is an improvement, but to maintain such a quantum efficiency while shrinking electrical volume would be ideal.

A device that successfully tackled the volume problem also used substrate removal and backside metallization to make Metal-Insulator-Metal (MIM) cavities out of QWIP [50]. Basically, an array of patches was made on top of 371nm QWIP. This QWIP was then etched to significantly reduce the volume. This etching of excess current-generating material reduced the device's dark current by 3x at ideal conditions, pushing it into BLIP at 77K. This is a huge step forward in noise reduction for QWIP, however the resonant design was not optimized perfectly and, though it's not directly reported, we can extract a Quantum Efficiency of only 4% from other reported parameters.

B. Microstrip-coupled patches for BLIP Noise Reduction

In QWIP (and other photoconductors), if the dark current noise is reduced far enough, either by cooling or by volume reduction, then photocurrent from background radiation takes over as the dominant source of noise. As discussed previously, a narrow angle antenna-coupled

system could have amazing benefits for a detector in BLIP operation. Here we propose a structure based on a periodic patch antenna array coupled into a microstrip waveguides connecting every antenna in the x- and y-direction-s making a mesh of microstrip-coupled antennas.

In one sense, this structure operates like a phased-array antenna that can't be tuned; at its proper design, all of the antennas will add in phase for 0°-incident radiation at the correct wavelength, and add destructively at all of the other frequencies/angles in the desired measurement range. However, these antennas don't couple to another circuit, the substrate (as considered in the context of microstrip circuits) itself is biased and is the absorber.

This substrate is made of the semiconductor itself. The loss of 8μm InGaAs/InP QWIP with a 50nm barrier width is far too lossy to support the desired waveguide modes. However, if you apply just one quantum well, there is a perfect trade-off between supporting a resonant waveguide mode and absorbing all or most of normal-incident light. In the model this is represented as the thickness of one quantum well plus one barrier with the bulk absorption coefficient ($\alpha = 950\text{cm}^{-1}$) of the whole QWIP structure. As was the case with the small volume designs in this section, the device is clad with As_2Se_3 for the purpose of index matching (Figure 42).

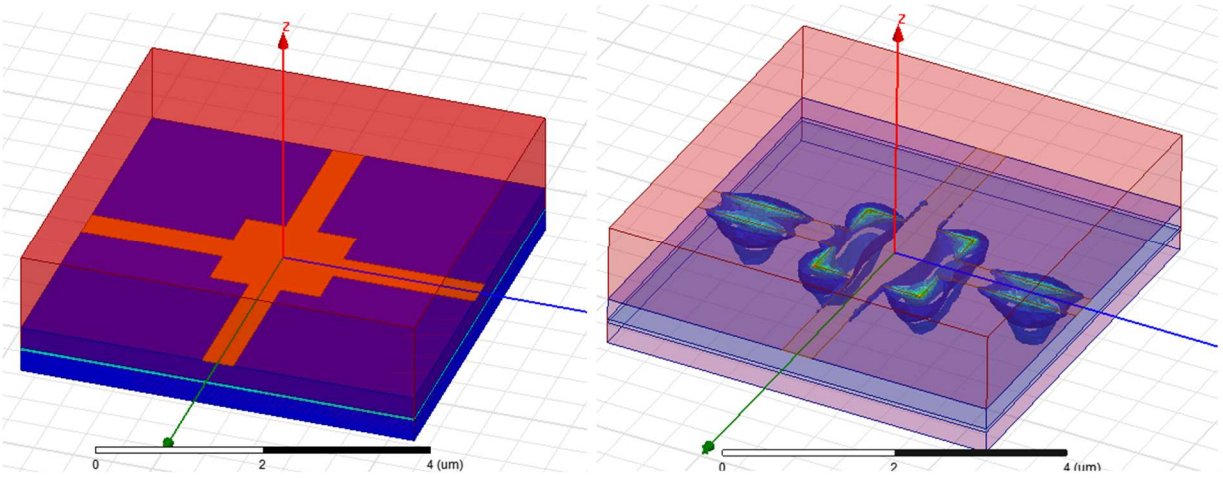

Figure 42 Concept of Microstrip-Coupled Patch Array for Narrow Angle Detection with Single Quantum Well

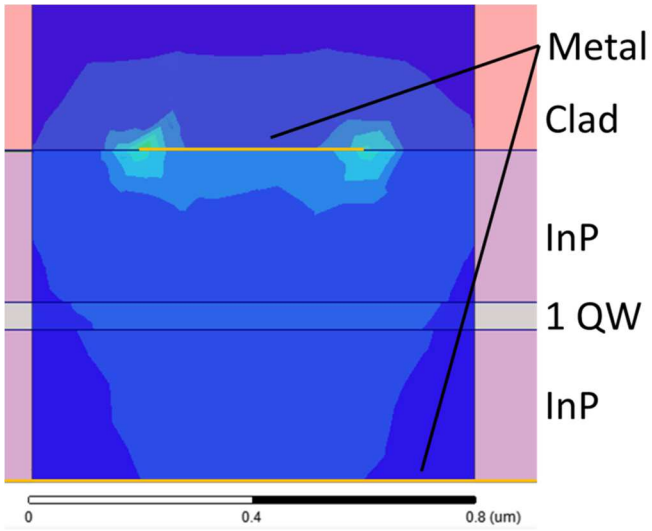

Figure 43 Microstrip Mode with Single Quantum Well

This type of semiconductor setup is realistic for BLIP as there will be only one quantum well contributing to dark current noise. Because this is designed for BLIP, removing semiconductor area is unnecessary, as it will unnecessarily cut into quantum efficiency and may introduce unwanted loss to the waveguide/antenna resonance.

C. Microstrip-coupled patches for Beam-Forming

In the last section we showed that a microstrip-based system can be made from semiconductor and can support a microstrip mode. To extend this system further we want to have an antenna system that can support beam-forming. This has two major applications: angle-of-arrival detection and lens-less imaging. If there is an array of pixels, each with a unique 2-dimensional angular response, not only could a cold shield be eliminated for background suppression, but the lens itself could be eliminated as the image could be reconstructed making this the first infrared application of synthetic aperture. We propose using a star coupler fed in with an array of antennas (Figure 44).

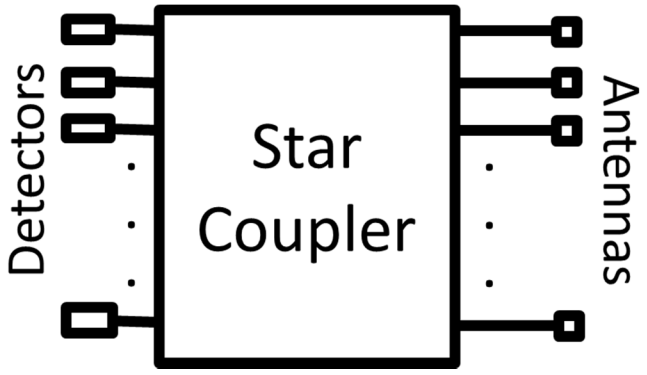

Figure 44 Star Coupler-coupled QWIP Schematic

Though we would like to eventually make a 2D-array with 3D-angle sensitivity that can "see" in any direction, our initial goal is to show only 1-dimensional beam forming with a 1-dimensional array of antennas and pixels. The idea is to couple broad-angle antennas into a multi-input, phase-difference-sensitive waveguide coupler that interferes based on relative input phase (determined by angle of arrival) and form a beam at the output, which couples directly to a detector. This coupler is called a star coupler, and the radius of curvature of the input and output is at the apex of the other side.

The microstrip structure is to be made from 0.5μm of Indium Phosphide over a gold ground plane. The microstrip and couplers are on top of this and made of 0.25μm of Gold on top. The QWIP is the same 8μm wavelength InP/InGaAs structure discussed throughout this document and is 0.25μm thick on top of the substrate, with gold on top. Acting like a microstrip. The layout and microstrip mode is shown in Figure 45.

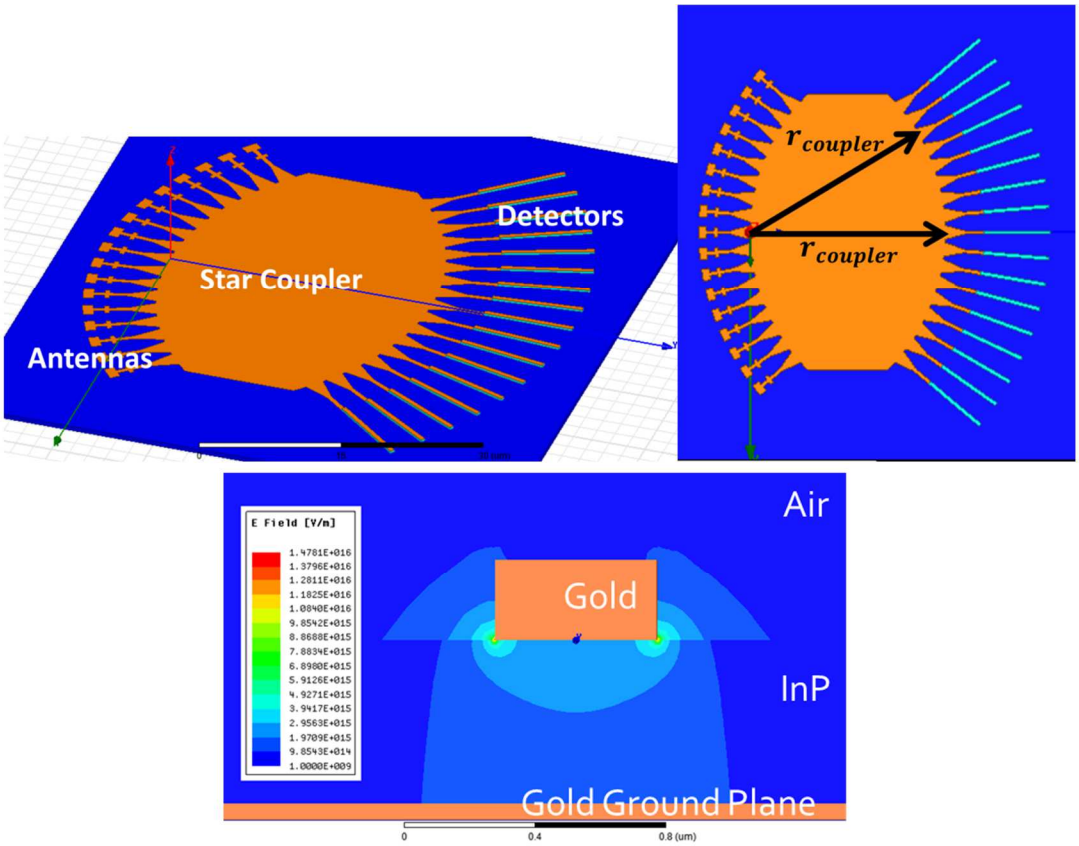

Figure 45 Patch Antenna-Star Coupler Concept and Microstrip Mode in InP

This design process utilizes ANSYS HFSS, a finite element Electromagnetic Solver. This is a common software used in designing microwave and radio systems and is ideal for this project due to parameterization; because the three types of components are connected by waveguides, and these modes can be excited directly with a specified complex impedance, the design of each component can be done separately. Waveguides are analyzed using real gold and the mode index is 2.72, corresponding to an effective wavelength of 2.94μm, the characteristic impedance is 45Ω.

The first component to analyze is the coupler itself. Because of the large structure we can't simulate the structure using real gold properties as the initial mesh would require too many elements (11 million) for the RAM of even an advanced system (uses more than 64GB) and this number would increase each subsequent pass. Instead, a 30μm wide waveguide is analyzed for each mode and a loss tangent of $\tan\delta = 0.01$ is estimated. The real coupler is simulated using Indium phosphide with this loss and PEC replacing the gold.

The radii of curvature are 10λ or 29.4μm and there are 17 inputs and 17 outputs separated by 5°. Each output has a 1λ long taper that increases transmission by 243%. Even though we can read the impedance of each port, matching a 17-port input and 17-port output passive device is incredibly difficult as each port interacts with all the others. We must rely on the tapers to minimize reflection as much as possible.

We expect Beam Steering to follow the formula [51]:

$$\theta_{star} = \sin^{-1}\left(\frac{\Delta\varphi - m2\pi}{k_{eff} d_{in}}\right) \qquad (31)$$

where θ_{star} is the beam angle relative to the center input in the coupler, $\Delta\varphi$ is the phase difference between inputs, k_{eff} is the effective propagation constant in the coupler ($n_{eff}\frac{2\pi}{\lambda_0}$, where $n_{eff} = 2.72$ and $\lambda_0 = 8\mu m$), and the distance between inputs is d_{in}, 2.6μm. The order, m, shows that this structure is similar to a free space diffractive grating. Of course, for a beam steering application, we only want to consider the 0th order, so this term drops out.

The phase difference is simply based on the distance of the antennas in the final design and the input wavelength:

$$\sin\theta_{in} = \frac{\left(\frac{\Delta\varphi}{2\pi}\right)\lambda_0}{d_{ant}} \qquad (32)$$

This angular response is shown in Figure 46 for both a 0° and 35° incoming phase front. Because the antennas aren't linearly spaced, however, this distance isn't consistent, and as such the input angle required to excite a specific detector will differ from that predicted by this equation at higher required angles. These equations are useful for initial design and understanding the device, but more rigorous simulations are required.

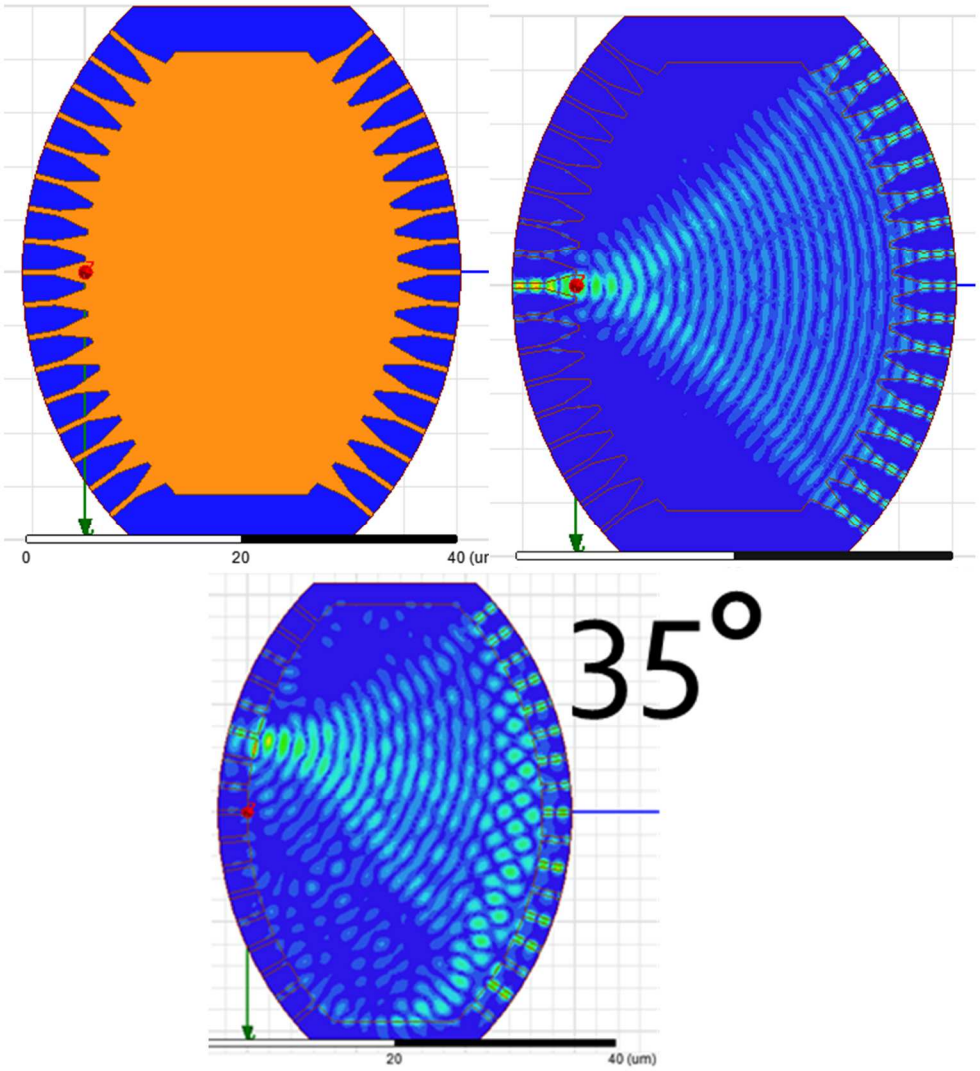

Figure 46 Star Coupler Decoding radiation from 0° and 35°

This structure is initially just analyzed for 0° incident radiation. Each port has about 10% reflection which would correspond to ~80% transmission, and more than half of the light is lost because of metal loss (our estimated loss tangent). The total transmission of power is 32.4%.

Next, we must simulate the detector. The detector is designed as an extension of a microstrip; an InP microstrip connects directly to a .25μm high InP ridge on top of the InP acting as a second waveguide that absorbs (Figure 47). There are four mechanisms for loss in this structure: metal loss, reflection, radiation, and QWIP absorption. The goal is to maximize QWIP absorption, while minimizing the other three losses and keeping the QWIP as small as possible to limit Dark Current Noise.

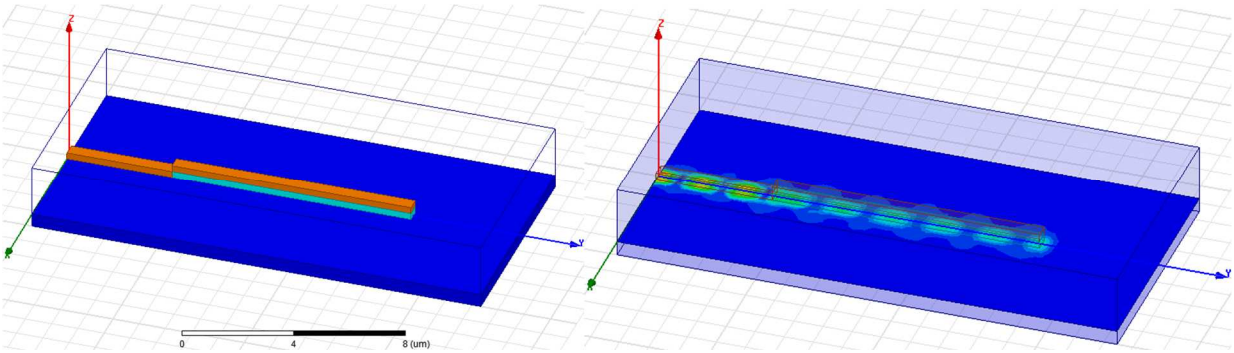

Figure 47 InP-Microstrip Coupled QWIP

In designing this, the length of QWIP is swept, and the QE (Figure 48), relative D*, and S_{11} (Figure 49) are monitored. There is a strong Fabry-Pérot effect as the length increases, and a QE maximum is chosen.

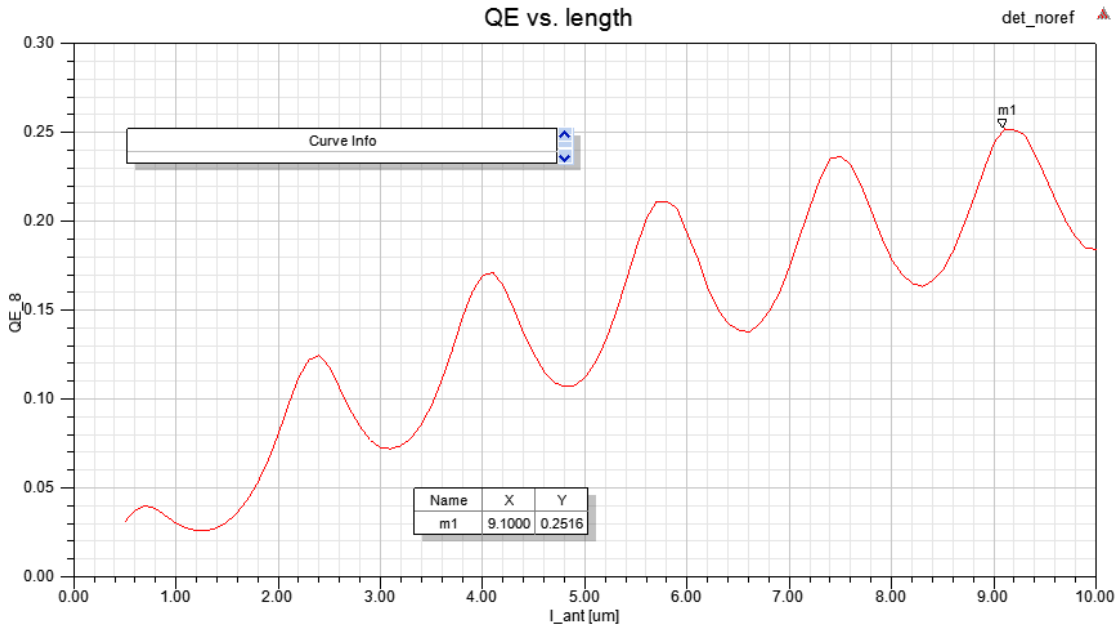

Figure 48 Quantum Efficiency of InP Microstrip-Coupled QWIP

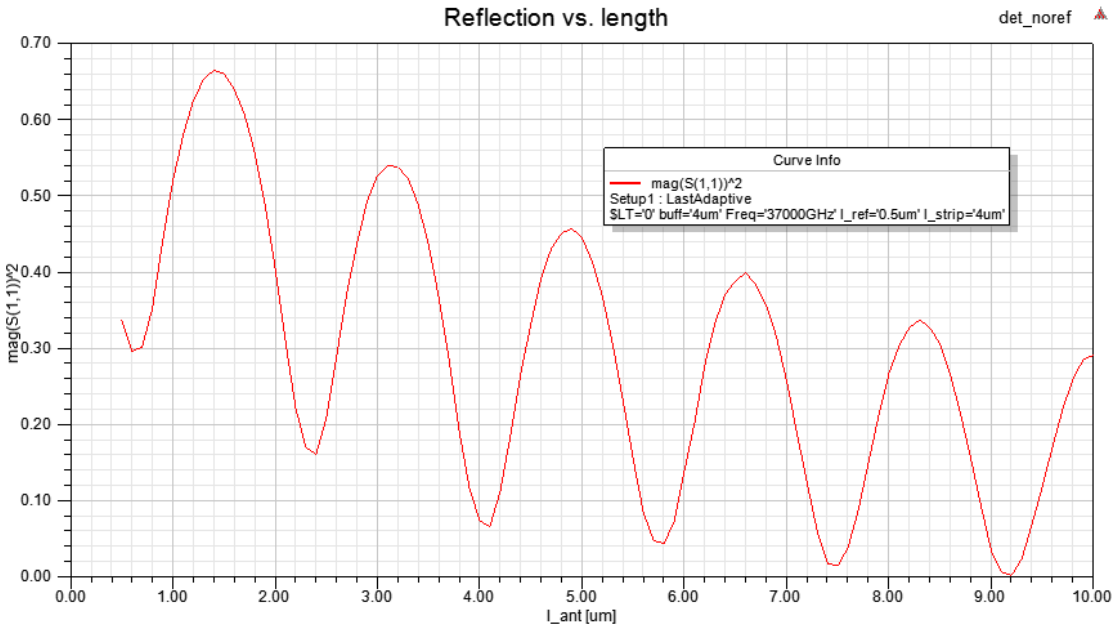

Figure 49 Reflection of InP Microstrip-Coupled QWIP

There is a local QE maximum at 9.2μm which also corresponds with an S_{11} minimum. Actually, $S_{11} = 0$ at this length which is very convenient as no matching is required. Otherwise, the Quantum Efficiency from the input waveguide is 25%. 22% of the power is radiated as this detector acts as an inefficient patch antenna, and 52% of the power is lost in the metal.

The last individual component to design is the antenna. A patch-coupled microstrip is designed with real gold for a maximum at 0° directivity as shown in Figure 50.

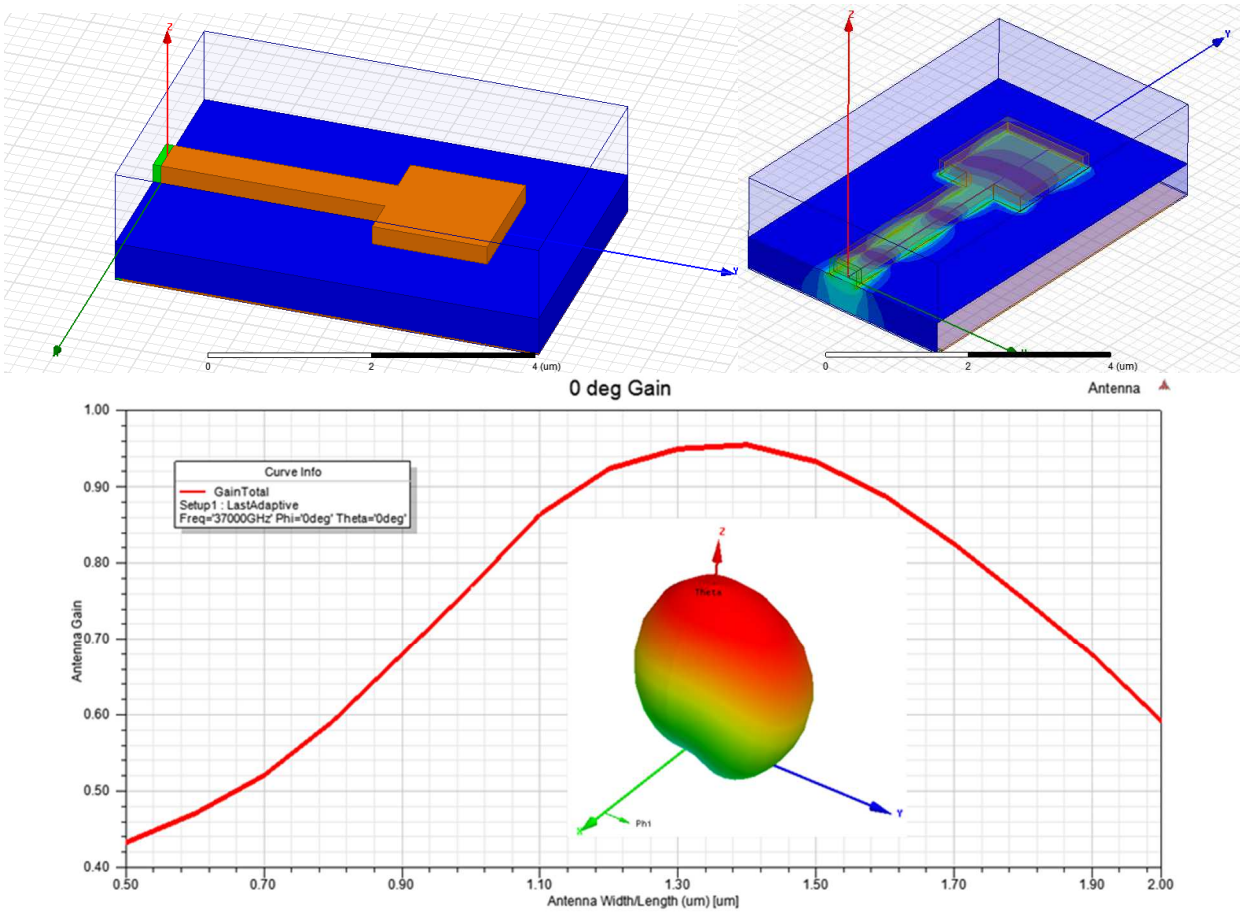

Figure 50 Square Microstrip Patch Antenna on InP and Radiation

The input of the waveguide is coupled with a microstrip mode as a passive antenna is reciprocal. The directivity and gain relate to power and efficiency as such:

$$G(\theta, \varphi) = E_{ant} D(\theta, \varphi) \qquad (33)$$

$$D(\theta, \varphi) = \frac{U(\theta, \varphi)}{P_{TOT}/4\pi} \qquad (34)$$

The normal-incidence gain is optimized and then impedance matching is applied to get rid of reflections at the input. After matching, the antenna efficiency is measured to be 76.8% and the normal incidence gain $G(\theta = 0°, \varphi = 0°) = 1.91$.

Now that all components are designed we must verify the system and the beam-forming. It is important to note that a second patch antenna is designed since we're not using real metal in the

large simulation. This antenna is not the same as the gold one, but has a similar directivity distribution, so it's a fair estimation, however exact numbers can't be determined analytically.

What's interesting is that this antenna has a large parallel-incidence-coupled lobe. This is likely due to the relative thickness of the substrate to the wavelength compared to that of microwave applications. Even without suppressing this, the three polarizations are orthogonal, and directivities are additive, so we can consider just the x- and y- polarizations. The comparison of total radiation and polarized radiation is shown in Figure 51.

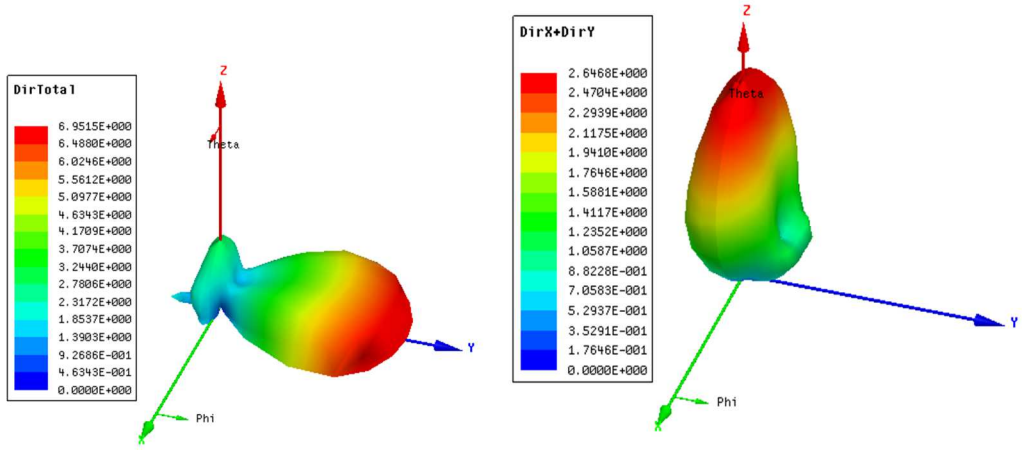

Figure 51 Polarization Sensitivity of Single Patch Antenna

This antenna is inserted at the end of the star coupler. Conveniently, because the detectors are naturally matched, a mode can be fed from each detector port. The idea is that each detector can "see" in a different direction, as the system is asymmetric from their individual locations.

As is the case with the individual antenna, there is a large z-polarized parallel-incidence beam, that we must get rid of. However, this can be controlled by the length of the microstrip between the coupler and the antenna system (including the matching stub) as shown in Figure 52, this length doesn't affect the matching of the individual patch.

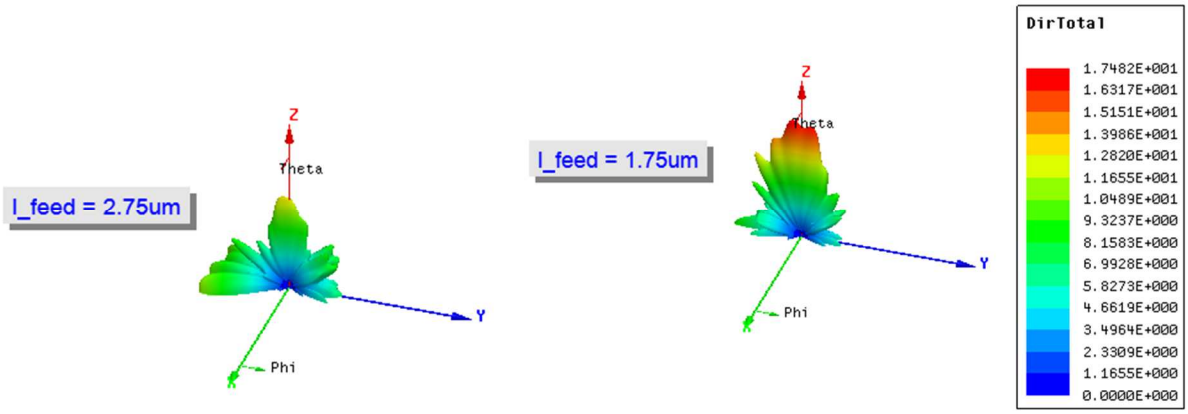

Figure 52 Effect of Feed Length on Star Coupler Radiation

Once this length is adjusted, beam forming can be analyzed. The field distributions from each port from the center to the end are shown in Figure 53-Figure 57. Ports are numbered 1-17, and 9 is the center.

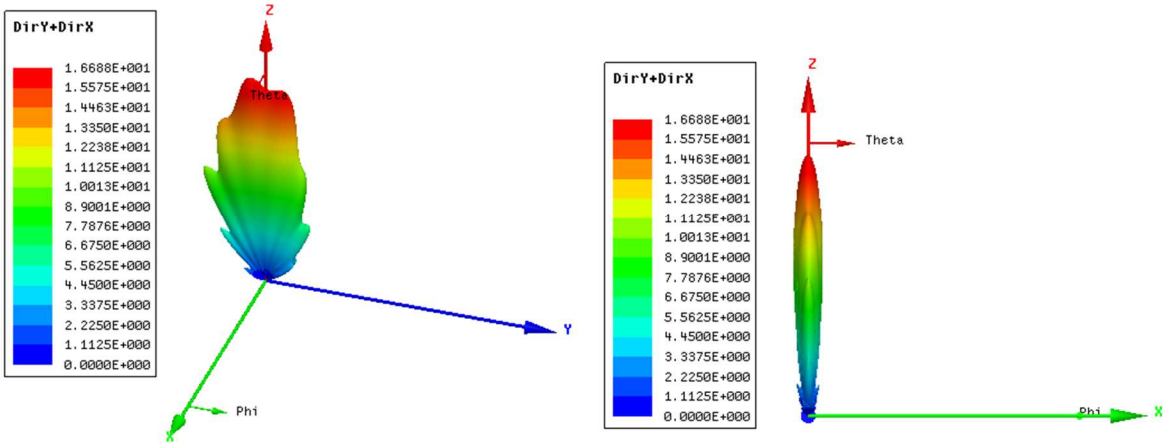

Figure 53 Port 9 Directivity of Star Coupler

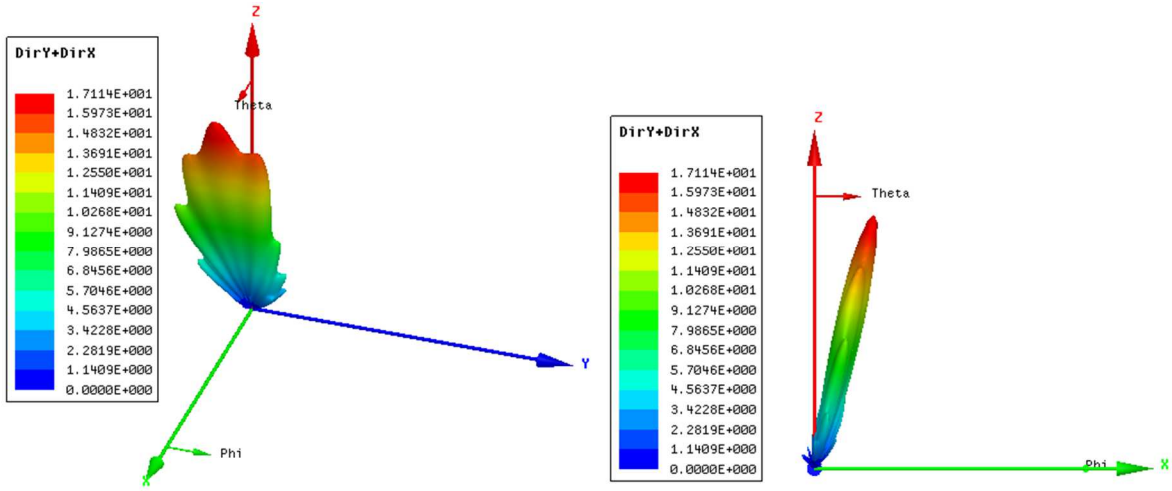

Figure 54 Port 10 Directivity of Star Coupler

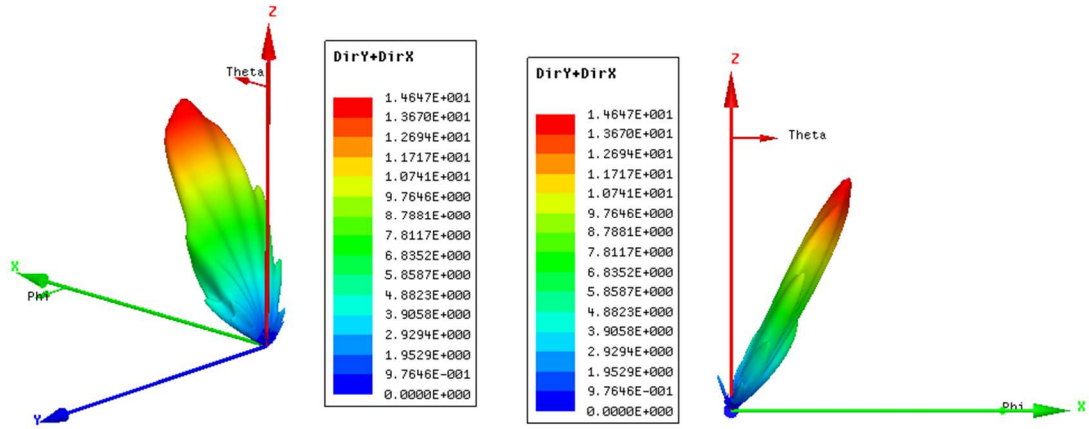

Figure 55 Port 11 Directivity of Star Coupler

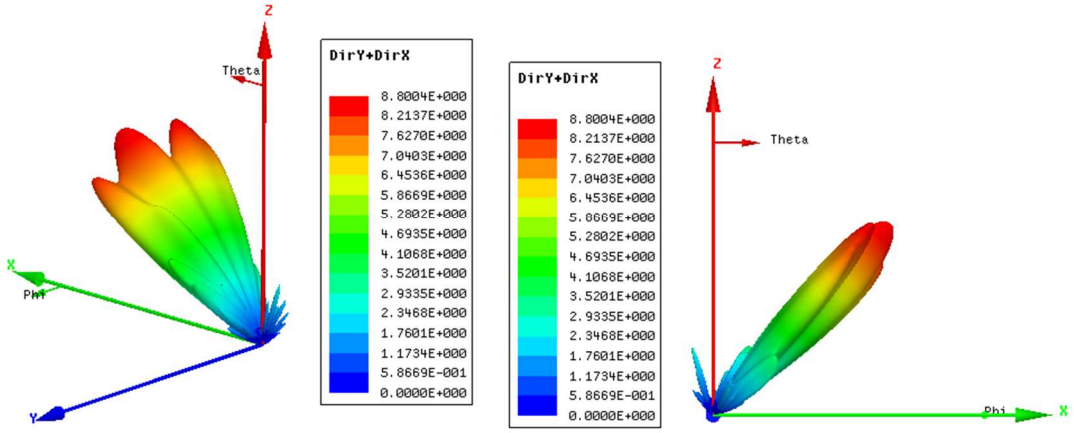

Figure 56 Port 12 Directivity of Star Coupler

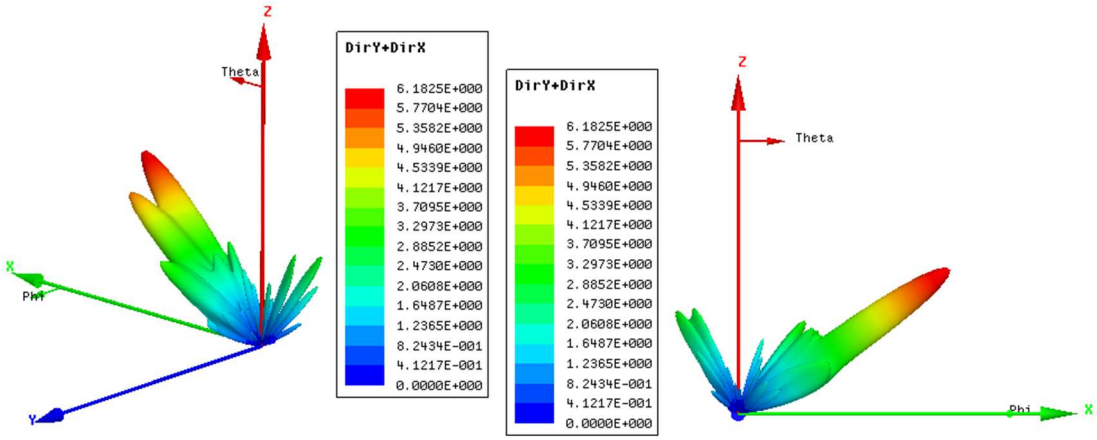

Figure 57 Port 13 Directivity of Star Coupler

These are the main 0th order beams. And the tuning is about 13-15° more for each port. This breaks down as higher orders become present. Ports 4 and 14 are a mixture (and not useful individually), and in ports 1-3 and 15-17 ±1st orders can be seen but again it's hard to really characterize as there's a lot of noise. Ports 1 and 17 are where the order becomes visible. This, however isn't predicted by the formula given above. These higher-order ports are shown in Figure 58-Figure 61.

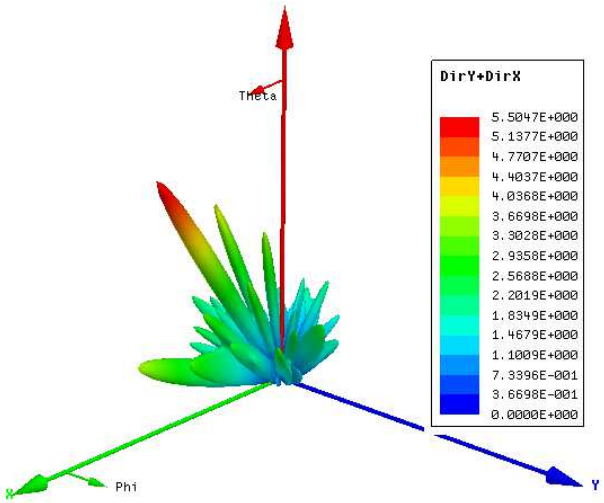

Figure 58 Port 14 Directivity of Star Coupler

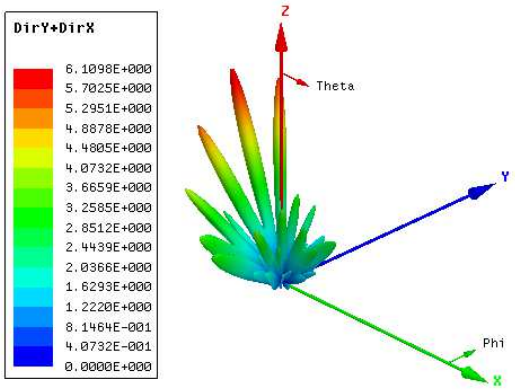

Figure 59 Port 15 Directivity of Star Coupler

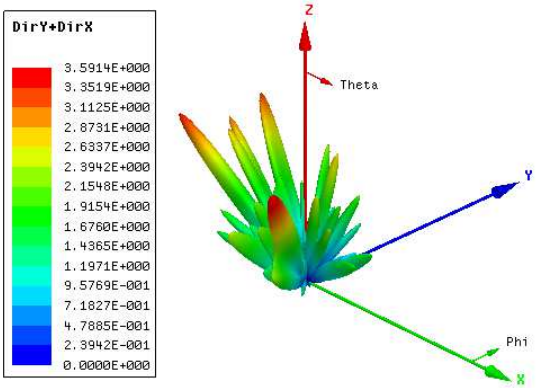

Figure 60 Port 16 Directivity of Star Coupler

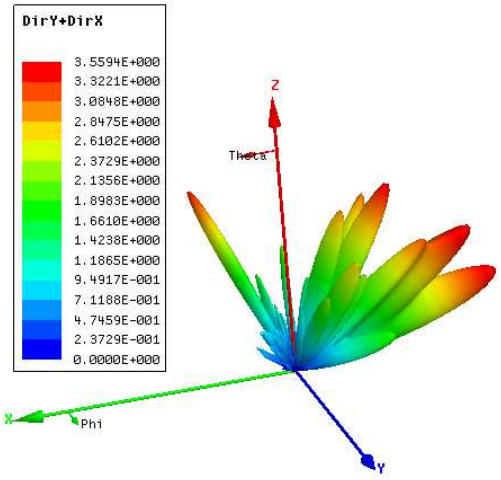

Figure 61 Port 17 Directivity of Star Coupler

Each above radiation pattern is generated by a 1W input at the detector. The total QE takes into account the XY-output power and the quantum efficiency of the detector at the point of microstrip input:

$$\eta_{TOT} = \eta_{DET} \frac{P_{XY}}{P_{in}} \qquad (35)$$

These are listed in Table 5-1, but the detectors of note, 6-12, have quantum efficiencies ranging from 2.5%-3.2%.

The specific detectivity of a detector, D^*, is directly dependent on measurement conditions. To determine a realistic D^* we compare to published results of a bulk QWIP with this same material system and assume the same measurement conditions [42], "*0*" denotes the published QWIP

$$D^* = {D^*}_0 \frac{\eta}{\eta_0} \sqrt{\frac{A_{opt}}{A_{elec}} \frac{t_0}{t}} \qquad (36)$$

All above parameters are known except for the optical area. For this we use the effective aperture of the antenna system as determined by peak gain and wavelength:

$$A_{opt} = \lambda^2 \frac{G}{4\pi} \qquad (37)$$

Table 2 - Power output from each detector

Port #	Port Angle	Total Power Output	Theta Predict	Theta Max	Phi Max	XY Power	QE	D* (cm$\sqrt{\text{Hz}}$/W)
9	0°	0.147W	0°	**0°**	N/A	**0.127W**	**3.2%**	$\mathbf{8.76 \times 10^{10}}$
8,10	5°	0.153W	11°	**14°**	**-19°**	**0.118W**	**3.0%**	$\mathbf{8.55 \times 10^{10}}$
7,11	10°	0.163W	23°	**31°**	**12°**	**0.110W**	**2.8%**	$\mathbf{7.57 \times 10^{10}}$
6,12	15°	0.169W	35°	**52°**	**22°**	**0.101W**	**2.5%**	$\mathbf{5.24 \times 10^{10}}$
5,13	20°	0.132W	49°	**57°**	**14°**	**0.0711W**	**1.8%**	$\mathbf{2.75 \times 10^{10}}$
4,14	25°	0.0667W	69°	33°	-6°	**0.0405W**	**1.0%**	$\mathbf{1.09 \times 10^{10}}$
3,15	30°	0.0526W	N/A	-17°	-3°	**0.0355W**	**0.89%**	$\mathbf{8.85 \times 10^{9}}$
2,16	35°	0.0648W	N/A	41°	-58°	**0.0401W**	**1.0%**	$\mathbf{9.97 \times 10^{9}}$
1,17	40°	0.1135W	N/A	**-71°**	**2°**	**0.0657W**	**1.6%**	$\mathbf{1.82 \times 10^{10}}$

It's fair to say that because each individual antenna is centered at 0° and has a similar beam shape to its real metal counterpart, that the XY power relative to each other is accurate, as well as the input angles "seen" by each detector. However, the magnitude of power is hard to know analytically.

D. Angle-Sensitive FPA Layout

This Star Coupler design is not an FPA or a camera, but is a proof of concept for beam-forming using antenna-coupled QWIP systems. However, the goal is to design future devices that could be conceivably used as an FPA. As such, we want to demonstrate how this microwave-to-infrared system could be extended physically to a FPA.

An FPA needs to be bump bonded to a side with signal to another chip with CMOS read-out circuitry. Because these microstrip detectors are relatively small and close together, the ground plane of this system will serve as the signal. A bump is bonded to an electroplated gold ground plane under a single pixel as shown in Figure 61Figure 62.

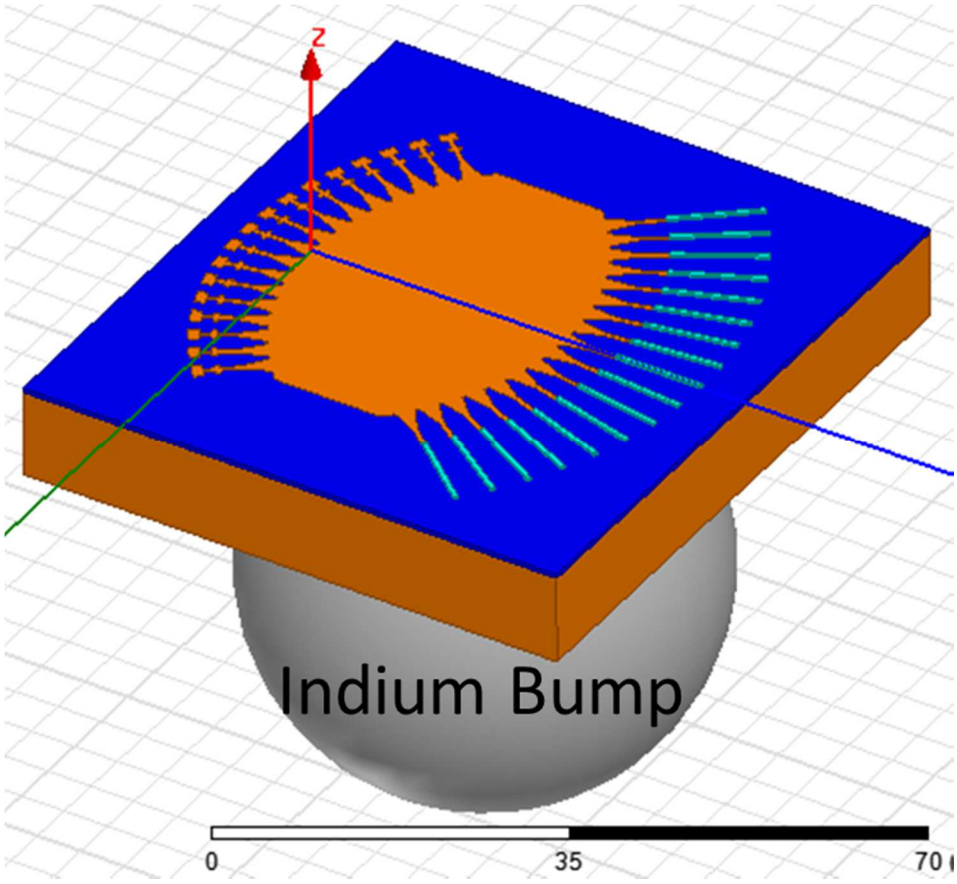

Figure 62 Indium Bump to Angle-Sensitive Star-Coupler Pixels

The system ground will be between the separate detectors on the top of the pixel. The individual detectors will be switched to read out ground. This will be either bonded from the top or wire bonded, but each similar detector can be connected. The "ground" will be switched to measure the individual pixels signals (Figure 63).

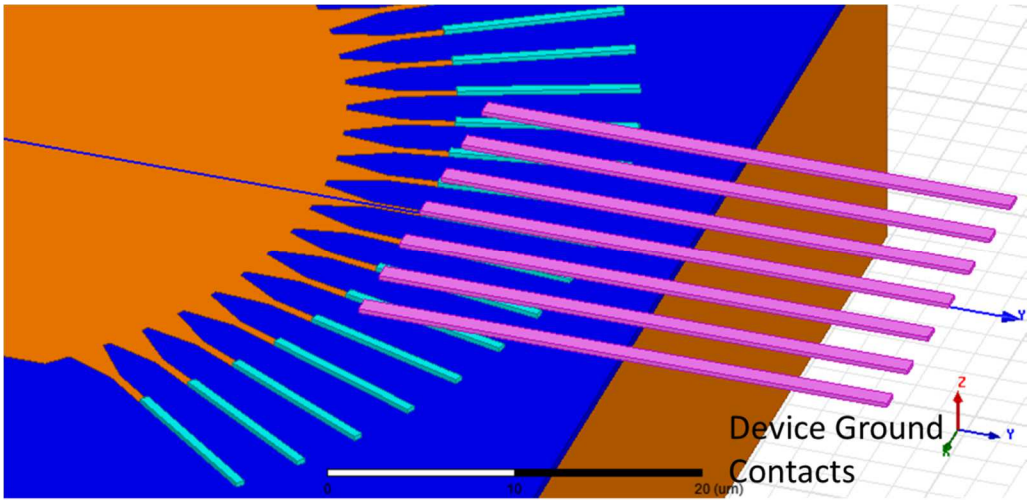

Figure 63 Device Contacts to Star Coupler

Imagine now, a single pixel with a unique angular response. This same concept applies, where there is an angular sensitive antenna array on top coupled to one pixel (Figure 64). Again, because signal comes from the top, the signal contact needs to be from the ground plane. All the detectors are connected to the system as ground.

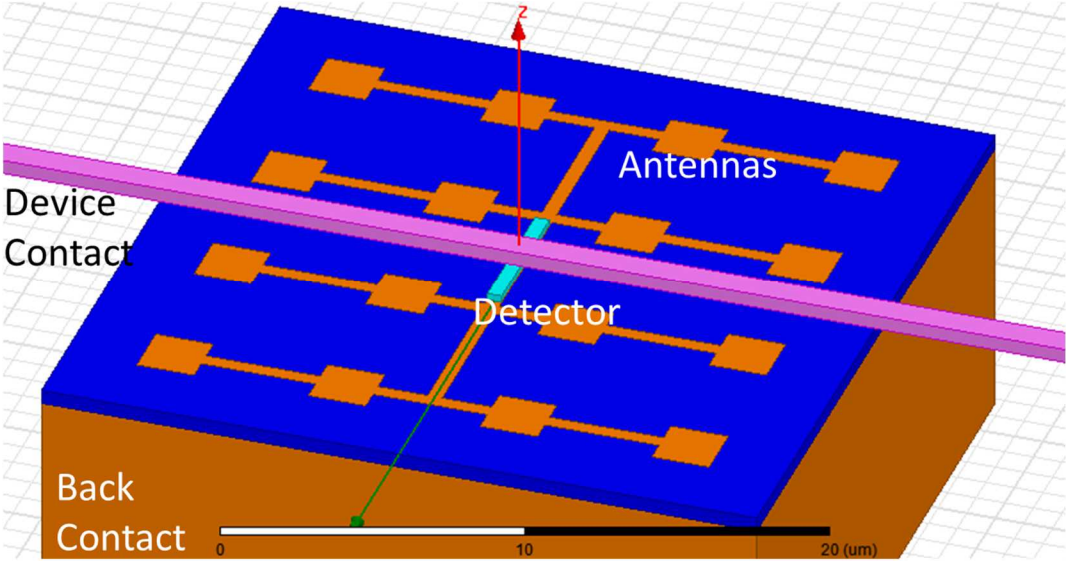

Figure 64 Concept for InP-Patch Array-coupled QWIP

VII. Microstrip Antenna Coupled QWIP

The microstrip platform is ubiquitous in microwave electronics and communications as an effective, inexpensive, compact, and simple way to transmit energy in the microwave regime that can be easily integrated with electronic components. By using conventional photolithography techniques, microstrip waveguides and antennas can be fabricated on a planar surface and can support modes smaller than dielectric waveguide over a long distance. [52]

Antennas were first scaled down to the mid-infrared by coupling a micro-bolometer to a spiral antenna. [53] This eventually led to the development of Metal Oxide Metal Diodes for detection [54] [55] [56], and the demonstration of beam forming. [57] In this same range, microstrip antennas coupled to microbolometers have been demonstrated. [58]

This approach to infrared detection has yet to be shown using higher-detectivity materials that are typically used in mid-infrared Focal Plane Arrays (FPAs) such as Quantum Well Infrared Photodetectors (QWIP). The type of metal optics and antennas used for enhancement of these materials instead utilize nearfield enhancement, for example: Metal Hole Arrays [41], Metal Resonators [59], and Individual Patch Antennas. [60]

QWIP, specifically, would be a natural fit for microstrip antennas and waveguides. The TE polarization of integrated microstrip waveguides would directly couple to the perpendicular absorption of quantum wells as grown on a substrate. [61] Also, QWIP has relatively low responsivity compared to materials like HgCdTe [62] and would benefit from the concentration of power by a guided mode. Additionally, as a confined detector based on microstrips, QWIP could be compact in both thickness and area, sharply reducing the dark current noise.

Additionally, beyond the common considerations for QWIP that this platform would address, we also consider extending other microwave concepts to this platform, such as beam forming, and potentially steering, which would prove useful for typically long-wavelength applications such as RADAR (IRDAR) and Synthetic Aperture [63], or short-wavelength applications such as lensless imaging [35]. Finally, we would like to point out the ability of this to be compartmentalized; that is, the different antennas, beam splitters, waveguides, and detectors can be utilized in any order with other microwave concepts in ways we may not have considered yet.

We propose a QWIP detector based on microstrip antennas and waveguides. We couple patches designed for 8um to waveguides, which are in turn coupled to a strip of QWIP. Additionally, we demonstrate off-angle detection, or beam forming, with this detector that could potentially be

used for lensless imaging.

A. Modular Design of Antenna-coupled QWIP

With this fabrication process in mind, a waveguide was designed with an infinite layer of gold on the bottom (the bonding metal), etched BCB (designed to be the same height as QWIP), and a metal strip. We are constrained by materials dielectric height when designing, and have 3 parameters we must consider separately: strip width, undercut, and strip metal thickness. With both the width and undercut we must consider the tradeoff between mitigating process variations and loss. With the waveguide thickness the tradeoff is between loss and antenna reflection (discussed later)

To simulate these antennas, we used the Eigenmode solver in Ansys Electronics Desktop 2016 (an HFSS design). We used a method that sweeps a phase across a thin slice of waveguide and solves for frequency [16]. From this we can deduce mode index and loss (Figure 65).

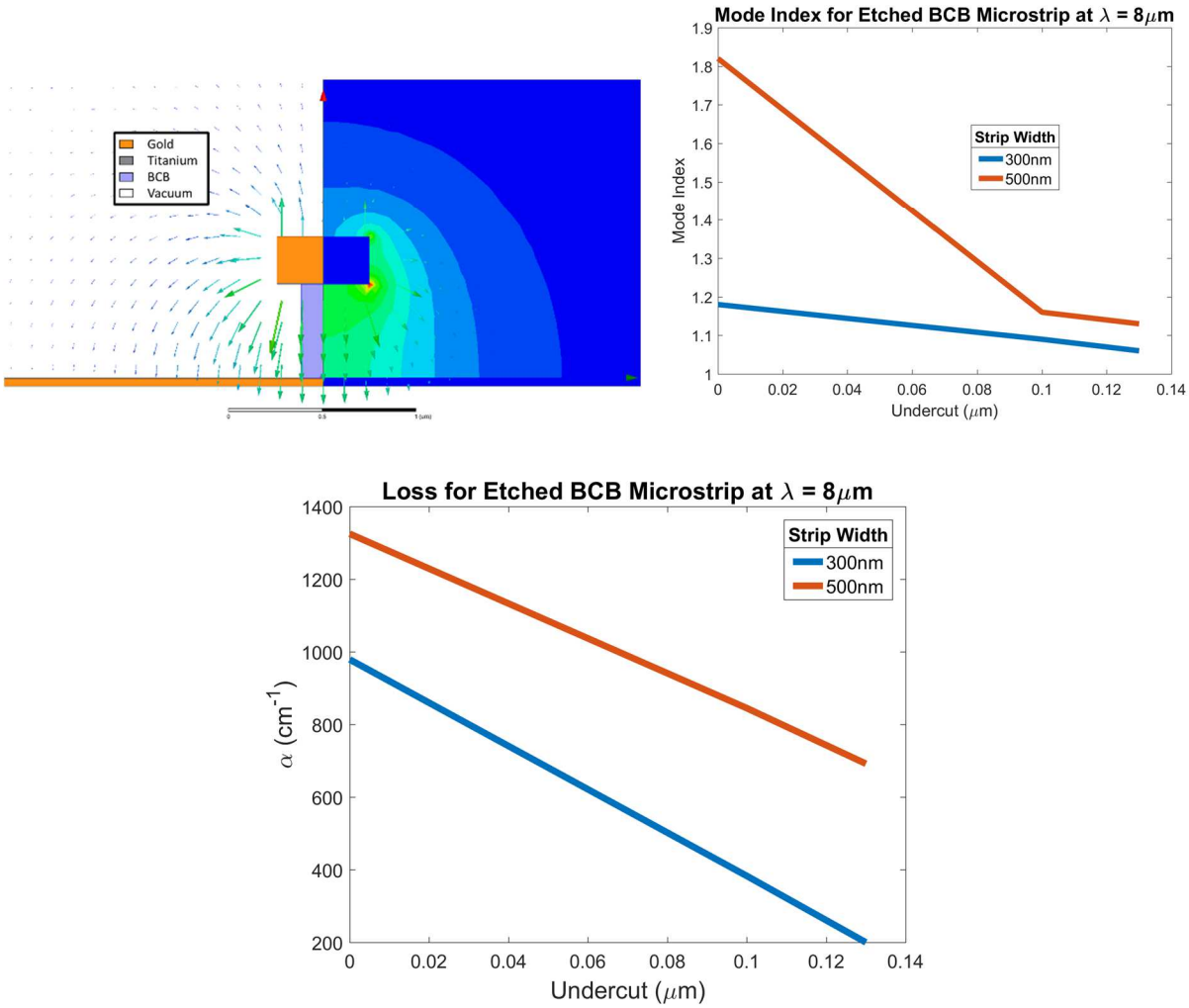

Figure 65 a) Field Distribution of etched BCB microstrip waveguide b) Mode Index of BCB Microstrip Waveguide c) Mode absorption of etched BCB Microstrip Waveguide

We found that, due to metal loss and BCB loss in the mid-infrared, these waveguides orders of magnitude lossier than typical dielectric waveguides or similar waveguides in the microwave regime. However, at least in this discussion, we are interested in travel over only 10's of μm in length so this is acceptable.

Based on our Electron Beam Lithography capabilities and our RIE process, we choose 0.5μm width waveguides with 0.13μm undercut for our process. Due to the lack of proximity effect correction and inconsistency in sample flatness, this allows us some room for error while still avoiding collapse.

The Detector is designed to a microstrip replacing the BCB with etched QWIP material fed

radiation by the etched BCB waveguide. The QWIP is based in Indium Phosphide (InP) with Indium Gallium Arsenide quantum wells designed for $\lambda = 8\mu m$ [65]. These 8 periods are 500nm thick

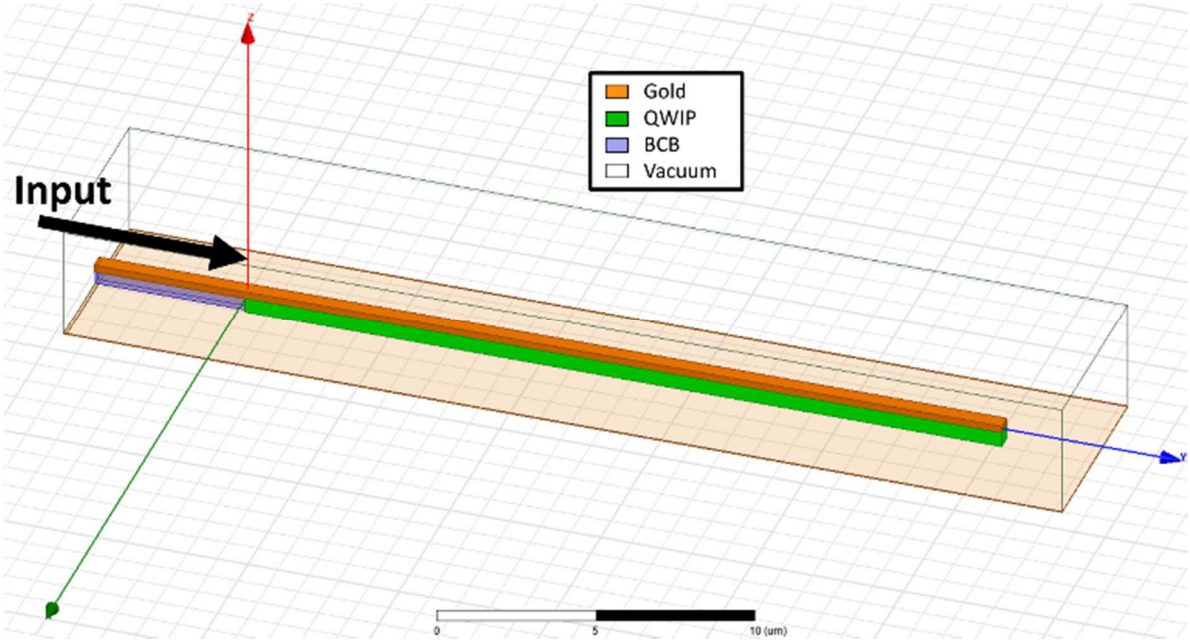

Figure 66 Microstrip Coupled QWIP

There is a Fabry-Perot effect in this detector, so we must extend it long enough such that process variation isn't a factor. However, we also want to reduce dark current noise, so it can't be extended much further. In HFSS, using a modal solution, an etched BCB waveguide is excited and coupled directly to a microstrip QWIP detector (Figure 66). The length of the detector is swept and reflected signal, radiated power, and Quantum Efficiency in the QWIP [18] are monitored (Figure 67).

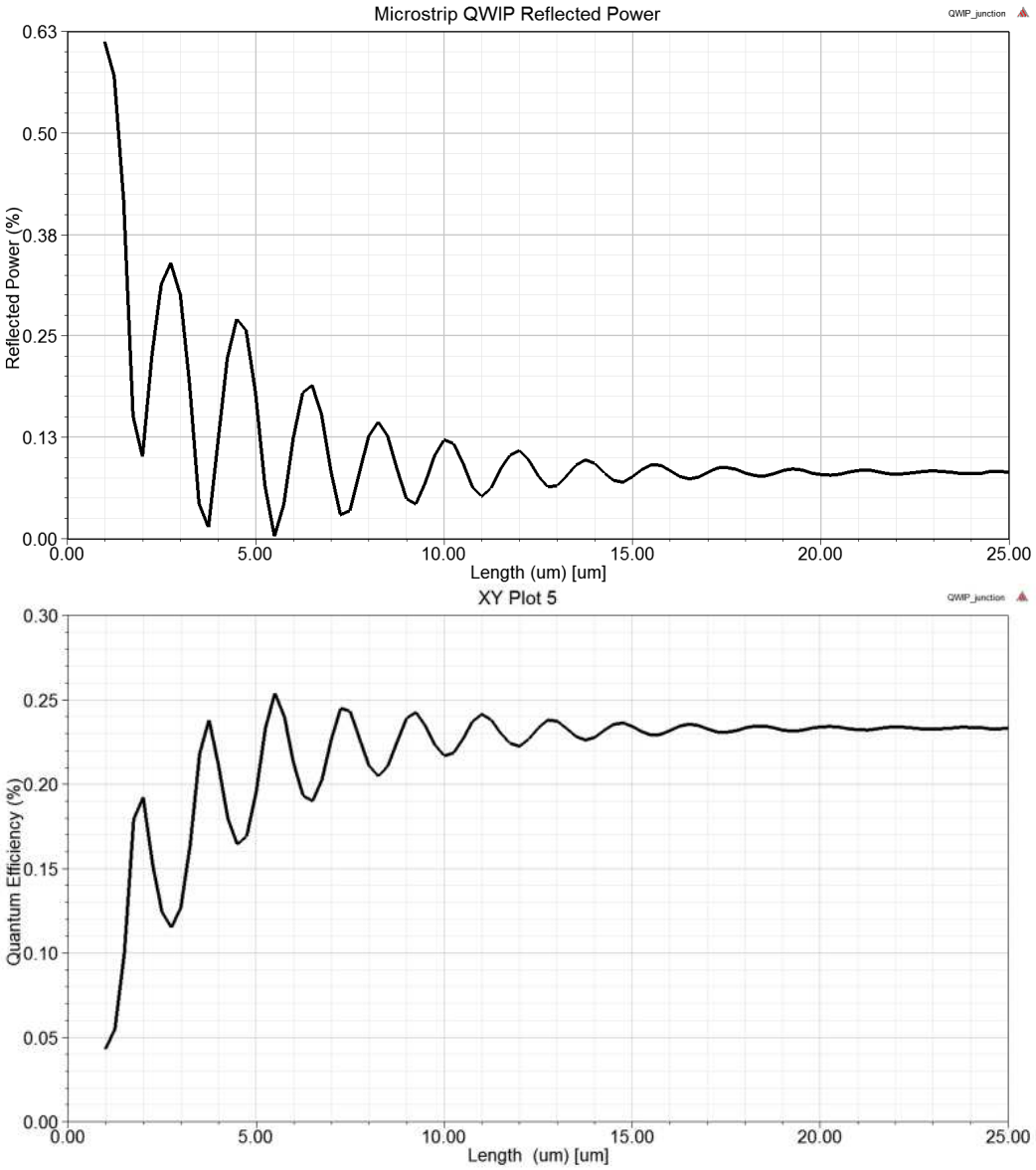

Figure 67 Radiated Power and Quantum Efficiency of QWIP vs. Length

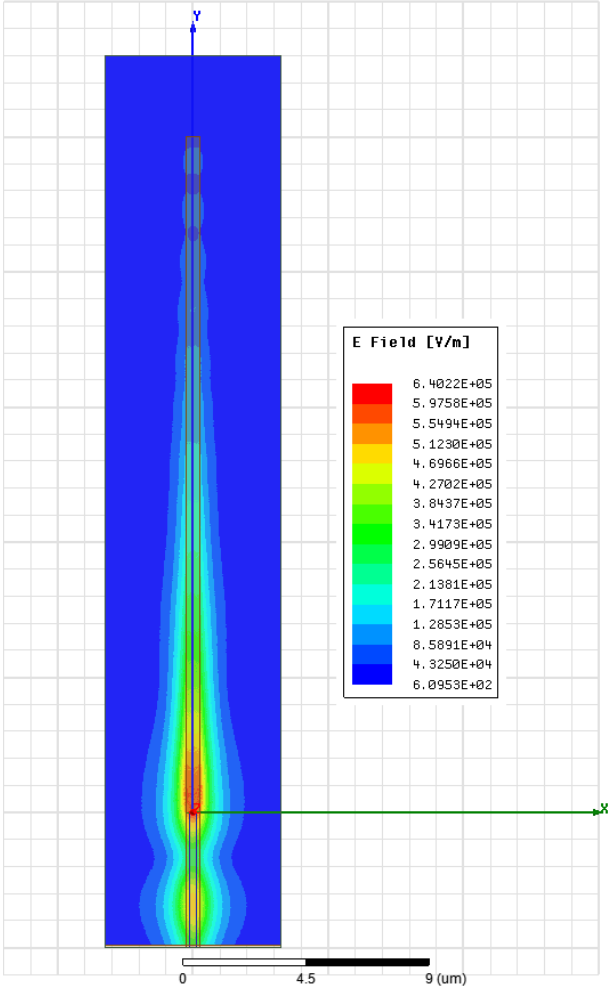

Figure 68 Top view of electric field magnitude along microstrip coupled QWIP

As shown in Figure 67 and Figure 68, the device converges at ~20µm. Figure 9 shows visual confirmation of the decay of radiation in QWIP using a 25µm long detector. Assuming we use a 25µm long detector, it has a QE of 24%. 8.2% of the power is reflected at the interface, 5.2% of the power is radiated, and the rest is lost in the gold. It is also worth noting the significant reduction in size of the QWIP. The Electrical Area (A_e) is 25µm×0.5µm and the thickness (t) is 0.5µm, which leads to a reduced current noise, as $I_n \propto \sqrt{A_e t}$.

The simplest way to direct incoming radiation to our QWIP is with a single patch antenna (Figure 10). Like the QWIP structure, the patch is fed by an etched microstrip, measuring reflected, radiated power, and quantify antenna directivity/gain (Figure 69). The antenna will be used in practice to accept radiation, but this simulation is valid due to reciprocity.

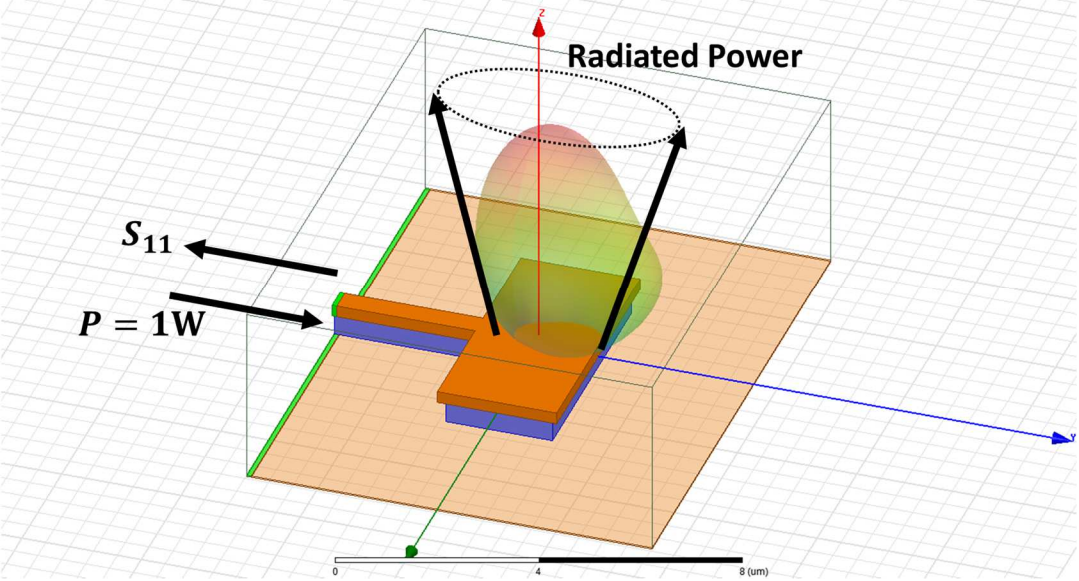

Figure 69 BCB Microstrip Patch Radiation

The dimensions that give a minimum S_{11} and highest radiated power is 5.25µm × 2.5µm (width × length). The reflected power is 0.10% and the radiated power is 75.2%. This design is less directive than other simulated dimensions, with a $D_{max} = 5.57$ but it is still the most efficient, with $E_{ant} = 75.3\%$, with a majority of the loss due to metal and BCB which is exacerbated by the resonant nature of the antenna. Based on this efficiency, we can calculate an effective aperture of $21.3\mu m^2$ which is notably larger than the detector's electrical area ($12.5\mu m^2$).

A common figure of merit in evaluating infrared detectors is Specific Detectivity (D^*), and though this is dependent on the measurement conditions, we can compare to published data on the same material [65] to compare using known proportionalities [12]:

$$D^* = {D^*}_0 \frac{\eta}{\eta_0} \sqrt{\frac{A_{optical}}{A_{electrical}} \frac{t_0}{t}} \qquad (38)$$

The reference material had a ${D^*}_0 = 9 \times 10^{10} \text{cm}\sqrt{\text{Hz}}/\text{W}$, a quantum efficiency of $\eta_0 = 12\%$, and a thickness of $t_0 = 1.12\mu m$, corresponding to 20 periods of QWIP. In a typical detector, the optical and electrical areas are equal, but because the collection of radiation is separate from the absorption in our setup, we must consider this ratio. Our thickness (t) is .45µm corresponding to 8 periods of QWIP.

When calculating the quantum efficiency (η), we must the quantum efficiency of the detector (24%), but also the antenna efficiency (75.2%) for $\eta = 18.0\%$. A single patch antenna coupled

to a 25μm long QWIP under similar measurement conditions as the reference has a $D^* = 2.79 \times 10^{11}\text{cm}\sqrt{\text{Hz}}/\text{W}$, a 3.1× enhancement.

To improve the efficiency of a microstrip coupled patch antenna, you can add more in series (Figure 70). We looked at adding 2, 3, and 4 antennas in series (Table 2). We start to see diminishing returns after adding more than 2 antennas in series, as you can see in table

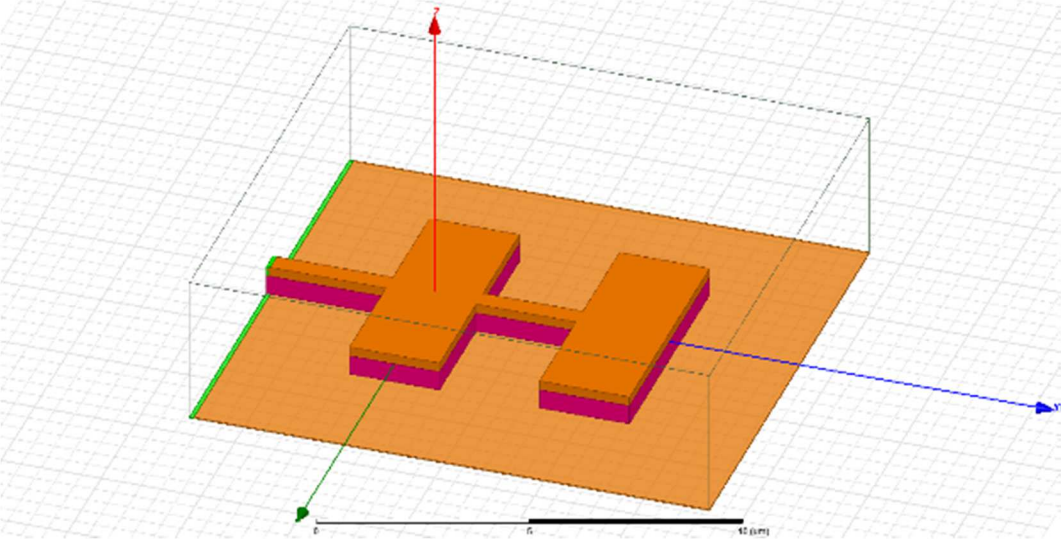

Figure 70 Series Coupled BCB Microstrip Patch

Table 2 – Predicted Performance of Patch-Coupled QWIP

Patches	Antenna Efficiency	Quantum Efficiency	Peak Gain	Effective Aperture	Relative D*
1	75.3%	18.0%	4.19	$21.3\mu\text{m}^2$	2.79×10^{11}
2	72.66%	17.4%	6.94	$35.3\mu\text{m}^2$	3.47×10^{11}
3	70.9%	17.0%	7.05	$35.9\mu\text{m}^2$	3.41×10^{11}
4	70.9%	17.0%	7.01	$35.7\mu\text{m}^2$	3.38×10^{11}

The final design presented is a 2x2 antenna to allow phase control between two antennas and ultimately off-angle beam forming. The antenna was designed with 2 sets of 2 antennas in series connected by a y-coupler (Figure 71). Due to loss from the coupler, this antenna is less efficient than the series antennas, but has the advantage of being able to shift phases and steer in the y-dimension.

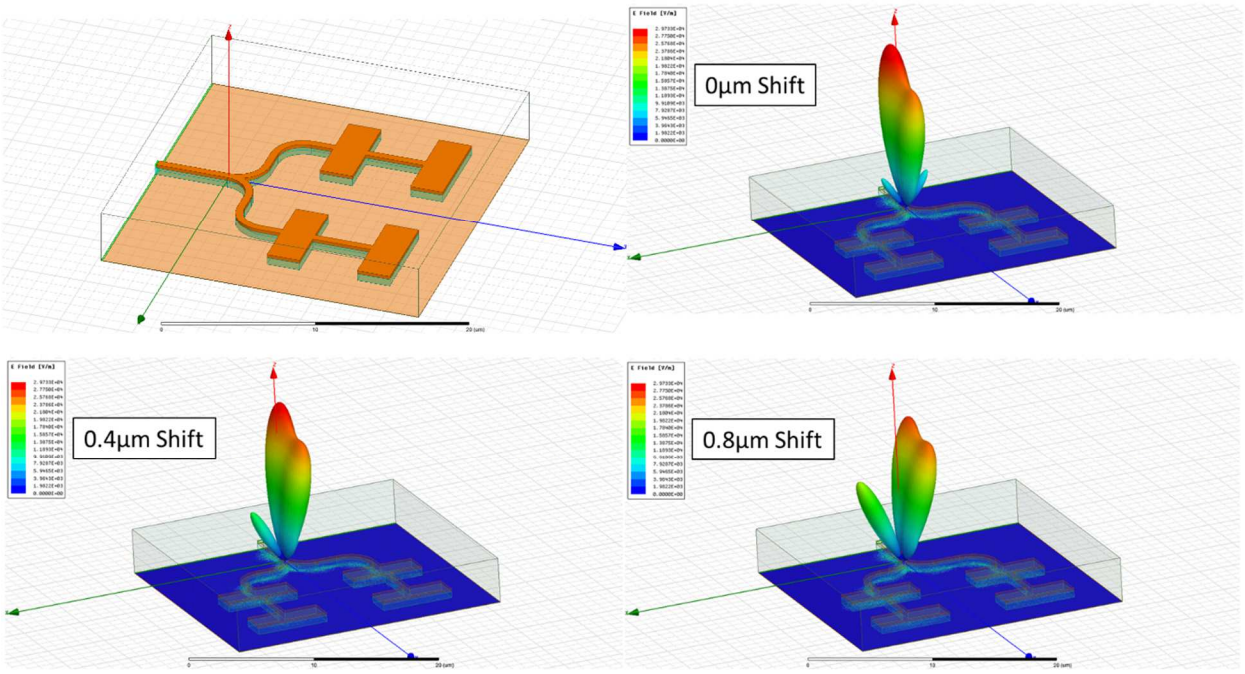

Figure 71 2x2 antenna layout and accepted beams from different angles

The device designed above requires a thin semiconductor on top of an "infinite" layer of gold in plane with a dielectric with small loss in the infrared, all etched. Fabricating this device is not trivial and required multiple new fabrication techniques.

B. Microstrip Coupled QWIP Fabrication

In order to have a thin, small-volume QWIP resting on metal, as designed, we needed to develop a process to bond to substrates together and then thin a III-V substrate. We started with QWIP grown on InP (the device) and silicon (mechanical substrate). We thoroughly cleaned both, and evaporated 20nm of gold on each. We then activated the surface with argon plasma. Immediately after pulling out of the plasma chamber, the two were pressed together by hand, with a thumb. Finally, this sealed device was taken to the flip chip bonder, and pressure (35kg) and heat (200ºC) were applied to this sample.

Once the two were together, the substrate was removed leaving just QWIP on gold on silicon. You can see a cross-section of this process in Figure 72a and a photograph of one of these thinned QWIPs in Figure 72b.

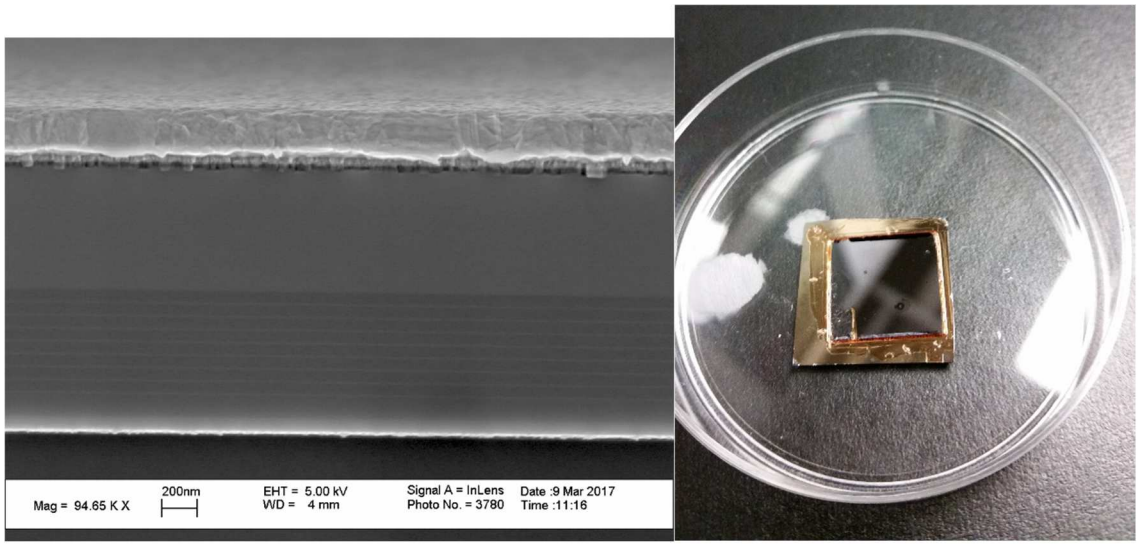

Figure 72 Bonded QWIP to metal-on-silicon substrate

At the very end of the process we must wirebond to test these devices. This very-last step is directly connected to the very first step after the substrate is removed, oxidation. As we found out early on, wirebonding to a metal directly on BCB doesn't work, as it punches through and completely shorts the device, so we needed a mechanically stable oxide that wouldn't allow current flow through.

First, we tried electron-beam evaporated silicon oxide, but this cracked and allowed shoring of the devices at the end of the process, so finally we tried a low-temperature PECVD oxide grown at 200ºC. Ellipsometry showed no difference between this and high-temperature PECVD (normally 350 ºC).

Next, this oxide was patterned and etched to define both the bond pad and the initial detector etch mask. This pattern is made with a laser writer and this photoresist mask is used to etch the oxide with a CF_4 RIE, as shown in Figure 73.

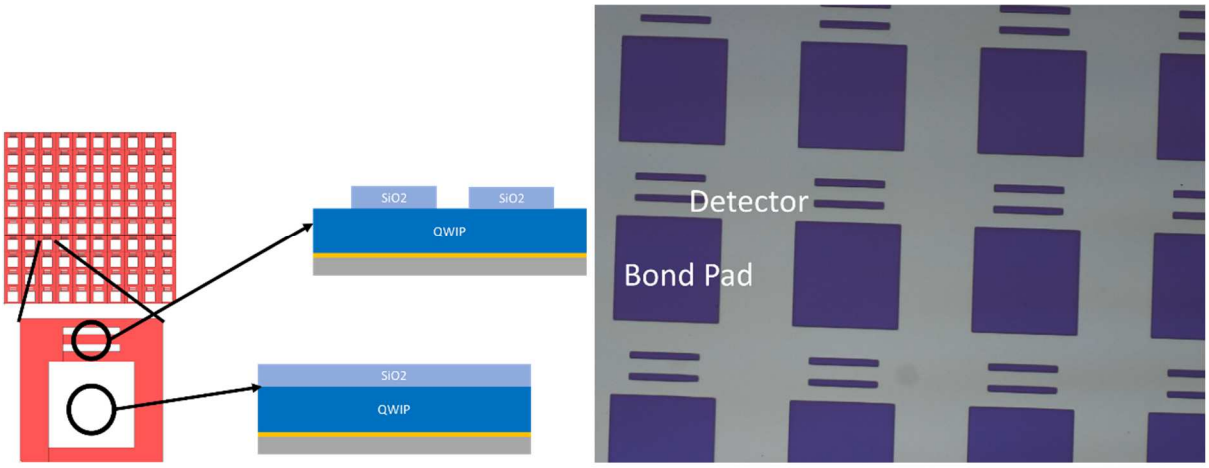

Figure 73 Oxide pad and stripes on QWIP

Using this oxide pattern as a mask, the exposed III-V semiconductor is etched in a Hydrogen:Methane (H2:CH4) for 10min exposing the bottom metal (Figure 74).

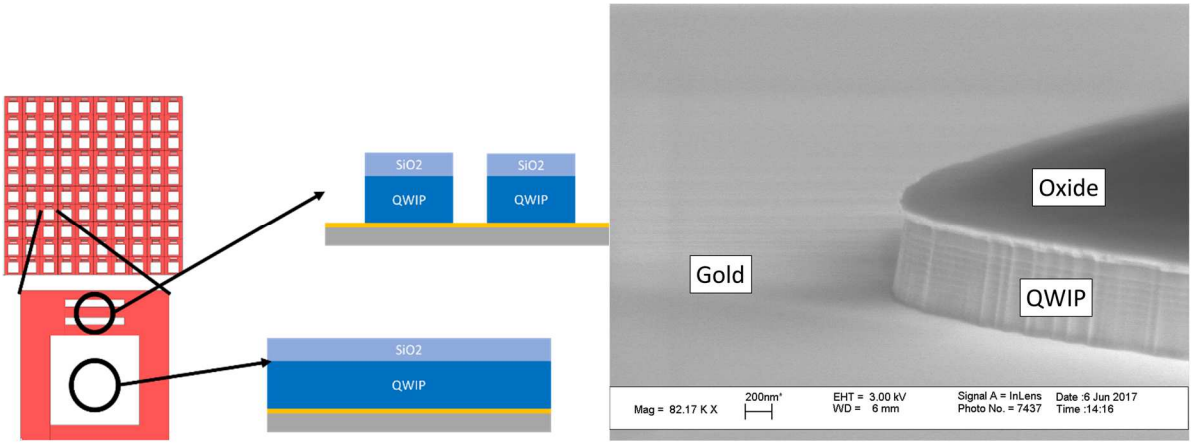

Figure 74 Initial III-V Etch Defining QWIP stripes and contact pedestal

The next step is to planarize and etchback the dielectric. We chose Benzocyclobutene (BCB) as it can conform to features on a chip/planarize and is relatively low loss at 8µm. BCB is spun onto the sample at 4000rpm for 1 min and baked for 2+ hours at 250ºC to cure/harden. This is then etched in an O2:CF4 plasma until the BCB is about flush with the top of QWIP (Figure 75).

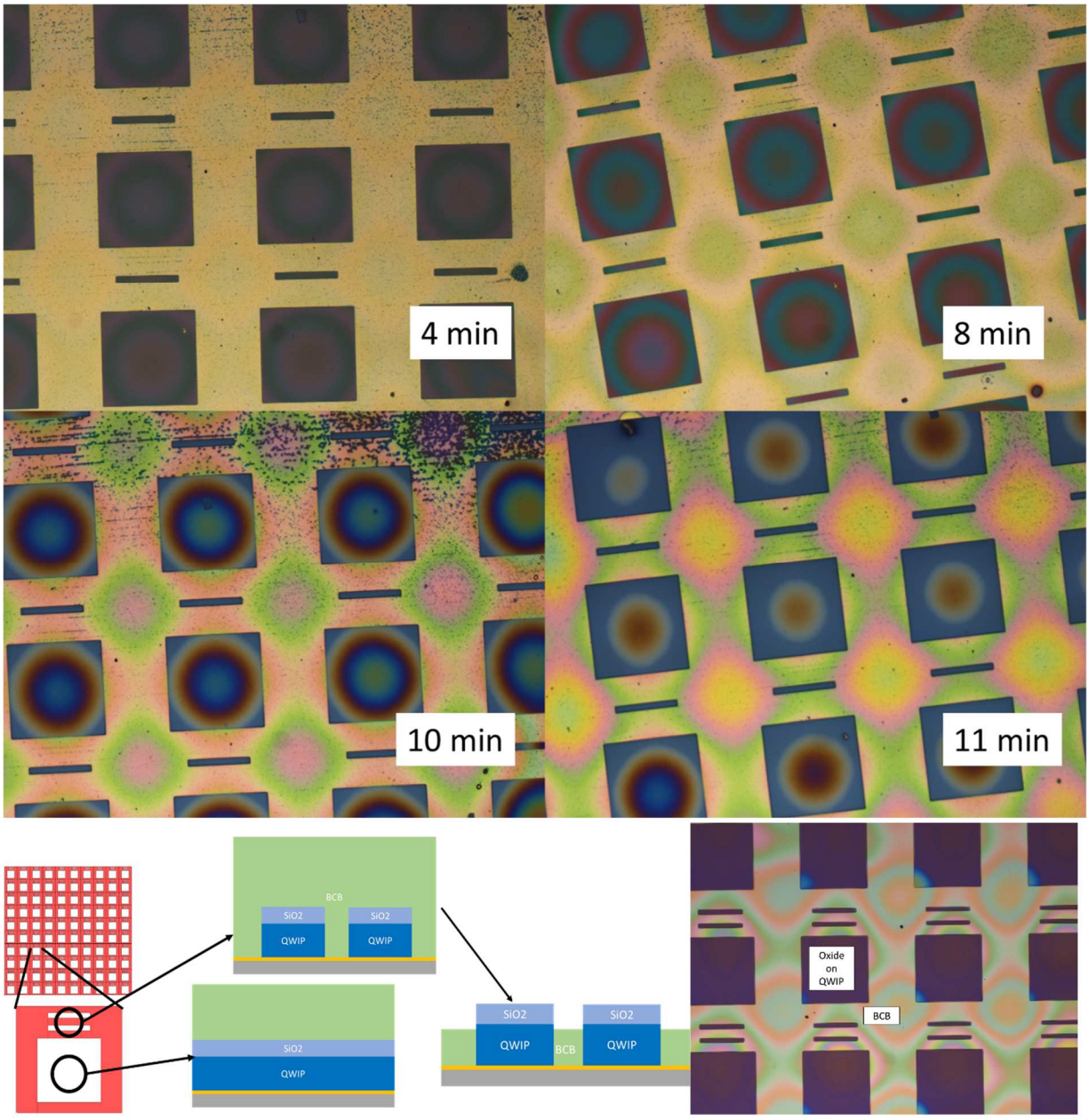

Figure 75 a) BCB Etchback Progression b) Cross-section schematic c) Final etch back

Next, the device is again patterned with the laser writer, this time to expose the two stripes and block the pad for SiO2 removal with Buffered Oxide Etch (BOE). This opens the stripes to contact to deposited metals, while leaving the pad insulated from the substrate (Figure 76).

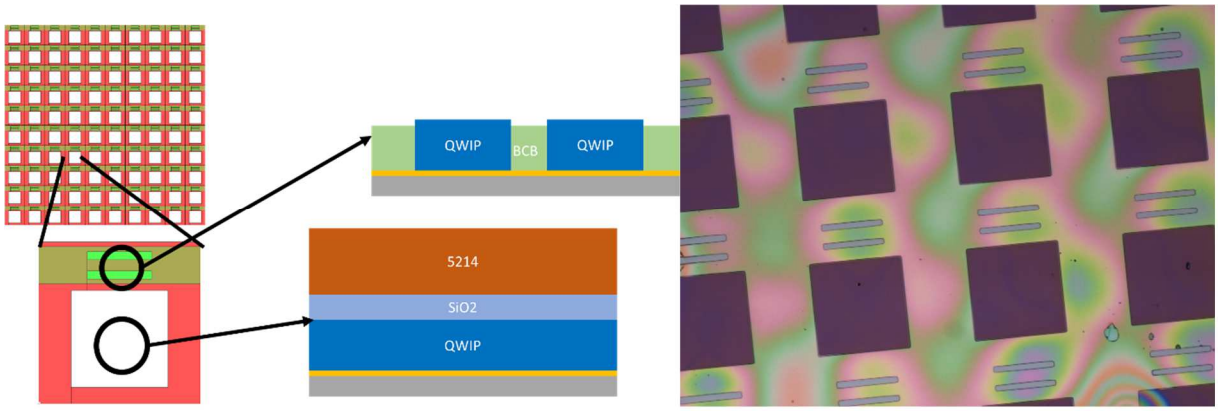

Figure 76 Strip Oxide Removal

Next was to define the antenna itself. Because the smallest feature in the design was 500nm, E-beam lithography is necessary. We used a bi-layer of MMA/PMMA to allow for metal lift-off after lithography (Figure 77).

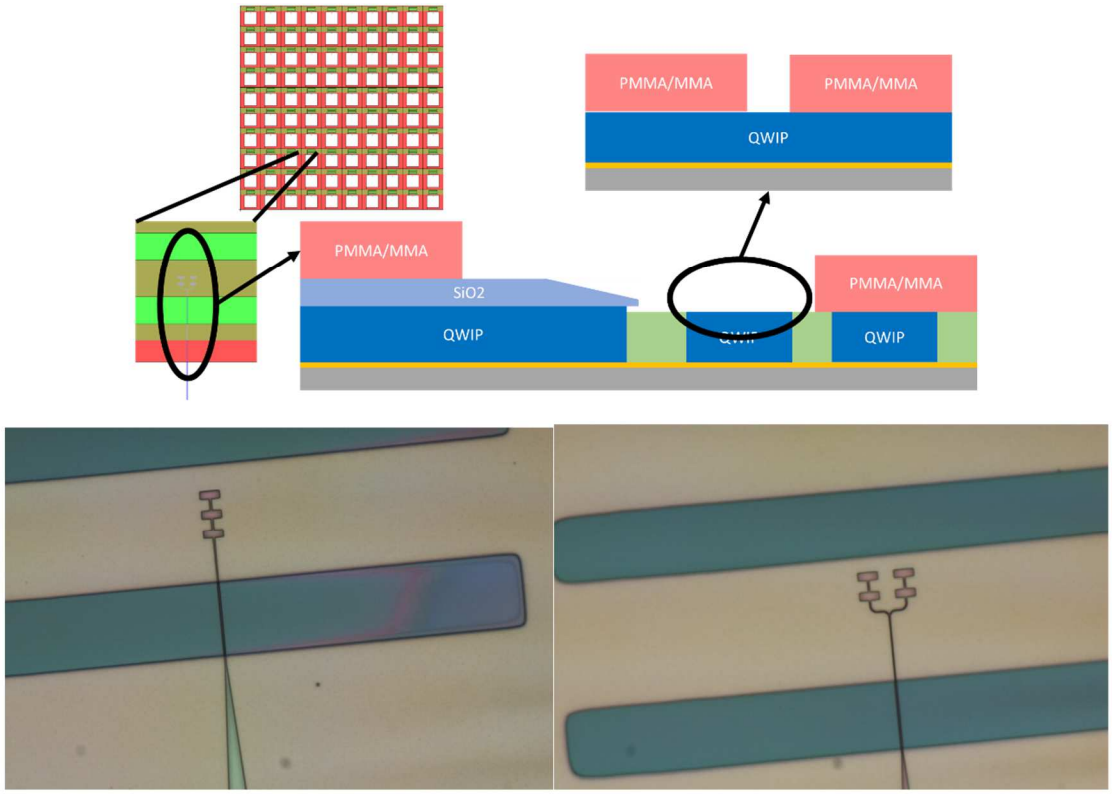

Figure 77 a) Cross-section schematic of Electron Beam Lithography for Antennas b) 3-patch series antenna c) 2x2 0° antenna

In these patterns, 250nm of Au was evaporated to act as both the antenna, microstrip, and top contact to the QWIP (Figure 78).

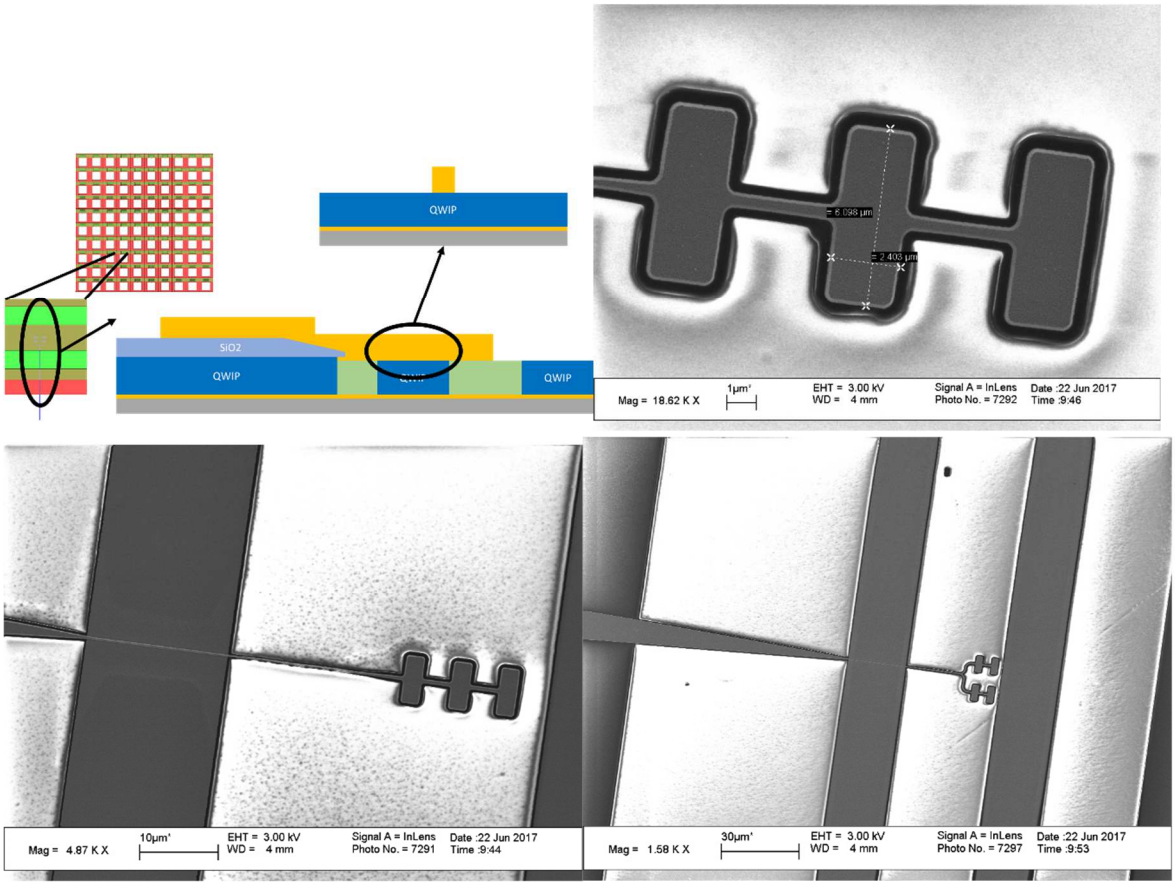

Figure 78 a) Antenna lift-off cross section b) c) d) Antenna lift-off over QWIP stripes

To finish the antenna and QWIP fabrication, everything around must be etched. With the waveguide this is necessary to minimize loss and with the detector, this is required to minimize dark current. The semiconductor is etched first due to its sensitivity and the risk of the BCB etch sputtering organics onto the surface (Figure 79). We use the same etch recipe as before to remove the III-V

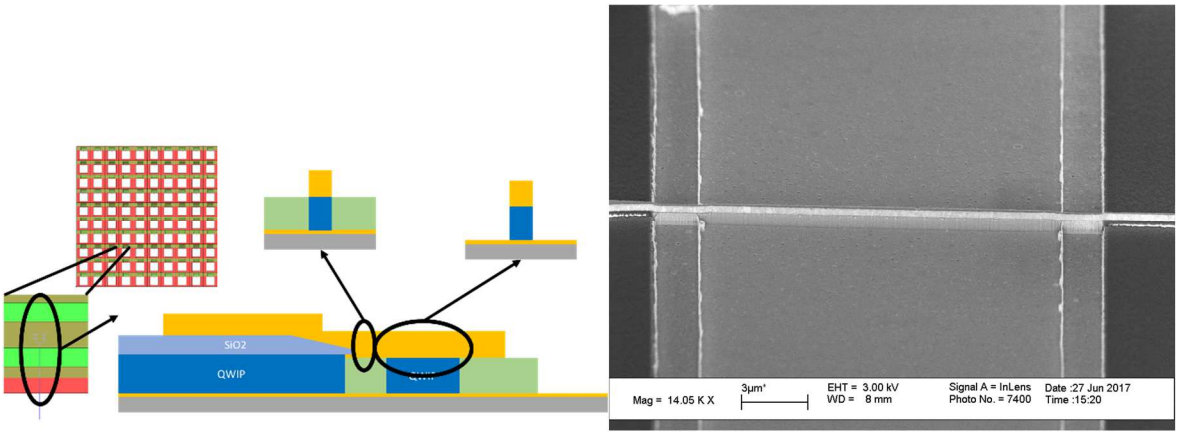

Figure 79 III-V Etch to define final microstrip-coupled QWIP

Again, using a similar recipe used to etch BCB previously, we etch the BCB to form the antennas and waveguides as designed. Note that this had to be adjusted to lower the undercut of the etch.

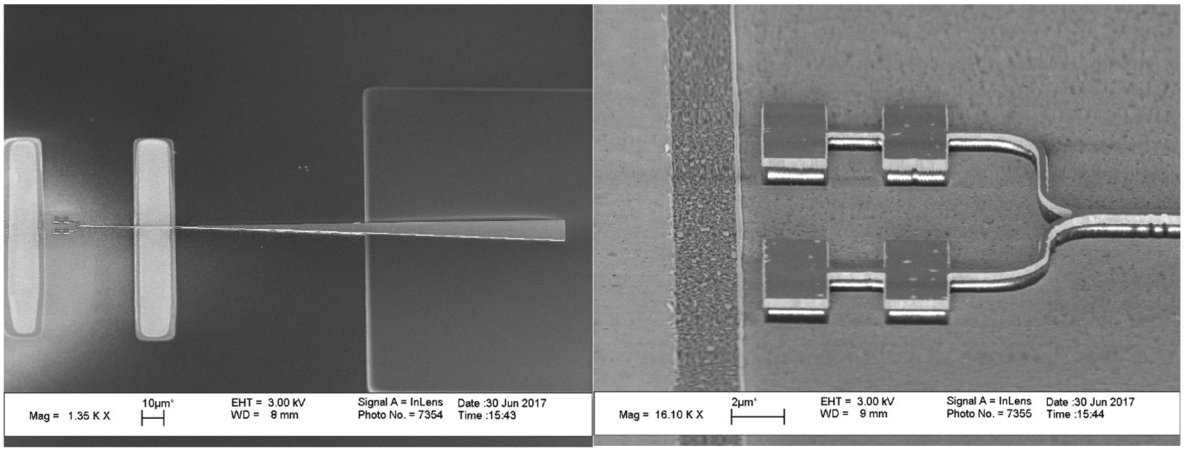

Figure 80 BCB Etch to Define Final Antenna

Finally, the device is made, but to access it for wirebonding, we must create the bond pad. A 250µm × 250µm pad is patterned and lifted off on the oxide pedestal made at the beginning (Figure 81). The metal stack is 5nm Ti/220nm Ni/30nm Au.

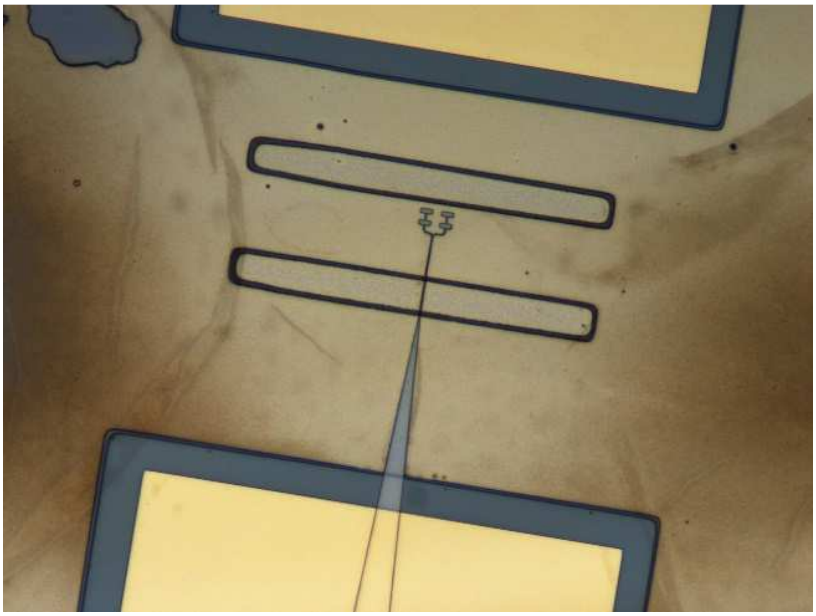

Figure 81 Completed Antenna-Coupled QWIP Device

C. Microstrip Coupled QWIP Measurement

Measurements of initial devices proved unsuccessful as we expect a relatively weak signal from this device. With the measurement in mind, the most recent iteration of these devices had 7 or 8 identical devices per contact pad (Figure 82)

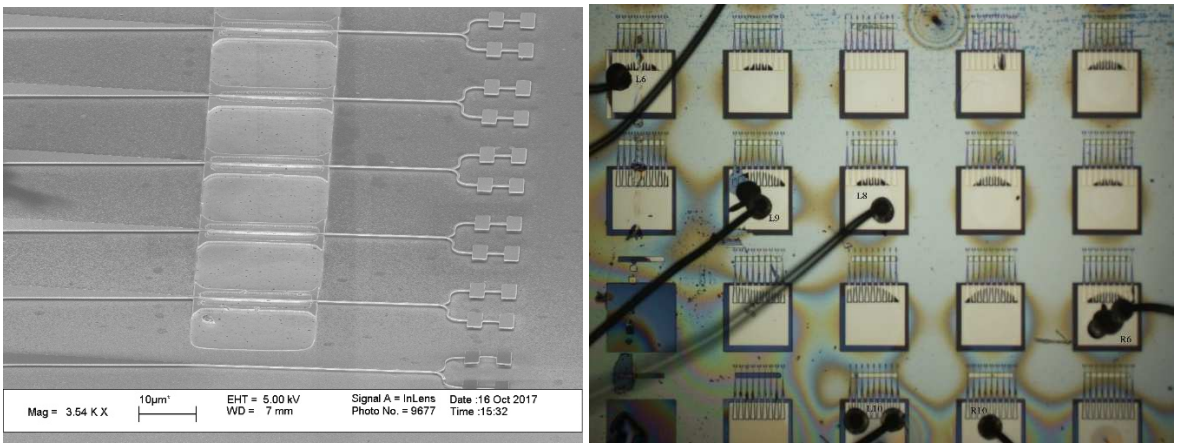

Figure 82 Array of Microstrip-Coupled QWIP to Same Contact Pad

From experience we worried about biasing these devices too aggressively and melting the gold over BCB, as these waveguides are only 500nm wide (Figure 83)

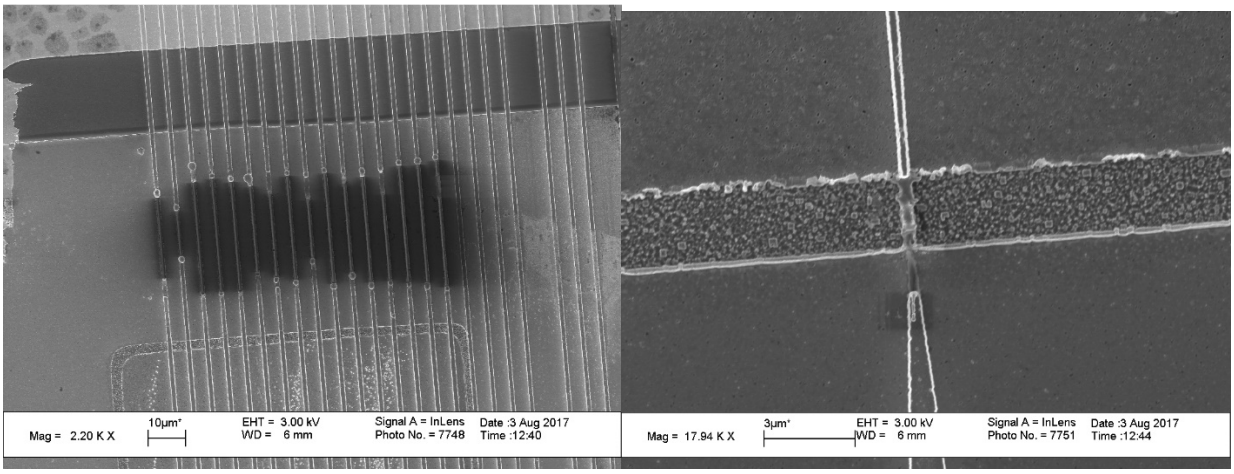

Figure 83 a) Burned BCB contacts to QWIP gratings b) burned BCB contact to QWIP Microstrip

Data was collected on a handful of devices with a large variation in performance, so far. The following data is strictly for the one device measured with signal. Figure 84 shows the dark current for this device, a QWIP antenna with 3 patches in series. Note that all QWIP microstrips designed are the same; the antenna design won't impact dark current.

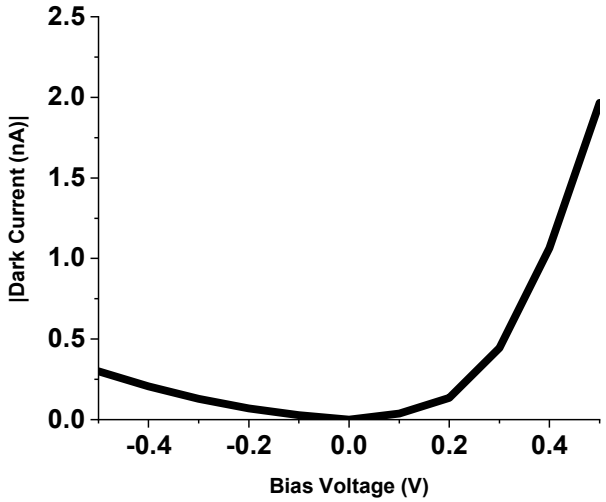

Figure 84 Low-Bias Dark Current for Microstrip QWIP

The photocurrent was too weak and the device too unstable to measure signal with the FTIR, as we'd desire. However, we can look at a broadband signal using filters and a chopper. Figure 85 shows a time response of QWIP current in time in line with a 2kHz chopper.

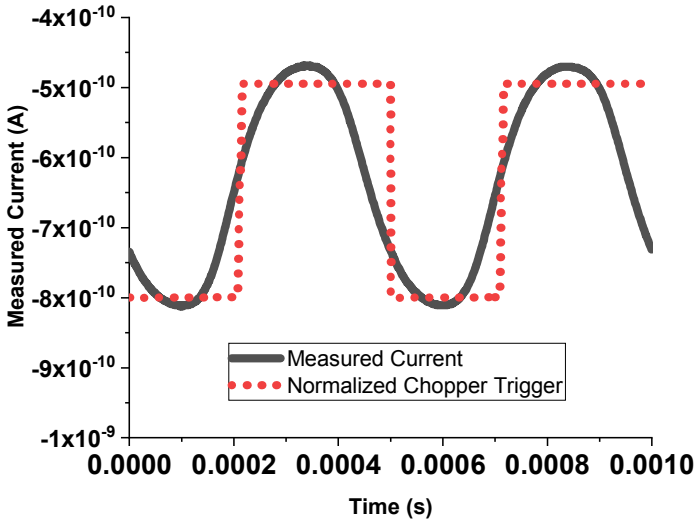

Figure 85 Chopped Measured Current from Microstrip-Coupled QWIP

This signal is proven to be QWIP by gain; with increased bias, the peak-to-peak current of this signal increases significantly, which wouldn't happen in the absence of semiconductor gain.

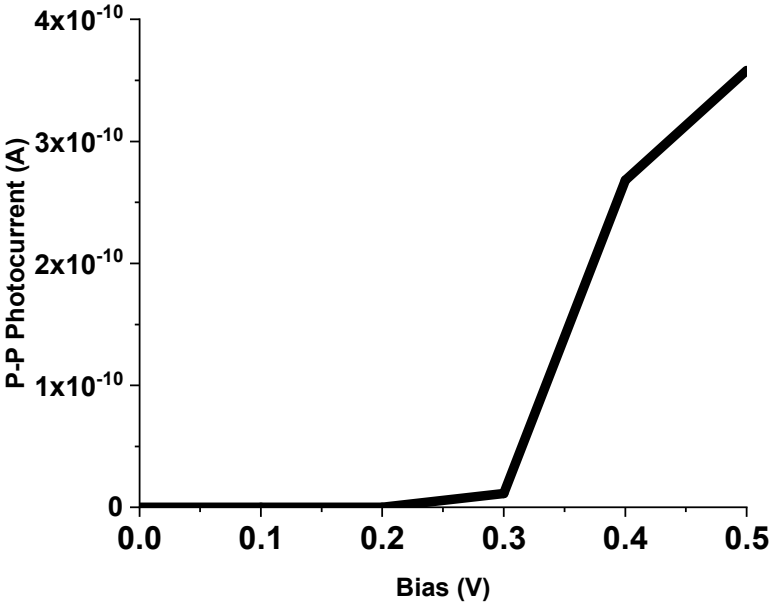

Figure 86 Increased Photocurrent with Bias for Microstrip-Coupled QWIP

I also looked at the polarization response of this device. Simulation predicts that this device is completely polarization-sensitive, but experimentally this is not the case. At the time of this

writing, we are still looking for the source of cross-polarization and ways to block the response of light directly onto the QWIP (not coupled by the antenna).

D. Future Directions for Microstrip-Coupled QWIP

We have demonstrated a straightforward, flexible, and easily-integrated platform for coupling microstrip antennas in the infrared with QWIP and potentially other semiconductors. In this section we are interested in future work, both in improving this platform and extending it to applications beyond infrared detection.

Solution-processed chalcogenide glass (CHG) is relatively high-index and lossless in the long infrared [68] and can be processed into many structures for a variety of photonic applications [69]. We attempted to replicate these processes in our lab, specifically with Arsenic Selenide (As_2O_3), and though we didn't have the exact toolset to make this work. We could deposit and mold films, but ultimately, they were porous and easily oxidized (Figure 87), and the BCB that we chose to use was easier to work with.

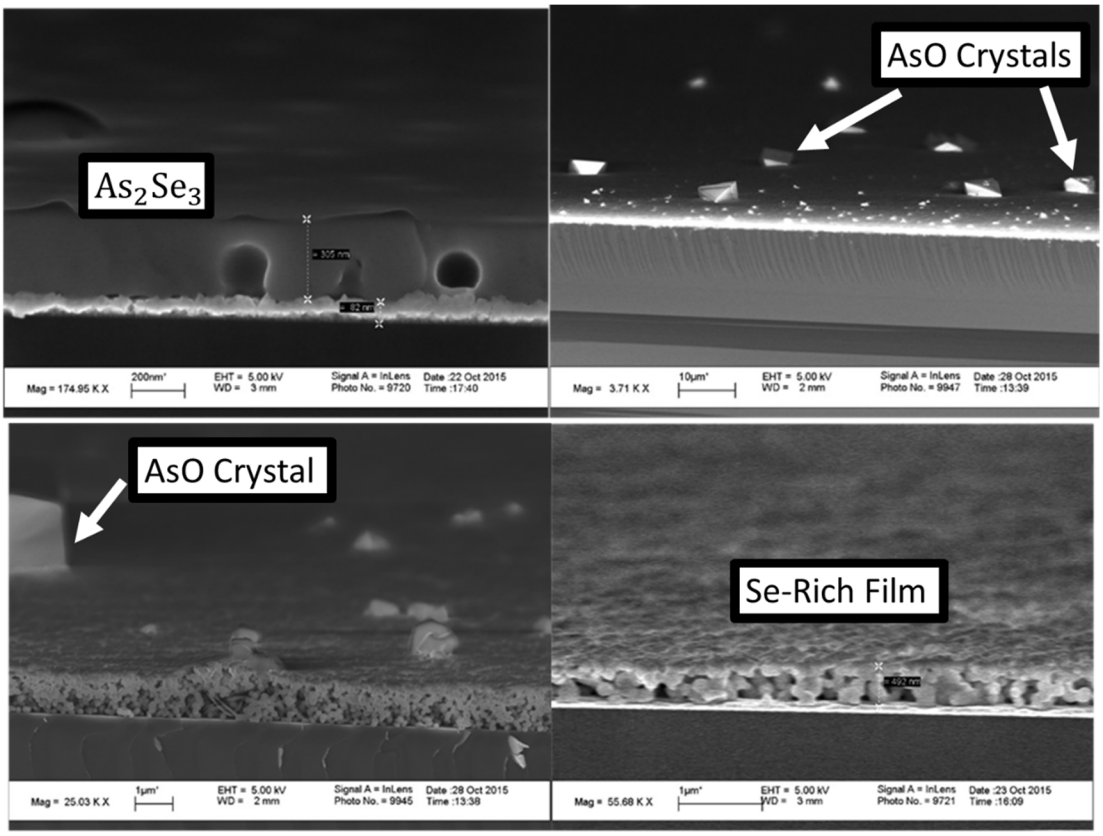

Figure 87 Attempts at depositing As_2Se_3 a) Large sparse pours b) AsO crystals in solid film c) AsO crystals in very porous film d) Selenide-rich Porous AsSe film

With further investigation and potential collaboration with groups with a working process, this material could replace BCB in our platform. There are two advantages: 1) This material is virtually lossless in the mid- and long-infrared. 2) This material provides mechanical and thermal stability that BCB doesn't provide. The tradeoff to using this material is that it is less compatible with other semiconductor processes, and must be deposited in a very special, controlled environment, and one of the main advantages of our process is its ease and compatibility. Nevertheless, from the perspective of device performance, this material is superior and could unlock potentials with bigger, more complicated antennas that have a higher loss.

From a systems perspective, this platform's modular design is very powerful. At its core this design has only 4 components integrated together, an antenna, a waveguide, QWIP, and a contact (Figure 88). In Practice, any of these components can be replaced and the other components will have the same functionality. This means that for example, the QWIP can be replaced with a Quantum Cascade Laser (QCL) and this device would emit directional radiation instead of receiving it.

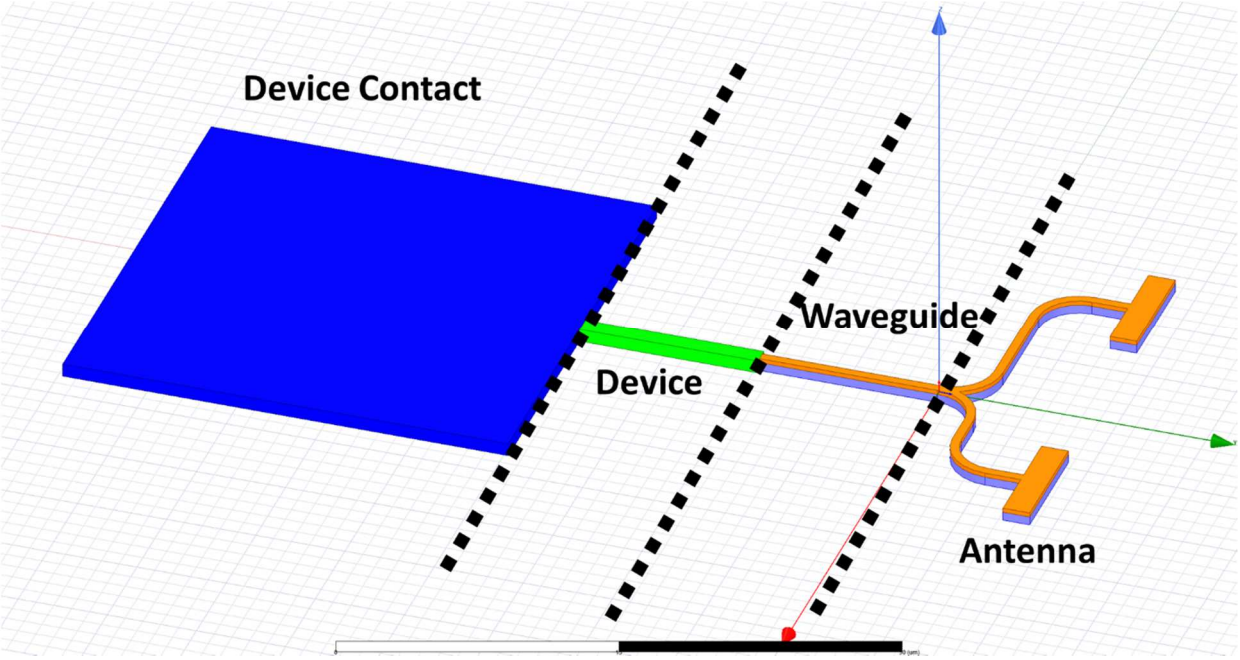

Figure 88 Modular Layout of Antenna-Coupled QWIP

VIII. Conclusion and Future Work

In conclusion, this thesis reported on a new process for flexible integration of infrared detectors with localized and de-localized antennas. More specifically, Quantum Well Infrared Photodetectors were fabricated for two different kinds of detectors: 1) Localized, reduced-volume QWIP to reduce dark current noise and boost performance, 2) delocalized, reduced-volume QWIP coupled with microstrip antennas with the same goals, and the flexibility for beam-steering and narrow-beam absorption.

Near field coupling to reduced-volume QWIP is advantageous because it has the potential to reduce dark current noise while maintaining or even increasing Specific Detectivity (D*). The first attempt at creating such a device involved a complicated three-dimensional structure imbedding QWIP inside of a metal hole array antenna. Though this device didn't work in the end it laid the groundwork for establishing fabrication processes and designs for these devices.

The second attempt at reduced-volume QWIP, enabled by a new metal-metal substrate bonding process used a much simpler grating design, achieved >0.1A/W Responsivity at only a 1V bias and reduces typical QWIP volume by ~10×. The functionality is proven to be a real signal by the complete polarization sensitivity; light polarized across the stripes is absorbed and polarized light in the direction of light isn't absorbed at all by QWIP. The responsivity/quantum efficiency was limited by the large sensitivity to duty ratio in the design and we would expect a 4× improvement with a proper dose, but this still outperforms the only other example of reduced-volume QWIP demonstrated [61] by about 40%.

Delocalized coupling to QWIP was inspired by Microwave Engineering. We took designs of patch antennas and microstrip waveguides and made them in the infrared. This platform lends itself very well to QWIP as it naturally re-directs the electric field across the quantum wells. We successfully fabricated these devices and made multiple novel processes. This platform expands greatly on the previous reduced-volume QWIP designs, as it allows for flexibility in design.

Though this antenna work is still ongoing, this process metal-to-metal bonding process is proven compatible with QWIP as demonstrated by the results from the reduced-volume grating. The addition of BCB microstrip antennas has opened the door for a flexible design of antenna-coupled QWIP with endless possibilities. We have created a platform for integration of a standard, static design of MSM semiconductor with a passive antenna that can open the door for many applications such as controlled emission and beam-steering.

IX. List of Figures

IX. References

[1] B. F. Levine, K. K. Choi, C. G. Bethea, J. Walker and R. J. Malik, "New 10 μm infrared detector using intersubband absorption in resonant tunneling GaAlAs superlattices," *Applied Physics Letters,* vol. 50, p. 1092, 1987.

[2] A. Rogalski, "Quantum Well Photoconductors in Infrared Technology," *Journal of Applied Physics,* vol. 93, no. 8, p. 4355, 2003.

[3] M. Reed, J. Randall, R. Aggarwal, R. Matyi, T. Moore and A. Wetsel, "Observation of Discrete Electronic States in a Zero-Dimensional Semiconductor Nanostructure," *Physical Review Letters,* vol. 60, no. 6, p. 535, 1988.

[4] S. Datta, Electronic Transport in Mesoscopic Systems, Cambridge University Press, 1995.

[5] H. Haug and S. Koch, Quantum Theory of the Optical and Electronic Properties of Semiconductors, Singapore: World Scientific, 1994.

[6] P. Bharadwaj, B. Deutsch and L. Novotny, "Optical Antennas," *Advances in Optics and Photonics,* vol. 1, p. 438, 2009.

[7] U. Fischer and D. Pohl, "Observation of Single Particle plasmons by Near-Field Optical Microcopy," *Physical Review Letters,* vol. 62, no. 4, p. 458, 1989.

[8] G. Boreman, A. Dogariu, C. Christodoulou and D. Kotter, "Dipole-on-dielectric Model for Infrared Lithographic Spiral Antennas," *Optics Letters,* vol. 21, no. 5, p. 309, 1996.

[9] P. Frigeri, L. Seravalli, G. Trevisi and S. Franchi, "Molecular Beam Epitaxy: An Overview," in *Comprehensive Semiconductor Science and Technology*, Elsevier, 2011, p. 480.

[10] D. Miller, Quantum Mechanics for Scientists and Engineers, New York, NY: Cambridge University Press, 2008.

[11] M. Razeghi, Fundamentals of Solid State Engineering, Springer, 2009.

[12] J. Zilko, "Metal Organic Chemical Vapor Deopostion: Technology and Equipment," in *Handbook of Thin-Film Deposition Processes and Technologies*, Norwich, NY, Noyes Publications, 2002, p. 151.

[13] D. McKinney, "http://www.nrl.navy.mil/," Naval Research Lab, 19 February 2014. [Online]. Available: http://www.nrl.navy.mil/media/news-releases/2014/a-roadmap-to-efficient-green-blue-ultraviolet-light-emitting-diodes. [Accessed 11 March 2016].

[14] R. Dingle and C. Henry, "Quantum Effects in Heterostructure Lasers". United States Patent #3,982,207, 7 March 1975.

[15] J. Faist, F. Capasso, D. Sivco, C. Sirtori, A. Hutchinson and A. Cho, "Quantum Cascade Laser," *Science,* vol. 264, no. 5158, p. 553, 1994.

[16] B. Levine, "Quantum-well Infrared Photodetectors," *Applied Physics Letters,* vol. 74, no. 8, p. R1, 1993.

[17] H. Schneider and H. Liu, Quantum Well Infrared Photodetectors, Heidelberg: Springer, 2007.

[18] J. Andersson, L. Lundqvist and Z. Paska, "Quantum Efficiency Enhancement of AlGaAs/GaAs Quantum Well Infrared Detectors Using a Waveguide with a Grating Coupler," *Applied Physics Letters,* vol. 58, no. 20, p. 2264, 1991.

[19] G. Sarusi, B. Levine, S. Pearton, K. Bandara and R. Leibenguth, "Improved Performance of Quantum

Well Infrared Photodetectors Using Random Scattering Optical Coupling," *Applied Physics Letters,* vol. 64, no. 8, p. 960, 1994.

[20] B. Levine, A. Zussman, S. Gunapala, M. Asom, J. Kuo and W. Hobson, "Photoexcited Escape Probability, Optical Gain, and Noise in Quantum Well Infrared Photodetectors," *Journal of Applied PHysics,* vol. 72, no. 9, p. 4429, 1992.

[21] Y. Yang, H. Liu, M. Hao and W. Shen, "Investigationon the Limit of Weak Infrared Photodetection," *Journal of Applied Physics,* vol. 110, p. 074501, 2011.

[22] S. Wadsworth and G. Boreman, "Analysis of Throughput for Multilayer Infrared Meanderline Waveplates," *Optics Express,* vol. 18, no. 13, p. 13345, 2010.

[23] A. Bonakdar and H. Mohseni, "Impact of Optical Antennas on Active Optoelectronic Devices," *Nanoscale,* vol. 6, p. 10961, 2014.

[24] N. Landy, S. Sajuyigbe, J. Mock, D. Smith and W. Padilla, "Perfect Metamaterial Absorber," *Physical Review Letters,* vol. 100, no. 20, p. 207402, 2008.

[25] C. Middlebrook, P. Krenz, B. Lail and G. Boreman, "Infrared Phased-Array Antenna," *Microwave and Optical Technology Letters,* vol. 50, no. 4, p. 719, 50.

[26] B. Slovivk, J. Bean and G. Boreman, "Angular Resolution Improvement of Infrared Phased-Array Antennas," *IEEE Antennas and Wireless Propagation Letters,* vol. 10, p. 119, 2011.

[27] W. Stutzman and G. Thiele, Antenna Theory and Design, Wiley, 2012.

[28] D. Pozar, Microwave Engineering, Wiley, 2005.

[29] L. Codreanu and G. Boreman, "Integration of Microbolometers with Infrared Microstrip Antennas," *Infrared Physics and Technology,* vol. 43, p. 335, 2002.

[30] E. Kinzel, R. Brown, J. Ginn, B. Lail, B. Slovick and G. Boreman, "Design of an MOM Diode-Coupled Frequency-Selective Surface," *Microwave & Optical Technology Letters,* vol. 55, no. 3, p. 489, 2013.

[31] K. Choi, M. Jhabvala, D. Forai, A. Waczynski, J. Sun and R. Jones, "Electromagnetic Modeling of Quantum Well Infrared Photodetecors," *IEEE Journal of Quantum Electronics,* vol. 48, no. 3, p. 384, 2012.

[32] B. Slovick, J. Bean, P. Krenz and G. Boreman, "Directional Control of Infrared Antenna-Coupled Tunnel Diodes," *Optics Express,* vol. 18, no. 20, p. 20960, 2010.

[33] J. Bean, A. Weeks and G. Boreman, "Performance Optimization of Antenna-Coupled Al/AlOx/Pt Tunnel Diode Infrared Detectors," *IEEE Journal of Quantum Electronics,* vol. 47, no. 1, p. 126, 2011.

[34] G. W. Stimpson, Introduction to Airborne Radar, SiTech Publishing, 3014.

[35] D. Stork and P. Gill, "Optical, Mathematical, and Computational Foundations of Lensless Ultra-Miniature Diffractive Imagers and Sensors," *International Journal on Advances in Systems and Measurments,* vol. 7, p. 2014, 30.

[36] A. Wang, P. Gill and A. Molnar, "Light Field Image Sensors Based on the Talbot effect," *Applied Optics,* vol. 48, no. 31, p. 5897, 2009.

[37] E. E. Chain, "Optical properties of vanadium dioxide and vanadium pentoxide thin films," *Applied Optics,* vol. 30, no. 19, p. 2782, 1991.

[38] D. Shelton, K. Coffey and G. Boreman, "Experimental demonstration of tunable phase in a thermoelectric infrared-reflectarray metamaterial," *Optics Express,* vol. 18, no. 2, p. 1331, 2010.

[39] J. Ginn, D. Shelton, P. Krenz, B. Lail and G. Boreman, "Polarized Infrared Emission Using Frequency

Selective Surfaces," *Optics Express,* vol. 18, no. 5, p. 4557, 2010.

[40] J. Faist, Quantum Cascade Lasers, Oxford, UK: Oxford University Press, 2013.

[41] W. Wu, A. Bonakdar and H. Mohseni, "Plasmonic Enhanced Quantum Well Infrared Photodetector with High Detectivity," *Applied Physics Letters,* vol. 96, p. 161107, 2010.

[42] S. Gunapala, B. Levine, D. Ritter, R. Hamm and M. Panish, "InGaAs/InP Long Wavelength Quantum Well Infrared Photodetectors," *Applied Physics Letters,* vol. 58, p. 2024, 1991.

[43] R. Brown, A. Bonakdar, O. Memis, V. Fathipour, S. Jang and H. Mohseni, "Embedded Plasmonic Quantum Well Infrared Photodetector," *Proceedings of SPIE, Infrared Sensor, Devices, and Applications III,* vol. 8868, p. 886808, 2013.

[44] R. Brown, A. Bonakdar, S. Jang, O. Memis and H. Mohseni, "Embedded Plasmonic-Enhanced Quantum Well Infrared Photodetector," *Proceedings of SPIE, Infrared Sensors, Devices, and Applications IV,* vol. 9220, p. 922005, 2014.

[45] J. Goodman, Introduction to Fourier Optics, Greenwood Village, CO: Roberts & Company Publishers, 1968.

[46] B. Saleh, Fundamentals of Photonics, Hoboken, NJ: John Wiley & Sons, Inc., 2001.

[47] R. L. Olmon, B. Slovick, T. W. Johnson, D. Shelton, S.-H. Oh, G. D. Boreman and M. B. Raschke, "Optical Dielectric Function of Gold," *Physical Review B,* vol. 86, p. 235147, 2012.

[48] S. Lee, A. Z. Ku, J. Montoya, W. Jang, S. Brueck, M. Sundaram, A. Reisinger, S. Krishna and S. Noh, "A Monolithically Integrated Plasmonic Infrared Quantum Dot Camera," *Nature Communications,* vol. 2, p. 286, 2011.

[49] K. Choi, C. Monroy, V. Swaminathan, T. Tamir, M. Leung, J. Devitt, D. Forrai and D. Endres, "Optimization of Corrugated-QWIPs, for Large Format, High Quantum Efficiency, and Multi-Color FPAs," *Infrared Physics & Technology,* vol. 50, p. 124, 2007.

[50] K. Choi, M. Jhabvala, J. Sun, A. Jhabvala, A. Waczynski and K. Olver, "Resonator-Quantum Well Infrared Photodetectors," *Applied Physics Letters,* vol. 103, p. 201113, 2013.

[51] Y. Chen, Y. Todorov, B. Askenazi, A. Vasanelli, G. Biasiol, R. Colombelli and C. Sitori, "Antenna-Coupled Microcavities for Enhanced Infrared Photodetection," *Applied Physics LEtters,* vol. 104, p. 031113, 2014.

[52] M. Smit and C. v. Dam, "PHASAR-Based WDM-Devices: Principles, Design and Applications," *IEEE Journal of Selected Topics in Quantum Electronics,* vol. 2, no. 2, p. 236, 1996.

[53] D. M. Pozar, Microwave Engineering, Danvers, MA: John Wiley & Sons, Inc., 2005.

[54] Grossman, S. E.N., J.E. and D. McDonald, "Lithographic Spiral Antennas at Short Wavelengths," *Appl. Phys. Lett.,* vol. 59, no. 25, p. 3225, 1991.

[55] C. Faumeaux, W. Herrmann, F. Kneubuhl and H. Rothuizen, "Nanometer thin-film Ni-NiO-Ni diodes for detection and mixing of 30 THz radiation," *Infrared Physics & Technology,* vol. 39, p. 123, 1998.

[56] J. Bean, B. Tiwari, G. Bernstein, P. Fay and W. Porod, "Thermal infrared detection using dipole antenna-coupled metal-oxide-metal diodes," *J. Vac. Sci. Technol. B.,* vol. 27, no. 1, p. 11, 2009.

[57] J. Bean, A. Weeks and G. Boreman, "Performance Optimization of Antenna-Coupled Al/AlOx/Pt Tunnel Diode INfrared Detectors," *IEEE J. Quant. Elec.,* vol. 47, no. 1, p. 126, 2011.

[58] B. Slovick, J. Bean, P. Krenz and G. Boreman, "Directional Control of Infrared Antenna-Coupled Tunnel Diodes," *Optics Express,* vol. 18, no. 20, p. 20960, 2010.

[59] I. Cordreanu, C. Fumeaux, D. Spencer and G. Boreman, "Microstrip Antenna-Coupled Infrared Detector," *Elec. Letters,* vol. 35, no. 25, p. 2166, 1999.

[60] K. Choi, J. M.D., J. Sun, C. Jhabvala, A. Waczynski and K. Olver, "Resonator-Quantum Well Infrared PHotodetector," *Applied PHysics Letters,* vol. 103, p. 201113, 2013.

[61] Y. Chen, Y. Todorov, B. Askenazi, A. Vasanelli, G. Biasiol, R. Colombelli and C. Sirtori, "Antenna-Coupled Microcavities for Enhanced Infrared Photo-detection," *Appl. Phys. Lett.,* vol. 104, p. 031113, 2014.

[62] D. Coon and R. Karunasiri, "New Mode of IR Detection Using Quantum Wells," *Appl. Phys. Lett.,* vol. 45, p. 649, 1984.

[63] A. Rogalski, "Quantum Well Photoconductors in Infrared Detector Technology," *J. Appl. Phys.,* vol. 93, no. 8, p. 4356, 2003.

[64] G. Stimpson, Introduction to Airborne Radar, 2014.

[65] A. S. D. Degiron, "Numerical Simulations of Long Range Plasmas," *Optics Express,* vol. 14, no. 4, p. 1611, 2006.

[66] S. Gunapala, Levine, R. BF, H. D and M. Panish, "InGaAs/InP Long Wavelength Quantum Well Infrared Photodetector," *Applied Physics Letters,* vol. 58, no. 18, p. 2024, 1991.

[67] K. J. M. F. D. W. A. S. J. J. R. Choi, "Electromagnetic Modeling of Quantum Well Infrared Photodetectors," *IEEE Journal of Quantum Electronics,* vol. 48, no. 3, p. 384, 2012.

[68] J. Hu, "A Substrate-Blind Platform for Photonic Integration," *SPIE Newsroom,* 2014.

[69] L. Li, S. Qiao, Y. Zou, S. Danto, K. Richardson, J. D. Musgraves, N. Lu and J. Hu, "Integrated Flexible Chalcogenide Glass Photonic Devices," *Nature Photonics,* vol. 8, p. 643, 2014.

[70] W. B. A. M. H. Wu, "Plasmonic Enhanced Quantum Well Infrared photodetector With HIgh Detectivity," *Applied Physics Letters,* vol. 96, p. 161107, 2010.